# MULTIELECTRON PROCESSES IN ION-ATOM COLLISIONS

**MIKHAIL ZAMKOV**

A DOCTOR'S DISSERTATION

DEPARTMENT OF PHYSICS

KANSAS STATE UNIVERSITY

MANHATTAN

2003

Approved by:

Prof. P.Richard

# Contents

**1 Introduction** **1**

**2 Zero-degree Auger Projectile Spectroscopy** **12**

2.1 Introduction . . . . . 12

2.2 Kinematic Effects . . . . . 16

2.2.1 Projectile–to–Laboratory Frame Transformation . . . . . 17

2.2.2 Kinematic Line Broadening . . . . . 28

2.3 Impulse Approximation . . . . . 34

2.3.1 Rutherford Scattering Model . . . . . 36

2.3.2 Elastic Electron Scattering Model . . . . . 37

2.4 Conclusions . . . . . 39

**3 Experimental Arrangement** **43**

3.1 Experimental Setup . . . . . 43

3.2 Vacuum . . . . . 50

3.3 The Spectrograph . . . . . 53

3.4 The Position Sensitive Detector . . . . . 56

3.5 Electronics and Data Acquisition System . . . . . 58

3.6 Dead Time . . . . . 63

**4 Metastable Fraction Determination: Theoretical Description** **67**

4.1 Background and Motivation . . . . . 67

4.2 Experimental Technique for the Determination of the Metastable Fraction in He-like Ions . . . . . 69

4.3 Proposed Model for the Calculation of the Metastable Fraction . . . 77

**5 Metastable Fraction Determination: Experimental Results 85**

5.1 Metastable Fraction in $B^{3+}$ Beams Produced in Foil and $N_2$ Gas Targets 85

5.2 Metastable Fraction in Fast He-like F, O, N Beams . . . . . 90

5.3 Metastable Fraction in $C^{4+}$ Beams: Influence of K-vacancy Sharing . 96

5.4 Model Calculations for the Fraction of Metastable Ions . . . . . 96

5.5 Foil Thickness Considerations . . . . . 99

**6 Experimental Study of the Triply Excited $B^{2+}$ ($2s2p^2\,{}^2D$) Resonance 102**

6.1 Background and Motivation . . . . . 102

6.2 Experimental Details . . . . . 103

6.3 Results: Absolute Cross Sections and Decay Rates for the $B^{2+}$ ($2s2p^2\,{}^2D$) Resonance . . . . . 107

6.4 Concluding Remarks . . . . . 112

**7 Triple Electron Capture in Fast Ion–Atom Collisions 114**

7.1 Introduction . . . . . 114

7.2 Experimental Procedure . . . . . 118

7.3 The Independent Particle Model . . . . . 121

7.4 Results and Discussion . . . . . 127

7.5 Conclusions . . . . . 134

**8 Experimental Observation and Theoretical Calculations of Triply Excited $2s2p^2\ {}^2S^e$, ${}^{24}P^e$, ${}^2D^e$, and $2p^3\ {}^2P^o$, ${}^2D^o$ States of Fluorine 136**

8.1 Background and Motivation . . . . . 136

8.2 Experiment . . . . . 139

8.3 Hyperspherical Close Coupling Calculations . . . . . 149

8.4 Results and Discussion . . . . . 152

8.5 Conclusions . . . . . 156

**9 Conclusions 157**

# List of Figures


1 Zero-degree spectrum obtained by the KSU tandem spectrometer. . . 15

2 Velocity addition diagram. . . . . 16

3 Two auto-ionizing states with energies 60 MeV and 100 MeV, respectively. . . . . 20

4 The stretching effect. . . . . 24

5 Stretching (compressing) $\Delta\epsilon/\Delta\epsilon'$ between two Auger lines. . . . . 25

6 Angular compression of electrons emitted from fast projectiles. . . . . 26

7 Geometrical interpretation of the broadening effect. . . . . 29

8 Broadening coefficients $\Delta B_\theta^{(1)}/\epsilon$ and $\Delta B^{(2)}/\epsilon$ as a function of the laboratory angle $\theta$. . . . . 32

9 Calculated IA–Rutherford BEe DDCSs. . . . . 38

10 Compton profiles for $H_2$, He and Li. . . . . 39

11 Top view of the J. R. Macdonald Laboratory. . . . . 45

12 The zero-degree experimental setup. . . . . 48

13 Chamber pressure as a function of the gas-cell pressure. . . . . 52

14 The hemispherical paracentric spectrograph for ZAPS. . . . . 54

15 The 4-element electrostatic focusing and decelerating lens. . . . . 55

16 Chevron arrangement microchannel plates. . . . . 57

17 The Electronics Diagram. . . . . 60

18 XSYS Data Acquisition System output. . . . . 61

19 Formation mechanisms of the doubly excited states of Li-like ions resulting from collisions of metastable He-like ($1s^2\,{}^1S, 1s2s\,{}^3S$) beams with gas targets. . . . . 71

20 Two possible formation mechanisms of metastable $1s2s\,{}^3S$ state from the ground state of Li-like ions. . . . . 79

21 The comparison of predicted and observed ratios of the metastable fraction produced in $N_2$ gas to the metastable fraction produced in a foil. . . . . 82

22 Production of metastable He-like ions in a foil from the incident Li-like beam. . . . . 84

23 Zero degree Auger spectra measured for $B^{3+} + H_2$ collisions at the projectile energies of 5.1 and 7.1MeV. . . . . 87

24 The metastable fraction F $=B^{3+}(1s2s\,{}^3S)/B^{3+}(1s^2\,{}^1S, 1s2s\,{}^3S)$ versus the stripping energy. . . . . 89

25 Zero-degree Auger spectra measured for 25.3 MeV $F^{7+}$ on $H_2$ collisions. 92

26 Zero degree Auger spectra measured for 24.6 MeV $O^{6+}$ on $H_2$ collisions. 93

27 The metastable fraction F in He-like B, C, N, O, F beams versus the projectile velocity in units of projectile K-shell electron velocity. . . . 95

28 Techniques for measurement of charge state fractions $N_1, N_2, N_1', N_2'$ . 98

29 The metastable fraction F in 13.27 MeV $C^{4+}$ beams as a function of foil thickness. . . . . 101

30 The formation and decay diagram of the triply excited resonance $2s2p^2\,{}^2D$ . . . . . 106

31 Zero degree Auger projectile electron measurements of the triply excited resonance $2s2p^2\,{}^2D$ in $B^{3+}$ beams . . . . . 108

32 Measurements of single differential cross sections for the $1s2s\,{}^3S$ to $2s2p^2\,{}^2D$ excitation followed by Auger decay to the $1s2s\,{}^3S$ state as a function of the projectile energy. . . . . 110

33 Target pressure dependence for the KLL Auger electron emission in 13 MeV $C^{6+} + Ar$ collisions. The solid line represents the linear fit to the experimental data. . . . . 120

34 13 MeV $C^{6+} + Ar$ Auger electron spectra measured with low and high vacuum pressure in the area between the analyzing magnet and the gas cell. Solid circles represent experimental data taken with a vacuum pressure of $1 \times 10^{-4}$ Torr, and open circles represent experimental data taken with a vacuum pressure of $1 \times 10^{-6}$ Torr. . . . . 123

35 The energy level diagram for the $C^{6+}$ + Ar collision system. K and L shell binding energies of $C^{5+}$ match the L shell binding energy of Ar, which maximizes the electron transfer probability. . . . . 126

36 Absolute Auger electron DDCS spectra for the collision system of 13 MeV $C^{6+}$ + Ar . . . . . 129

37 Absolute SDCS measurements of triple electron capture to the $C^{3+}$ KLL states. . . . . 132

38 Possible Auger relaxation pathways from the triply excited states of Li-like fluorine into the continua of $F^{7+}$ ions. . . . . 138

39 Visualization of the electron transfer probability. . . . . 142

40 Present experimental measurements of Auger decay channels from the triply excited states of Li-like fluorine into the continua of $F^{7+}$ ions. . . . . 143

41 Present experimental measurements of Auger decay channels from the triply excited states formed in collisions of $F^{9+}$ ions on Kr. . . . 146

42 Present experimental measurements of Auger decay channels from the KLM and quadruply excited states formed in collisions of $F^{9+}$ ions on Kr. . . . . 147

43 Adiabatic hyperspherical potential curves for $^2P^o$ states of $F^{6+}$. . . . 151

# List of Tables


1 Doubling, shifting, stretching and enhancing frame transformation kinematic effects for $\theta = 0°$ detection. . . . . 42

2 Basic geometrical parameters of the ZAPS setup. . . . . 66

3 Auger yields for the decay from the 1s2s2p $^4P$ state. . . . . 74

4 Lifetimes and fractions of $1s2s\,^1S$ and $1s2s\,^3S$ ion beams that reach the target area at $v_p/v_k$ =1. . . . . 76

5 Comparison of the calculated and measured metastable fractions for $B^{3+}$ beams. . . . . 99

6 Measured and calculated autoionization rates, branching ratios and widths for the triply excited $2s2p^2\,^2D$ state of $B^{2+}$. . . . . 112

7 Correction factors for the extraction of the experimental SDCS for the triple electron capture to the $C^{3+}$ KLL states, from the corresponding DDCS spectra. . . . . 135

8 Summary of present experimental results and theoretical calculations for the observed triply excited states of $F^{6+}$. Single differential cross sections (SDCS) are given in units of $10^{-21} cm^2/sr$. Auger energies are calculated relative to the ground state of Li-like fluorine (E = 2242.2 eV [**?**]). . . . . 154

9 Summary of experimental and theoretical branching ratios for main Auger decay channels from triply excited states of $F^{6+}$. . . . . 155

# Acknowledgments

It is a great pleasure to express my sincere gratitude to the people who supported and inspired me throughout this period of my life. First of all I would like to thank my supervisor, the director of the J. R. Macdonald laboratory, Prof. Patrick Richard for guiding me through the numerous experimental details and always being the first to stand by my initiatives. It was his ideas and remarks whether on the interpretation of the experimental data or the understanding of physical phenomena that very often promoted a guiding path for further investigations. I also express my gratefulness to him for giving me the chance to participate in many conferences, where I had a privilege to meet with leading scientists. At this point, I would like to acknowledge the financial support of the Chemical Sciences, Geosciences and Biosciences Division, Office of Basic Energy Sciences, Office of Science and the U. S. Department of Energy.

I am greatly indebted to my colleagues from the University of Crete E. Benis and T.J.M. Zouros for mentoring my transition into Auger electron spectroscopy. My special thanks are extended to Manolis Benis, a true friend and co–worker, for sharing his experience in many aspects of research and beyond, very often, at the expense of his own time. His invaluable contribution to the description of zero–degree Auger electron spectrometer utilizing a hemispherical analyzer in this work is greatly appreciated.

I also would like to express my thanks to the personnel of JRML and the Machine Shop for their support and willingness to help, which provided a very friendly and at the same time productive work environment. I especially acknowledge Prof. Kevin Carnes and Vince Needham for their help with the computers, Bob Krause for providing the ion beams, Hiro Tawara, Bob Geering, Mike Wells and Al Rankin for their help on various daily problems.

My gratefulness along with my admiration are extended to my professors in the Department of Physics at Kansas State University, for their high quality lectures during my graduate studies. I am greatly indebted to Prof. C.D. Lin for providing me with a strong theoretical support and fruitful discussions on the physics of multi–excited states of ions.

I also express my gratefulness to Dea Richard for being very helpful in countless everyday issues and for reading and commenting on my manuscripts, abstracts and the present thesis.

Finally, I would like to express my deep and most sincere thanks along with my true love to my son who has been an inspiration to my work for all these years. This work is dedicated to him.

# ABSTRACT

Multielectron interactions in fast ion–atom collisions were investigated using high–resolution projectile Auger electron spectroscopy. Experimental studies were performed by measuring state-resolved projectile Auger cross sections utilizing a novel high–efficiency hemispherical detector–analyzer. Experimental data were used both to test the predictions of recent theoretical calculations and to provide a basis for the development of new atomic models.

A novel experimental technique for the determination of the metastable $1s2s\,^3S$ ion fraction has been developed and subsequently used to measure the metastable fraction in fast He-like beams. The dominant contribution to the formation of the metastable $1s2s\,^3S$ state in collisions of He-like ions with atomic targets was identified. A model for the calculation of the metastable ion fraction has been developed and successfully applied for predictions of absolute values and energy dependence of the metastable content. Having the accurate knowledge of the metastable $1s2s\,^3S$ state fraction enabled a novel approach for the investigation of the triply excited $2s2p^2\,^2D$ resonance produced in collisions of metastable $B^{3+}$ ions with $H_2$ targets by resonant transfer excitation. The results were compared to existing theoretical calculations within the $1/Z$ expansion method.

A new experimental technique for studying multielectron capture in ion–atom collisions has been introduced by measuring state–selective differential cross sections of intermediate multiexcited states. Measurements of the Auger electron emission in

the direction of the ion beam were used to determine the absolute single differential cross sections for the triple electron capture to all autoionizing KLL states. The results were compared to cross sections calculated within the independent particle model.

The study of triple electron capture stimulated a new experimental technique that relies on a strong projectile-Coulomb interaction to populate triply excited states in Li-like ions. The production of these states is realized in energetic ion-atom collisions by triple electron capture. The method is demonstrated by studying triply excited $2s2p^2\ {}^2S^e$, ${}^{2,4}P^e$, ${}^2D^e$, and $2p^3\ {}^2P^o$, ${}^2D^o$ states of fluorine formed in fast collisions of bare $F^{9+}$ ions with Ar and Kr targets; both experimentally, using zero-degree Auger projectile electron spectroscopy and theoretically, using the hyperspherical close coupling method.

# 1 Introduction

### Dissertation Goals

The study of electron interactions with highly charged ions plays an essential role in developing models and providing important cross section data to other scientific branches of physics, such as plasma physics, astrophysics, nuclear physics and solid state physics, as well as in other sciences such as chemistry, biophysics and medicine. Electron-ion resonances can substantially alter the charge and energy distributions in high temperature ion-electron environments that include plasma from fusion, discharges, and ion sources. Measured and calculated differential electron scattering cross sections are important for the testing of models of inelastic energy loss processes, which lead to x-ray emission and charge transfer. Accurate knowledge of the cross sections of such processes is of vital importance for understanding controlled nuclear fusion and the modelling of astrophysical plasma. Furthermore, interest in electron emission cross sections is especially widespread in applied particle physics such as radiobiology since about 2/3 of the energy loss of the ion is transferred into the kinetic energy of $\delta$ electrons.

Due to a number of experimental difficulties associated with the merged-beams

technique, earlier electron–ion experiments were generally limited to collision systems with relatively large cross sections using low-charge-state beams. With the advent of the electron scattering model (ESM) that related basic electron–ion interactions to those in ion–atom collision systems, a spectacular opportunity has emerged to study many fundamental processes at a new level. More specifically, in the ESM the dynamic electron-electron interactions are treated within a semi–classical approach called the Impulse Approximation (IA). Its main idea rests on the fact that in the reference frame of the fast moving projectile ion, the loosely–bound target electron, often referred to as a quasi–free electron, can be treated as an incoming free particle. The validity of this approximation for fast moving projectile ions and the availability of thick, quasi–free electron targets, have allowed for intense, well-characterized collisions for studying low cross section processes.

In this work, the interest is focused on the projectile Auger electrons, emitted in energetic collisions between highly charged ions and atoms. Energies of these Auger electrons carry the signature of the processes that occurred during the collision time, providing invaluable information about the structure of the charged particles and the collision mechanisms.

The technique of detecting Auger electrons emitted from projectiles at 0° with respect to the beam direction, is known as Zero-degree Auger Projectile Spectroscopy (ZAPS) and has received considerable attention in the past two decades [**?**, **?**]. The potential advantage of the technique is that it is the *only* efficient method that

provides *state-selective* double differential cross section information about collision mechanisms. X-ray crystal spectrometry, while having similar resolutions, suffers from very low efficiency, COLTRIMS benefits from similar resolutions accompanied by the superior detection efficiency, however, works only for relatively low energy electrons (<300eV) [**?**]. Consequently, the use of ZAPS to investigate Auger electrons arising from energetic ion–atom collisions in the present work is well justified. The advantages of this technique, as also the limitations, are examined in the first two chapters.

In brief, the primary purpose of this work is to address the dynamic electron–electron interactions in ion–atom collisions by applying zero–degree Auger projectile spectroscopy and to provide new measurements utilizing weak intensity beams and/or low cross section processes using a novel high-efficiency hemispherical detector–analyzer.

**Zero-degree Auger Projectile electron Spectroscopy**

The Zero-degree Auger Projectile electron Spectroscopy is discussed in chapter 2. Theoretical aspects of the kinematics frame transformation effects, such as peak doubling, energy shifting, line stretching, angular compression and peak height enhancement, in addition to line broadening effects are investigated and upon which are further commented. New prospects of this method arising from the high elec-

tron detection efficiency of the novel hemispherical detector analyser [**?**], are explicitly pointed out. In chapter 3, the ZAPS experimental station setup at the J. R. Macdonald (JRM) laboratory at Kansas State University is described. A detailed characterization of its features, including hardware components, the spectrograph consisting of the hemispherical detector analyser (HDA), the focusing/decelerating lens and the two-dimensional position sensitive detector (2D-PSD), the vacuum conditions, the electronics and the data acquisition system is given. In addition, the key geometrical parameters of the spectrograph in relation to the experimental setup also are provided.

**The fraction of metastable $1s2s\,^3S$ ions in He-like beams: experimental determination and study of the production mechanism.**

Experimental measurements of various collision cross sections for fast He-like ions require quantitative information on the fraction of ions in a long-lived $1s2s\,^3S$ metastable state present in two-electron ion beams. The knowledge of this fraction is necessary for the absolute cross section measurements of numerous processes in ion–atom and electron–ion collisions including dielectronic recombination, transfer excitation, capture of the target electron, inelastic scattering or recently discovered superelastic scattering of target electrons from highly charged metastable ions [**?**].

A number of experimental techniques have been developed for the determina-

tion of the metastable fractions over the years, and several measurements of the metastable fraction have been reported in literature for various He-like ions. Until now, however, the unified treatment that accounts for a wide range of beam energies and target densities, which dramatically affect the metastable population in two-electron ions, has not yet come forth. That creates a major problem in determining absolute cross sections for collisions with He-like ions, since theoretical calculations are very often unable to predict the correct fractions. Therefore, the goal of the present investigation was to measure the metastable fraction for the He-like isoelectronic sequence to establish a benchmark for various absolute measurements in metastable ion-atom collisions.

In this work, a universal technique for the determination of the metastable $1s2s\,^3S$ ion fraction has been developed. The method is based on measurements of the Auger electron emission from doubly excited states of Li-like ions formed in collisions of several different beams with light targets. The unique signature of these double excited KLL states allows one to determine the fraction of the incoming ions in the beam that were initially in the metastable $1s2s\,^3S$ state. The developed technique was used to measure the fraction of metastable $1s2s\,^3S$ ions in fast He-like B, C, N, O, and F beams produced in collisions with thin carbon foils as a function of both the incident energy in the range of 0.5 to 2 MeV/u and the foil thickness in the range of $1 - 5\mu g/cm^2$.

In the last stage of this work, a considerable effort was directed toward the

qualitative and quantitative description of the production mechanisms involved in the formation of the metastable $1s2s\,^3S$ ions in foils, justified by the keen need for numerical predictions of metastable fractions for systems that were not studied experimentally. It was demonstrated that the dominant production mechanism of the metastable $1s2s\,^3S$ ions in both foil and gas targets is the K-shell vacancy production in incoming beams, that leaves ions in the H-like charge state, followed by subsequent electron capture. The proposed mechanism has been verified experimentally and used to derive a numerical model for the calculation of the metastable fraction for He-like beams. In chapter 4, the energy dependent metastable fraction in He-like beams (Z=5-9) determined both from the experimental measurements and from the model calculations is presented.

**Study of the triply excited $B^{2+}(2s2p^2\,^2D)$ resonance in metastable ion–atom collisions.**

The knowledge of the metastable fraction in He-like beams enabled a novel approach to the production of $2s2p^2\,^2D$ hollow states in Li-like ions. Simultaneous excitation of all three electrons from the ground state of ions directly into a hollow state presents some experimental difficulties associated with small cross sections for the process. Alternatively, the excitation can be divided into two steps. First, one K–shell vacancy is produced in the primary Li-like beam by passing it through a thin

foil, which leaves some ions in the metastable $1s2s\,^3S$ state. Then, the transition to the triply excited $2s2p^2\,^2D$ state is induced in collisions of the metastable ions with target gas by resonant transfer excitation (RTE).

In the present work, the $B^{3+}(1s2s\,^3S)$ metastable beam has been used to populate the triply excited $2s2p^2\,^2D$ state in collisions with molecular hydrogen targets. The resonance was observed to decay back to the $B^{3+}(1s2s\,^3S)$, the electron elastic scattering channel and to the $B^{3+}(1s2s\,^1S)$ and $B^{3+}(1s2p\,^3P)$, the two electron inelastic scattering channels. Measurements of the Auger electron emission in the direction of the ion beam were used to determine the absolute cross sections for the formation of the $2s2p^2\,^2D$ state and the branching ratios of the corresponding electron scattering channels. The results have been compared to the recent theoretical prediction of the 1/Z expansion method [?].

**Triple electron capture.**

Multiple electron capture in collisions of highly charged ions with multielectron atoms or molecules has become a very active area of atomic physics research in the last decade. Transfer processes with more than two active electrons represent a fundamental problem of a many-body dynamic system, thus providing tests for most contemporary atomic models. The present understanding of multiple electron transfer has come from numerous experimental and theoretical studies primarily in

terms of the classical quasimolecular description of the process. To date, however, a general approach, suitable for a wide range of impact velocities, has not yet been presented. In particular, the role of electron-electron correlation effects in multi-electron capture still remains unclear, raising the demand for a more comprehensive model.

Experimental investigation of multiple electron transfer resulting from fast, highly charged ion-atom collisions is hampered by the rapid fall off of capture probabilities with increasing velocity of the ion. To the best of our knowledge, the study of true triple electron capture in fast (v $>$ 1 a.u.) collisions has not been attempted experimentally. Meanwhile, the case of multiple electron transfer at high impact velocities becomes more appealing, due to the dominant role of the process in populating lower-lying multiexcited states, recently a very dynamic area of atomic research. Additional incentives to investigate multielectron processes in fast collisions are provided by their importance in such diverse areas as high temperature plasma studies, astrophysics, and laser technology.

Theoretically, the extended classical overbarrier model (ECB), moderately successful in describing multielectron capture at small impact velocities [**?**, **?**], cannot be utilized for predictions in fast ion-atom collisions, due to the fact that the interaction time at higher projectile velocities is not sufficient for target electrons to be molecularized. However, since in fast ion-atom collisions projectile core states do not fully readjust due to the small interaction time, and thus, are only partly

screened by target electrons during the collision, greater confidence is given to the independent particle model.

In the present work, high resolution zero-degree Auger electron projectile spectroscopy is used to study true triple electron capture to doubly excited KLL states of carbon. The states are produced in fast collisions (v = 4.5-6.6 a.u.) of bare $C^{6+}$ projectiles with Ar gas targets. By using the Auger electron spectroscopy in it was possible to account for the projectile charge change caused by the Auger decay following the collision. High resolution measurements of differential cross sections for individual KLL states provided a unique tool for testing the predictions of the independent particle model for the triple electron capture. In chapter 6, the influence of the present study on our understanding of projectile screening and electron-electron correlation effects in multiple electron capture is discussed.

**Study of triply excited states in Li-like ions.**

The study of triply excited states of atoms and ions presents new opportunities to probe multi-particle excitations of a quantum system. For these states, interelectronic correlation plays a crucial role in determining their properties. As a result, theoretical descriptions based on the conventional independent particle model fail completely. Thus, the description of the atomic structure as well as excitation and decay dynamics for triply excited states provides unique challenges to theory. In the

last decade, advances in synchrotron radiation technology have stimulated a considerable experimental and theoretical interest to the subject. In particular, the recent investigations using high–resolution photoelectron spectroscopy have provided some of the most detailed information on the partial photoionization cross sections for a number of triply excited states [?, ?, ?, ?, ?, ?].

Until now, the study of Li-like triply excited states have focused almost exclusively on neutral lithium. This is primarily due to the insufficient densities of ionic targets, which rules out the possibility to investigate triply excited resonances in Li-like ions using synchrotron radiation. Furthermore, the limited nature of the photoexcitation technique prohibited the population of quartet states, recently an ideal probe for photodetachment studies. The absence of available experimental data for three electron ions has prevented theorists from pursuing a global understanding of triply excited states, such as new classification schemes, approximate quantum numbers, and possible approximate selection rules for the formation and the decay of these states.

In this work a new experimental method, relying on strong electron-projectile Coulomb interaction, has been developed to efficiently form triply excited states of ions and atoms. The states are produced via triple electron capture in energetic ion-atom collisions. This technique benefits from the fact that by the proper selection of collision partners, any triply excited state of any ion can, in principle, be populated. In chapter 7, the method is demonstrated by studying the $2l2l'2l''$ intrashell states

of fluorine. In particular, all $2s2p^2$ and $2p^3$ triply excited states of $F^{6+}$ ions are produced in collisions of bare 16 MeV $F^{9+}$ ions on Ar. Multiple transitions from these states into the continua of $F^{7+}$ are identified from the ejected electron spectra in the direction of the ion beam and used to determine transition energies, branching ratios and absolute differential cross sections for the observed states. Experimental measurements are compared to new calculations based on the hyperspherical close coupling method (HSCC), courtesy of our collaborators T. Morishita and C. D. Lin. The experimental branching ratios were also compared to other available theoretical calculations.

# 2 Zero-degree Auger Projectile Spectroscopy

## 2.1 Introduction

Projectile electron spectroscopy of highly–charged ions in collisions with simple targets, such as $H_2$ and He, provided unique experimental conditions for studying basic electron–ion interaction mechanisms, such as excitation, ionization and capture. The large variety of highly charged ions available at a wide range of energies and charge states, is the main advantage of the method. A weak point is kinematic line broadening, which limits the Auger electron spectra resolution and therefore its applicability. The minimization of this problem originates from the fact that line broadening strongly depends on the detection angle. As will become clear in this chapter, electron detection at 0° or 180° with respect to the beam direction, substantially reduces line broadening. The first measurements at these favorable angles were reported at 180° for low keV/u collisions [**?**, **?**, **?**], at 0° for high (1-5MeV/u) [**?**, **?**] and intermediate (15-150keV/u) [**?**] collision energies. Ever since, only zero-degree measurements have been reported, mainly due to the fact that, for high energy collisions, electron detection at 180° is not possible. The method of projectile Auger electron detection at zero-degrees is known as Zero-degree Auger

electron Projectile Spectroscopy (ZAPS).

Auger electron Projectile Spectroscopy also can deliver elaborate information on electron–electron interactions through measurements of state-selective differential cross sections in a number of basic collision mechanisms, such as transfer and excitation [?, **?**], resonance transfer and excitation [**?**, **?**, **?**, **?**, **?**, **?**, **?**], electron-electron excitation [**?**, **?**], electron-electron ionization [**?**, **?**, **?**], and double electron capture [**?**, **?**, **?**, **?**, **?**]. The technique offers an exclusive study of electron production mechanisms such as cusp electrons [**?**, **?**] and binary encounter electrons ( [**?**] and references therein). The results obtained with ZAPS measurements are used in diverse practical applications such as in plasma physics, fusion research, astrophysics and biophysics. On the other hand, theoretical ion-atom collision models, largely successful up to now in total and single differential cross-section predictions, are more accurately tested using state-selective double differential cross section measurements. Furthermore, few electron collision systems, mostly utilized with ZAPS, provide a simple ground for studying the many-body problem, with emphasis on electron-electron interactions [**?**].

Typical zero-degree low resolution spectra of 1.5 MeV $H^+$ + He are shown in Fig. **??**. The intense sharp peak at the left part of the spectrum, centered at energy t=750eV, is known as the *cusp* peak. The processes involved with the cusp peak are the electron capture to the continuum (ECC) and the electron loss to the continuum (ELC) [?]. During the ECC process, electrons from the target are

captured to the continuum of the projectile, while during the ELC process, electrons from the projectile are excited to the continuum of the projectile.

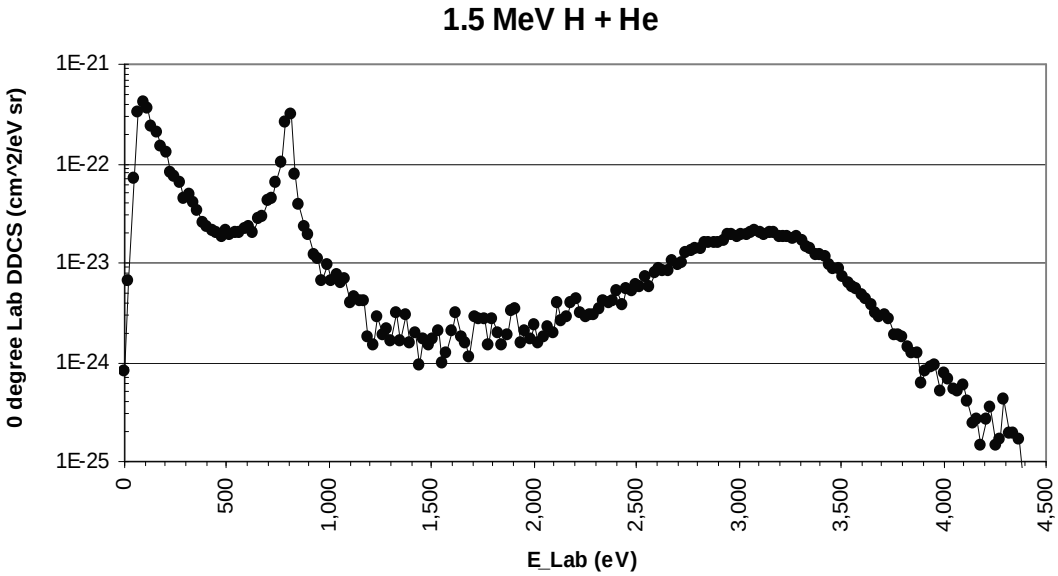


Figure 1: A typical Zero-degree spectrum obtained with the KSU tandem spectrometer.

The cusp peak, present only at zero-degree measurements, plays an important role in the determination of the beam kinetic energy, since cusp electrons are moving at the same velocity as the projectiles [?, **?**, ?].

The broad peak at the right part of the spectrum, centered at energy $\simeq$ 4t, is known as the Binary Encounter electron (BEe) peak [?]. Binary-encounter electrons are target electrons ionized through direct, hard collisions with energetic projectile ions. BEe double differential cross sections (DDCS) of bare ions colliding with $H_2$ or He targets, were used in the past for determining the electron detection efficiency, thus obtaining absolute DDCSs in electron spectra [**?**].

## 2.2 Kinematic Effects

Auger electrons emitted from projectile ions imprint projectile's momentum in their trajectories. A detailed analysis of the general electron kinematic effects can be quite complicated [**?**]. However, for the case of energetic collisions of a few MeV/amu, studied in this dissertation, projectile ions are scattered through very small angles ($\sim$ mrads), resulting in negligible effects both on the energy loss and on the projectile electron trajectories.

Thus, for simplicity, the projectile ion scattering angle in swift collisions can be safely assumed to be zero. With this consideration, a simple velocity vector addition model is sufficient for determining the projectile-to-laboratory frame transformation and related kinematic effects, as the ion-recoil effects can be overlooked.

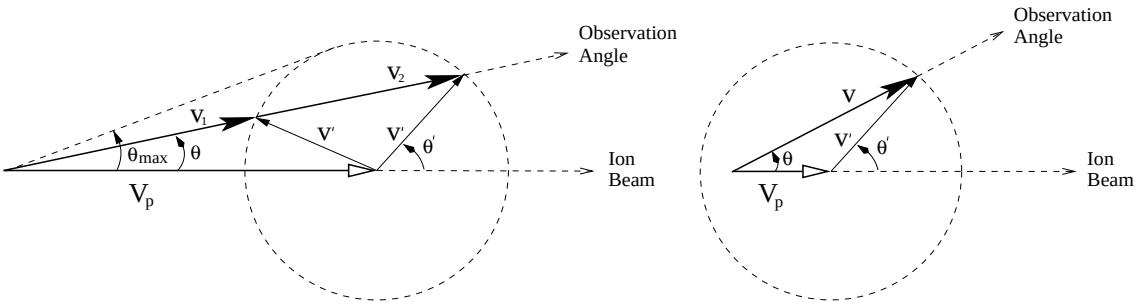


Figure 2: Velocity addition diagram [?]. The electron velocity $\mathbf{v}'$ in the projectile rest frame is transformed in the laboratory frame according to the vector addition rule as $\mathbf{v} = \mathbf{V_p} + \mathbf{v}'$ [*Left*] Projectile ion velocity is larger than the Auger electron velocity $V_p > v'$. [*Right*] Projectile ion velocity is smaller than the Auger electron velocity $V_p < v'$

The velocity $\mathbf{v}$ of the Auger electron in the laboratory frame is obtained by adding the projectile velocity $\mathbf{V}_p$ to the velocity $\mathbf{v}'$ of the electron in the projectile rest frame as shown in Fig. **??**. Denoting by primed symbols the quantities in the projectile rest frame, the electron kinetic energy $\epsilon = \frac{1}{2}mv^2$ in the laboratory frame can be related to the corresponding rest frame electron kinetic energy $\epsilon' = \frac{1}{2}mv'^2$ as:

$$\epsilon = \epsilon' + t + 2\sqrt{\epsilon' t}\ cos\theta' \tag{1}$$

or equivalently

$$\epsilon' = \epsilon + t - 2\sqrt{\epsilon t}\ cos\theta \tag{2}$$

where

$$t = \frac{1}{2}mV_p^2 = \frac{m}{M}\ E_p\ =\ 548.58\ \frac{E_p(MeV)}{M(amu)}\ (eV) \tag{3}$$

is the reduced projectile energy known also as the *cusp* energy. $E_p$ and M are the kinetic energy and mass of the projectile respectively, while $m$ is the electron mass.

### 2.2.1 Projectile–to–Laboratory Frame Transformation

In order to systematically study the kinematic transformation properties of the experimentally measurable physical quantities, it is convenient to adopt the universal dimensionless parameter $\zeta$ [?]

$$\zeta \equiv \sqrt{\frac{t}{\epsilon'}} = \frac{V_p}{v'} \tag{4}$$

From the experimental point of view, it is advantageous to express the relation between the energies in the rest and laboratory frame as a function of the *laboratory* observation angle $\theta$. Using simple trigonometric rules in Fig. **??**, geometry, and the introduced parameter $\zeta$, the energy in the laboratory frame can be written as

$$\epsilon_{\pm}(\theta) = \epsilon'(\zeta\cos\theta \pm \sqrt{1-\zeta^2\sin^2\theta}\ )^2 \qquad (\zeta > 1,\quad 0 < \theta < \arcsin\frac{1}{\zeta}) \tag{5}$$

$$\epsilon(\theta) = \epsilon'(\zeta\cos\theta + \sqrt{1-\zeta^2\sin^2\theta}\ )^2 \qquad (\zeta < 1,\quad 0 < \theta < 180^\circ) \tag{6}$$

As illustrated in Fig. **??**, for fast emitters ($V_p > v'$ or $\zeta > 1$ ) there can be two possible solutions for the laboratory electron energy $\epsilon$ as a function of the laboratory detection angle $\theta$, while for slow emitters ($V_p < v'$ or $\zeta < 1$) there is only one solution that represents Auger electrons scattered in the forward direction. For fast emitters ($\zeta > 1$) the constraint $\zeta^2 \sin\theta^2 \leq 1$ results in a restriction in the observation angle $\theta$ with a maximum value

$$\theta_{max} = \arcsin\frac{1}{\zeta} \tag{7}$$

This is a crucial limitation for non-zero degree Auger Projectile Spectroscopy since different electron energies correspond to different maximum detection angles, applying a lower limit on the electron energies accessible to the spectrometer. However, for $\theta = 0^\circ$ (i.e. ZAPS technique) the whole projectile electron energy range becomes accessible. This is one of the most important advantages for measuring electron

spectra at zero degrees. In the case of $\theta = 0°$, Eqs. **??**, **??** reduce to [1]

$$\epsilon_+ = (\sqrt{\epsilon'} + \sqrt{t}\ )^2 = \epsilon'(1+\zeta)^2 \qquad (\ All\ \ \zeta,\ \theta' = 0°,\ \theta = 0°\ ) \tag{8}$$

$$\epsilon_- = (\sqrt{\epsilon'} - \sqrt{t}\ )^2 = \epsilon'(1-\zeta)^2 \qquad (\ \zeta > 1,\ \theta' = 180°,\ \theta = 0°\ ) \tag{9}$$

Kinematic effects change the position, energy width and intensity of an Auger line and are referred to in the literature as *shifting, stretching* and *enhancing*, respectively. Also the possible occurrence of the same Auger line at two different electron energies in the spectrum is referred to as *doubling* [?]. In Table **??** the results of the kinematic transformation analysis are summarized for the case of zero degree laboratory detection angle. A detailed presentation of each case follows.

- Doubling of Auger lines

It already has been shown (see Fig. **??** and Eq. **??**), that there can be two possible solutions for the laboratory electron energy $\epsilon$, resulting in the observation of two peaks in the laboratory frame, which correspond to the same Auger transition energy. The phenomenon is known as *doubling* and an example of it is given in Fig. **??**. The two Auger peaks appear symmetrically around the cusp peak as predicted by Eqs. (**??**) and (**??**). In this way, forward-backward asymmetries of inelastically scattered quasi-free target electrons from ions were successfully studied [**?**]. Doubling serves a practical application in the accurate determination of the beam energy [?].

[1] For 180° observation Eqs. **??**, **??** result in $\epsilon = \epsilon'(1-\zeta)^2 \qquad (\zeta < 1,\ \theta' = 180°,\ \theta = 180°\ )$

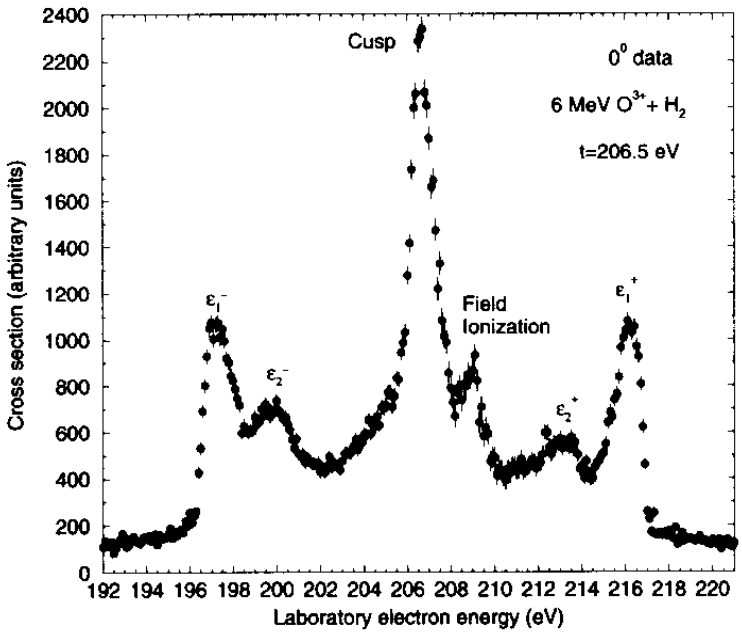


Figure 3: Example of detection of two auto-ionizing states with energies 60meV and 100meV, respectively, at laboratory energies around 200eV, in collisions of 6MeV $O^{3+}$ + $H_2$. Each peak appears symmetrically around the cusp peak due to the doubling effect. The small peak at the right shoulder of the cusp peak is due to the field ionization of projectile Rydberg states inside the analyser. From Ref. [?]

- Shifting of Auger energy in the laboratory frame

According to Eq. **??**, an electron emitted at energy $\epsilon'$ in the projectile rest frame will be detected in the laboratory frame at a different energy $\epsilon$. Forward electron emission in the projectile rest frame, ($\theta' = 0°$) yields a larger laboratory energy, while

backward electron emission ($\theta' = 180°$) yields larger or smaller laboratory energy values depending on the $\zeta$ value. It should be noted that detecting an Auger electron at an energy larger than its Auger transition value in ZAPS is very important, as it allows for the detection of very low energy electrons. For example, in the spectrum of Fig. **??**, the two auto-ionizing states shown have rest energies of 60 meV and 100 meV, respectively. They are detected though at laboratory energies around 200 eV. It should be emphasized at this point that detection of electrons with energies less than 10eV becomes an increasingly difficult task, since low energy electrons can be affected readily by very small stray magnetic and electric fields such as the earth's magnetic field or the contact potential fields developed at the interface between two different metal surfaces.

- Stretching

The energy width $\Delta\epsilon$ of an Auger line observed in the laboratory frame differs from the corresponding width $\Delta\epsilon'$ in the projectile rest frame. Differentiating Eq. **??** with respect to $\epsilon'$ results for zero-degree observation angle in:

$$\frac{\Delta\epsilon}{\Delta\epsilon'} \simeq \frac{d\epsilon}{d\epsilon'} = \sqrt{\frac{\epsilon}{\epsilon'}} = |1 \pm \zeta| \qquad (\theta = 0°) \tag{10}$$

It is clearly seen that for the case of a positive solution (forward electron emission in the projectile rest frame, i.e., $\theta' = 0$) line stretching is established, while for the case of (-) solution (backward electron emission in the projectile rest frame, i.e., $\theta' = \pi$)

a line stretching or compression is established depending on the $\zeta$ value (see Table **??**). It is very important to note that the energy stretching (or compressing) does not increase the overlap of two closely neighboring Auger lines. Therefore it does not wash out intrinsic structures in the spectrum. That is due to the stretching (compressing) of the mean values of the Auger lines by practically the same amount as their widths. An example of this stretching effect is given in Fig. **??**, where the Auger decaying states of $(1s2s2p)^2P_+$ and $(1s2p^2)^2D$ of $F^{6+}$ formed during collisions of 21.78MeV $F^{7+} + H_2$, are plotted in the laboratory (top) and projectile (bottom) rest frames, respectively. The ratios of the energy widths and energy difference of the two lines, measured in the laboratory and projectile frames, are identical: $\Delta\epsilon/\Delta\epsilon'$ $= \Delta\epsilon_{p-p}/\Delta\epsilon'_{p-p} = 2.08$. Although the line overlap is not affected by the stretching effect, the energy resolution $\Delta\epsilon/\epsilon$ *does* change. This easily can be derived from Eq. **??**:

$$\frac{\Delta\epsilon}{\epsilon} = \sqrt{\frac{\epsilon'}{\epsilon}}\,\frac{\Delta\epsilon'}{\epsilon'} \tag{11}$$

Eq. **??** is not valid for relatively large energy intervals. In order to calculate the correct formula in this case, two lines at energies $\epsilon'_1$ and $\epsilon'_2$ differing by the energy interval $\Delta\epsilon'$ are considered and subtracted mutually according to Eq. **??** yielding

$$\frac{\Delta\epsilon}{\Delta\epsilon'} = 1 \pm 2\,(\frac{t}{\epsilon'_1})\,(\frac{\epsilon'_1}{\Delta\epsilon'})(\sqrt{\frac{1+(\Delta\epsilon'/\epsilon'_1)}{t/\epsilon'_1}} - \sqrt{\frac{\epsilon'_1}{t}}\,) \qquad (\theta = 0^\circ) \tag{12}$$

For $\Delta\epsilon'/\epsilon'_1 << 1$, Eq.**??** is obtained. In Fig. **??** a plot of the quantity $\Delta\epsilon/\Delta\epsilon'$ as a function of the dimensionless variable $\Delta\epsilon'/\epsilon'_1$ is shown for different values of cusp

energies t according to Eq. **??**.

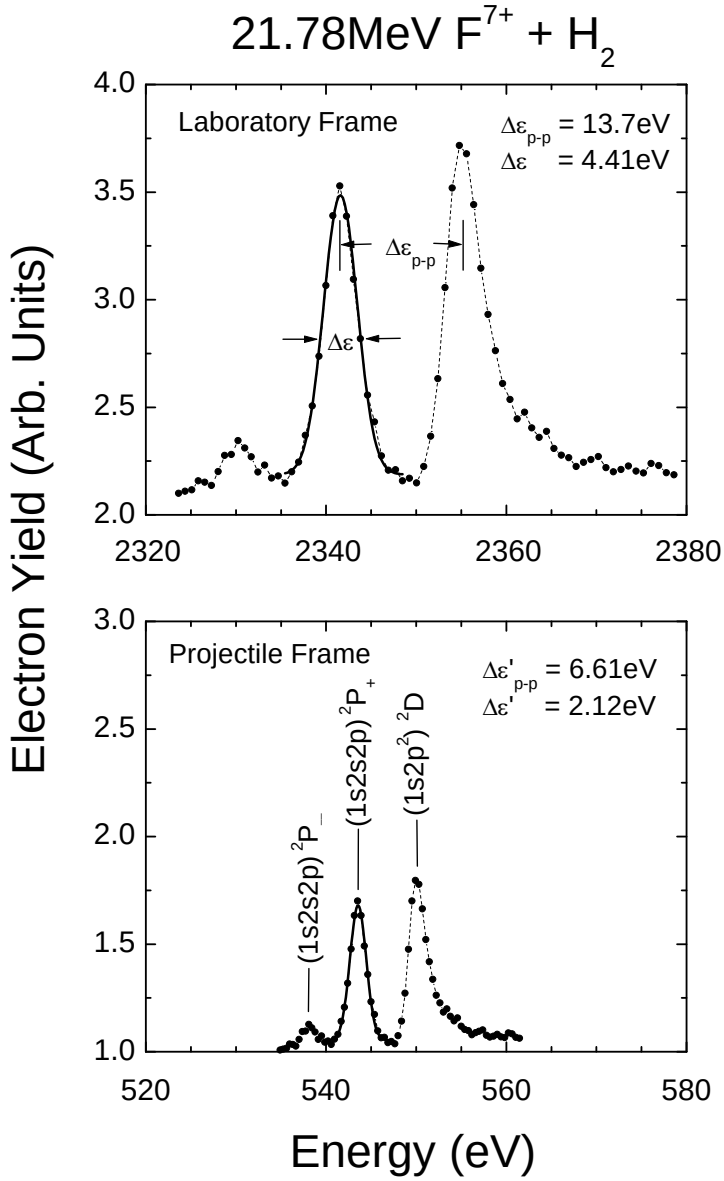


Figure 4: Example of the stretching effect. The Auger decaying states of $1s(2s2p\,^3P)^2P_-$, $1s(2s2p\,^1P)^2P_+$ and $1s2p^2\ ^2D$ of $F^{6+}$ formed during collisions of 21.78MeV $F^{7+} + H_2$, are detected in the laboratory [*top*], and then they are transformed to the projectile [*bottom*] rest frame, respectively. Note that $\Delta\epsilon/\Delta\epsilon' = \Delta\epsilon_{p-p}/\Delta\epsilon'_{p-p} = 2.08$.

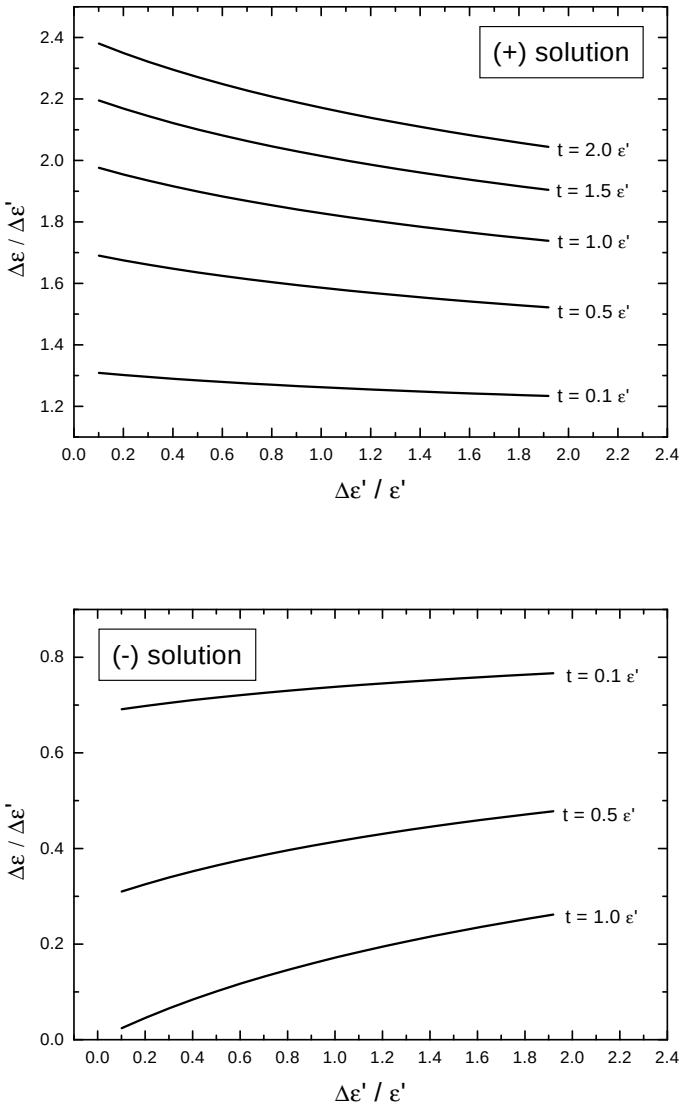


Figure 5: The amount of stretching (compressing) $\Delta\epsilon/\Delta\epsilon'$ between two Auger lines detected at the laboratory frame, is plotted as a function of their reduced rest frame energy interval $\Delta\epsilon'/\epsilon'_1$. Shown cases refer to different values of cusp energies t. [*Top*] (+) solution of Eq. **??** [*Bottom*] (-) solution of Eq. **??**. Analysis is made in ref. [?]

- Angular Compression

Electrons ejected from fast projectiles are influenced by the well known *beaming* effect observed in X-rays emitted from relativistic emitters. The phenomenon is dominant for forward emission in the projectile frame, while for backward emission it happens only for $\zeta > 2$. In Fig. **??** it is geometrically explained (in a two-dimensional projection) that for fast emitters the projectile frame solid angle $\Delta\Omega'$, denoted as $\Delta\Omega_-$ and $\Delta\Omega_+$, is always larger than the laboratory frame solid angle $\Delta\Omega$, defined by the distance between the source and the spectrometer opening.

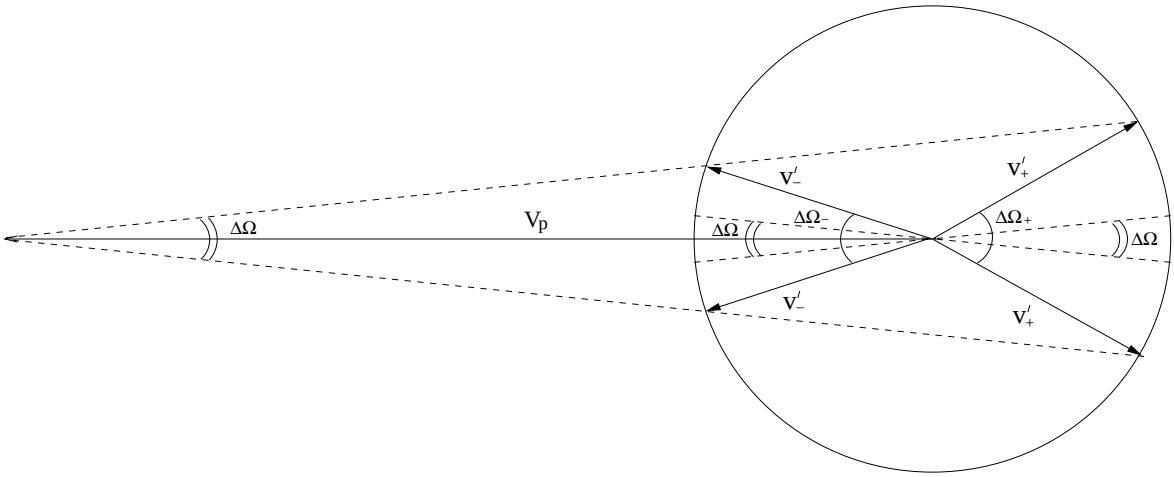


Figure 6: Angular compression of electrons emitted from fast projectiles.

For zero-degree laboratory observation angle ($\theta = 0°$), it is proved [?] that

$$\frac{\Delta\Omega}{\Delta\Omega'} \simeq \frac{d\Omega}{d\Omega'} = \frac{\epsilon'}{\epsilon} = \frac{1}{(1 \pm \zeta)^2} \qquad (\theta = 0,^\circ) \tag{13}$$

- Enhancement

The height of an Auger peak recorded at the laboratory frame differs from the hypothetical height recorded at the projectile rest frame. The situation is illustrated in Fig. **??**. The effect of the enhancement or diminishment of the Auger line intensity - mostly called *enhancement* - can be understood through the transformation of the double differential cross-section (DDCS) from projectile to laboratory frame at zero degrees. Combining Eqs. **??** - **??** results in:

$$\frac{d^2\sigma}{d\Omega d\epsilon} = \sqrt{\frac{\epsilon}{\epsilon'}}\,\frac{d^2\sigma}{d\Omega' d\epsilon'} = |1 \pm \zeta|\,\frac{d^2\sigma}{d\Omega' d\epsilon'} \qquad (\theta = 0^\circ) \tag{14}$$

In the cases of forward angles (+ solution, all $\zeta$) and backward angles (- solution and $\zeta > 2$) an enhancement of the laboratory peak heights is established, while in the case of backward angles ( - solution and $1 < \zeta < 2$) the situation is reversed.

Finally, the projectile-to-laboratory transformation for the single differential cross-section (SDCS) results in:

$$\frac{d\sigma}{d\Omega} = \frac{\epsilon}{\epsilon'}\,\frac{d\sigma}{d\Omega'} = (1 \pm \zeta)^2\,\frac{d\sigma}{d\Omega'} \qquad (\theta = 0^\circ) \tag{15}$$

### 2.2.2 Kinematic Line Broadening

It already has been pointed out that electrons ejected in the projectile rest frame with the same velocity $v'$ will be detected in the laboratory frame with velocity $v$, the value of which depends on the observation angle $\theta$ (Eqs. **??** and **??**). Therefore, two electrons with the *same* energy in the projectile frame, but emitted at two different angles $\theta'_1$ and $\theta'_2$, respectively, will be detected in the laboratory frame at two *different* energies $\epsilon_1(\theta_1) \neq \epsilon_2(\theta_2)$. Assuming that the emission angles of the two electrons of the former example correspond to the angular width $\Delta\theta$ of the spectrometer acceptance angle, i.e., $\Delta\theta = \theta_2 - \theta_1$, the observed energy width $\Delta E$ is then written as: $\Delta E = \epsilon_1(\theta_1) - \epsilon_2(\theta_2)$. As clearly seen from Eqs. **??** and **??**, the observed energy width $\Delta E$ is not a linear function of $\Delta\theta$ but rather depends on the average observation angle $\theta \equiv (\theta_1 + \theta_2)/2$. The situation is geometrically illustrated in Fig. **??**, where it is indicated that the observation at zero-degrees ($\theta = 0°$) reduces substantially the observed energy width $\Delta E$. As a rule, the finite spectrometer solid angle results in the overlap between two neighboring peaks, degrading in this way the energy resolution of the spectra. The effect is referred to as the kinematic *broadening* effect [?].

The broadening can be understood algebraically as the uncertainty of the two variables, the laboratory observation angle $\theta$, and the cusp energy t in Eq. **??** or **??**.

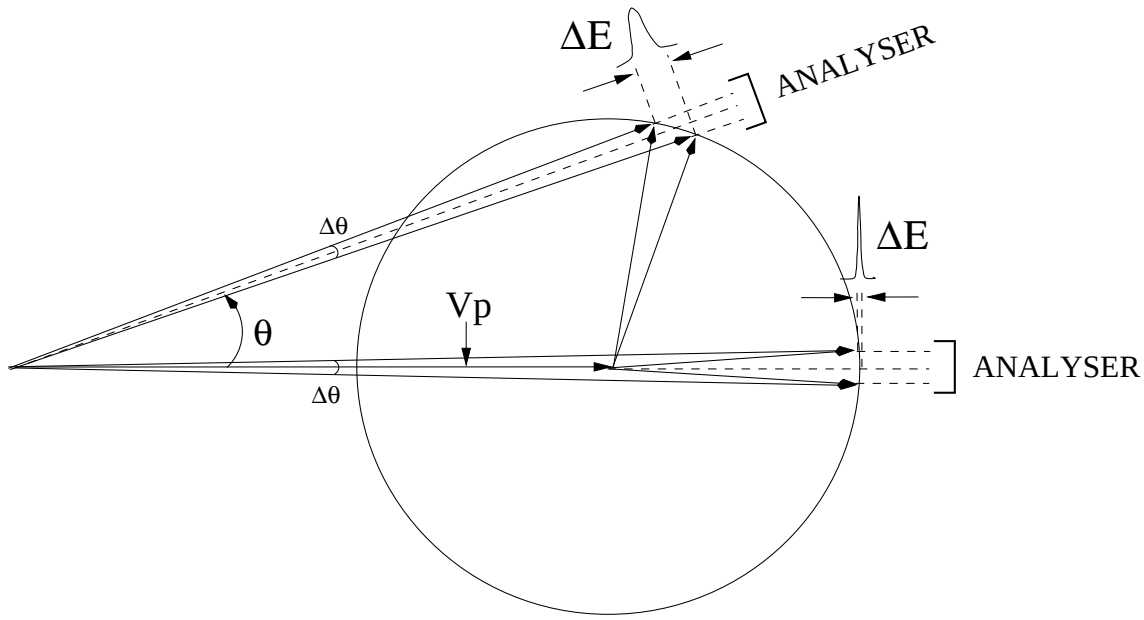


Figure 7: Geometrical interpretation of the broadening effect due to the laboratory observation angle. It is clearly seen how observations at zero-degrees ($\theta = 0°$) have substantially reduced line energy broadening.

A systematic way to estimate the uncertainties of these variables is to expand Eq. **??** or **??** in a Taylor series in powers of $\Delta\theta$ and $\Delta$t:

$$\Delta B_\theta = |\sum_n \frac{\partial^n \epsilon(\theta)}{\partial \theta^n} \frac{(\Delta\theta)^n}{n!}| = |\sum_n \Delta B_\theta^{(n)}| \tag{16}$$

$$\Delta B_t = |\sum_n \frac{\partial^n \epsilon(t)}{\partial t^n} \frac{(\Delta t)^n}{n!}| = |\sum_n \Delta B_t^{(n)}| \tag{17}$$

The broadening $\Delta B_\theta$ due to observation angle $\theta$ can be calculated exactly for each experimental setup since the observation angle is defined geometrically by the dimension of the effective spectrometer acceptance aperture and the distance between this aperture and the target. Even though an easy broadening calculation

is feasible for every spectrometer, the algebraic treatment of the problem provides further insight into the broadening effect. By differentiating Eq. **??** with respect to $\theta$ the first order broadening coefficient in terms of $\theta$ and $\epsilon$ is obtained. Thus

$$\Delta B_{\theta}^{(1)} = -2\sin\theta\Delta\theta \left(\frac{\sqrt{\epsilon t}}{1-\sqrt{\frac{t}{\epsilon}}\cos\theta}\right) \tag{18}$$

For 0° or 180° observations this term vanishes, as can be seen also in Fig. **??**, where the first order broadening coefficient $\Delta B_{\theta}^{(1)}$ is plotted as a function of the laboratory angle $\theta$. In these cases, the second order coefficient must be calculated giving (replacing $\Delta\theta$ with $\Delta\theta/2$ )

$$\Delta B_{0}^{(2)} = \frac{\epsilon}{|1-\sqrt{\frac{\epsilon}{t}}|}\left(\frac{\Delta\theta}{2}\right)^2 \tag{19}$$

$$\Delta B_{\pi}^{(2)} = \frac{\epsilon}{1+\sqrt{\frac{\epsilon}{t}}}\left(\frac{\Delta\theta}{2}\right)^2 \tag{20}$$

The relative broadening $\Delta B^{(2)}/\epsilon$ for both 0° and 180° is thus given by the following simple result: [?]

$$\frac{\Delta B_{0,\pi}^{(2)}}{\epsilon} = \zeta\left(\frac{\Delta\theta}{2}\right)^2 \tag{21}$$

while the absolute broadening can be expressed as a function of $\epsilon'$:

$$\Delta B_{0\pm}^{(2)} = \epsilon'(1\pm\zeta)^2\zeta\left(\frac{\Delta\theta}{2}\right)^2 \tag{22}$$

$$\Delta B_{\pi}^{(2)} = \epsilon'(1-\zeta)^2\zeta\left(\frac{\Delta\theta}{2}\right)^2 \tag{23}$$

An important conclusion is that the observation at zero-degrees *substantially* reduces the broadening due to the observation angle $\theta$. In Fig. **??** the geometrical

interpretation of this phenomenon is explained. In Fig. **??** (left), where the first order coefficient $\Delta B^{(2)}_{0,\pi}/\epsilon$ is plotted as a function of the detection angle $\theta$, it is clearly seen that broadening is maximized for the detection angle of 60°, while it diminishes for the detection angles of 0° and 180°. In Fig. **??** (right) the second order reduced broadening coefficient $\Delta B^{(2)}/\epsilon$ is plot as a function of the rest frame electron energy $\epsilon'$ for various projectile energies, at forward and backward angles. It is clearly seen that for high energy electrons (KLL-Auger, binary encounter) the broadening is negligible, but for low energy electrons (Coster-Krönig, Rydberg) it becomes significant. The present experimental setup utilizes a spectrometer with a full acceptance angle of $\Delta\theta$=0.868°, which is ideal for studying high energy electrons.

Finally, the second order broadening coefficient $\Delta B^{(2)}_{0+}$ for the negative solution (emission angle $\theta' = 180°$) is much smaller than the value of the broadening for the positive solution $\Delta B^{(2)}_{0-}$ (emission angle $\theta' = 0°$). Still, the energy resolution due to broadening $\Delta B^{(2)}/\epsilon$ is the same in both cases, as it can be clearly seen from Eq. **??**.

The uncertainty in the beam energy is another factor which leads to line broadening. Expanding Eq. **??** to first order in $\Delta t$ for $\theta = 0$ gives:

$$\Delta\epsilon_t \;=\; |1 \pm \frac{1}{\zeta}|\;\Delta t \qquad\qquad (\theta = 0°) \tag{24}$$

A beam energy spread of $\Delta$t/t = 1×10$^{-3}$ is characteristic to the J. R. Macdonald Laboratory tandem Van de Graaff accelerator.

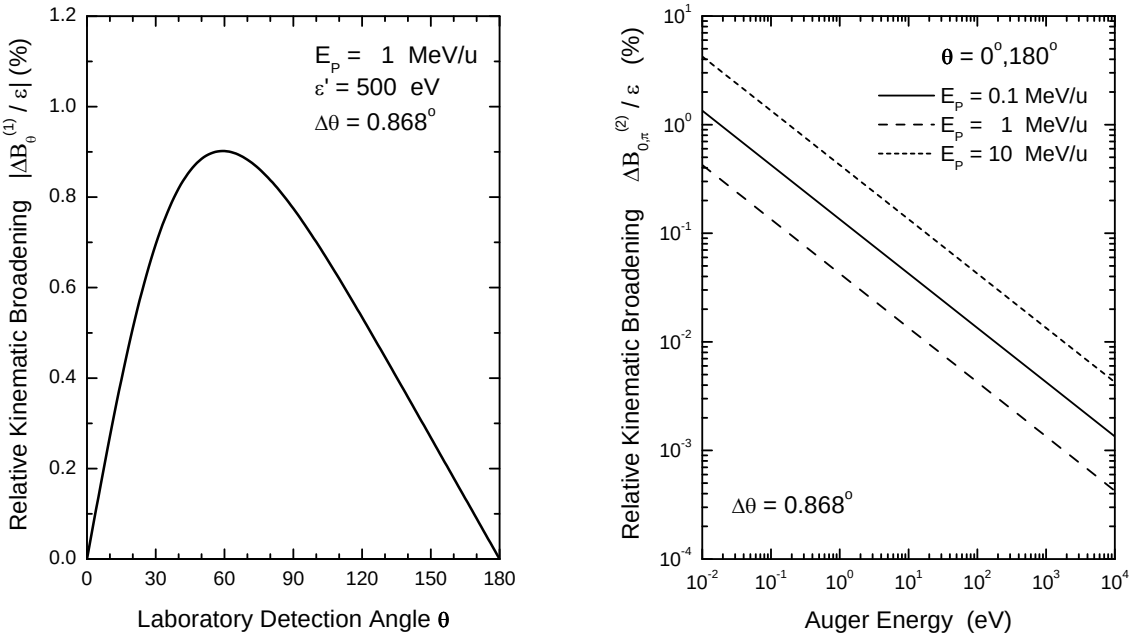


Figure 8: [*Left*] First order relative broadening coefficient $\Delta B_\theta^{(1)}/\epsilon$ as a function of the laboratory angle $\theta$. [*Right*] Second order relative broadening coefficient $\Delta B^{(2)}/\epsilon$ as a function of the Auger electron energy $\epsilon'$ for laboratory observation angles $\theta = 0°$ and 180°. In all cases the acceptance angle is $\Delta\theta = 0.868°$.

However, when the post-stripping method is used to obtain a certain charge state of an ion, an additional beam energy spread should be considered due to the beam straggling in the post-stripper foil [**?**, **?**].

A broadening, may be considered also from the uncertainty of the variable $\epsilon'$ in Eq. **??**. $\Delta\epsilon'$ in this case will be the intrinsic width of the Auger line and will be transformed to $\Delta\epsilon$ in the laboratory frame according to Eq. **??**. This kind of broad-

ening though is actually a stretching and therefore the kinematic transformation of the intrinsic width $\Delta\epsilon'$ cannot be considered as a broadening. However, in order to estimate the width of a peak in the laboratory frame this factor also should be considered.

Finally, the overall kinematic broadening is calculated by adding in quadrature all the kinematic broadening factors discussed previously, the energy width of an Auger line can be estimated in first order non-vanishing terms at zero-degrees observation angle as:

$$\Delta\epsilon = \sqrt{\left[\epsilon'(1 \pm \zeta)^2\zeta\right]^2 \left(\frac{\Delta\theta}{2}\right)^4 + \left[1 \pm \frac{1}{\zeta}\right]^2 (\Delta t)^2 + \left[1 \pm \zeta\right]^2 (\Delta\epsilon')^2} \qquad (25)$$

This energy width constitutes the lowest permissible limit to the measured resolution, defining the limit of the experimental energy resolution. The quantity $\Delta\epsilon/\epsilon$ should always be compared to the smallest attainable instrumental energy resolution $\Delta\epsilon_I/\epsilon$ in order to have an estimate on the possible spectral identification of closely neighboring Auger lines. The major component of the broadening at 0° is usually due to instrumental effects and usually not due to the beam energy spread. However, in the case where the beam is obtained by post-stripping in a foil, the effect of increased beam spread is observable.

## 2.3 Impulse Approximation

In the Impulse Approximation (IA) the interaction between a fast projectile and a relatively slow target electron is treated in a way so that the collisional response of the nucleus to which the electron is bound is neglected. The IA was initially implemented in RTE studies [**?**], and since then it has been successfully applied to other $e-e$ processes in ion–atom collisions, such as electron-electron Excitation [?], electron-electron Ionization [?,?], Inelastic Resonant scattering [?] and Super-Elastic Scattering [**?**], providing a unified approach for dealing with all target-electron – projectile-electron interactions [**?**].

In the Impulse Approximation, the target electron is considered frozen during the collision time, provided that the collision velocity $V_p$ is large compared to the velocity of the target electron $v_t$, i.e., $V_p/v_t >> 1$ [?]. Thus, in the projectile rest frame, the electron can be treated as a quasi-free particle approaching the projectile nucleus with a velocity $\mathbf{v} = \mathbf{V_p} + \mathbf{v_t}$. Then, the quasi-free electron impact energy in the projectile frame will be written as: [?]

$$\epsilon' = \frac{1}{2}\, m\, \mathbf{v}^2 = \frac{1}{2}\, m\, V_p^2 + p_z \cdot V_p + \frac{p_x^2}{2m} + \frac{p_y^2}{2m} + \frac{p_z^2}{2m} \tag{26}$$

where $p_j = m\, v_j$ is the momentum component in the $j = x, y, z$ directions and $m$ the electron mass. Brandt [?] in his RTE - IA treatment, neglected the $p_j^2$ terms for small electron velocities, $v_{t_j} << V_p$. Itoh [?] *et al.*, also neglected the $p_j^2$ terms, but subtracted the ionization energy of the active target electron $E_I$ as a correction.

Lee [?] *et al.*, improved agreement between the IA model and experiment by keeping the $E_I$ correction along with the $p_z^2$ term. Following Lee's IA model, Eq. **??** is written for the *i-th* target quasi-free electron as:

$$\epsilon' = \frac{1}{2}\, m\, V_p^2 + p_{z_i} \cdot V_p + \frac{p_{z_i}^2}{2m} - E_{I_i} \tag{27}$$

Thus, within the IA, the DDCS in the projectile frame for the ion-atom collision, $\frac{d^2\sigma}{d\Omega'\, d\epsilon'}$, can be related to the SDCS for the free electron-ion collision, $\frac{d\sigma}{d\Omega'}$, as follows (atomic units):

$$\frac{d^2\sigma(\epsilon', \theta')}{d\Omega'\, d\epsilon'} = \sum_i \left(\frac{d\sigma(\epsilon', \theta')}{d\Omega'}\right) \left(\frac{J_i(Q_i)}{V_p + Q_i}\right) \tag{28}$$

where

$$Q_i \equiv p_{z_i} = \sqrt{2}\sqrt{\epsilon' + E_{I_i}} - V_p \tag{29}$$

obtained by solving Eq. **??** for $p_z$, and

$$J_i(Q_i) = \int\int dp_{x_i} dp_{y_i} |\psi_i(\mathbf{p}_i)|^2 \tag{30}$$

is the Compton profile, which gives the probability of finding a specific target electron $i$ with a z-momentum component $Q_i$ , where z is the direction of the projectile velocity. $\psi_i(\mathbf{p}_i)$ is the *i-th* electron wavefunction in momentum space while $n_i$ is the number of electrons in the *i-th* subshell. The single differential cross section $\frac{d\sigma}{d\Omega'}$ is considered to be a function of the free electron impact energy $\epsilon'$ and the scattering angle $\theta'$. The sum index $i$ in Eq. **??** should run over all target electrons satisfying the basic IA assumption, i.e., $V_p >> v_{t_i}$.

Calculated Hartree-Fock Compton profiles are available in the literature [**?**]. For $H_2$ and He targets, analytic expressions have been derived from fits to X-ray measurements [**?**].

### 2.3.1 Rutherford Scattering Model

The single differential cross-section for a free electron colliding with a bare nucleus of charge $Z_p$ is successfully described by the Rutherford scattering model and is given in atomic units by: [**?**]

$$\frac{d\sigma(\epsilon', \theta')}{d\Omega'} = \left[\frac{Z_p}{4\,\epsilon' \sin^2\left(\frac{\theta'}{2}\right)}\right]^2 \tag{31}$$

where primed symbols refer to the projectile rest frame.

Substituting Eq. **??** in Eq. **??**, the DDCS of a quasi-free electron scattered at 180° (zero-degree laboratory observation angle, $\theta = 0°$) from a bare nucleus is described under the IA - Rutherford treatment as:

$$\frac{d^2\sigma(\epsilon', \theta' = 180°)}{d\Omega'\, d\epsilon'} = \left[\frac{Z_p}{4\,\epsilon'}\right]^2 \sum_i \frac{n_i\, J_i(Q_i)}{V_p + Q_i} \tag{32}$$

The laboratory frame Rutherford DDCSs are obtained according to the transformations described by Eqs. **??** and **??**. In Fig. **??**, theoretically calculated IA - Rutherford BEe DDCSs, illustrating the dependence on the projectile energy, the nuclear charge and the Compton profile, are shown in the laboratory frame. The Compton profiles of $H_2$, He and Li are also shown in Fig. **??** (top) for comparison.

The Rutherford SDCS, a smoothly varying function is convoluted with the Compton profile of target electrons, resulting in the BEe peak shape that is shown in Fig. **??** (bottom) for $Z_p = 9$ and scattering angle of $\theta' = 180°$. It should be mentioned here that the Li(1s) electrons do *not* satisfy the IA basic assumption $V_p >> v_{t_i}$, and therefore were not included in the calculations.

### 2.3.2 Elastic Electron Scattering Model

BEe production from fast collisions of ions with $H_2$ targets can be described within the IA as the elastic scattering of quasi-free electrons in the statically screened field of the projectile nucleus including electron exchange effects. This is also known as the Elastic electron Scattering Model (ESM). In the ESM calculations described by Bhalla *et al.* [**?**], the static potential and nonlocal exchange contributions are computed in a self-consistent Hartree-Fock atomic model. The Coulomb phase shift and the additional phase shifts due to screening and exchange effects are calculated using a partial wave treatment. The details of the calculation can be found in Refs. [**?**, ?, **?**] The ESM code, which was used for comparison to the experimental data, was generously provided to me by Prof. C.P. Bhalla.

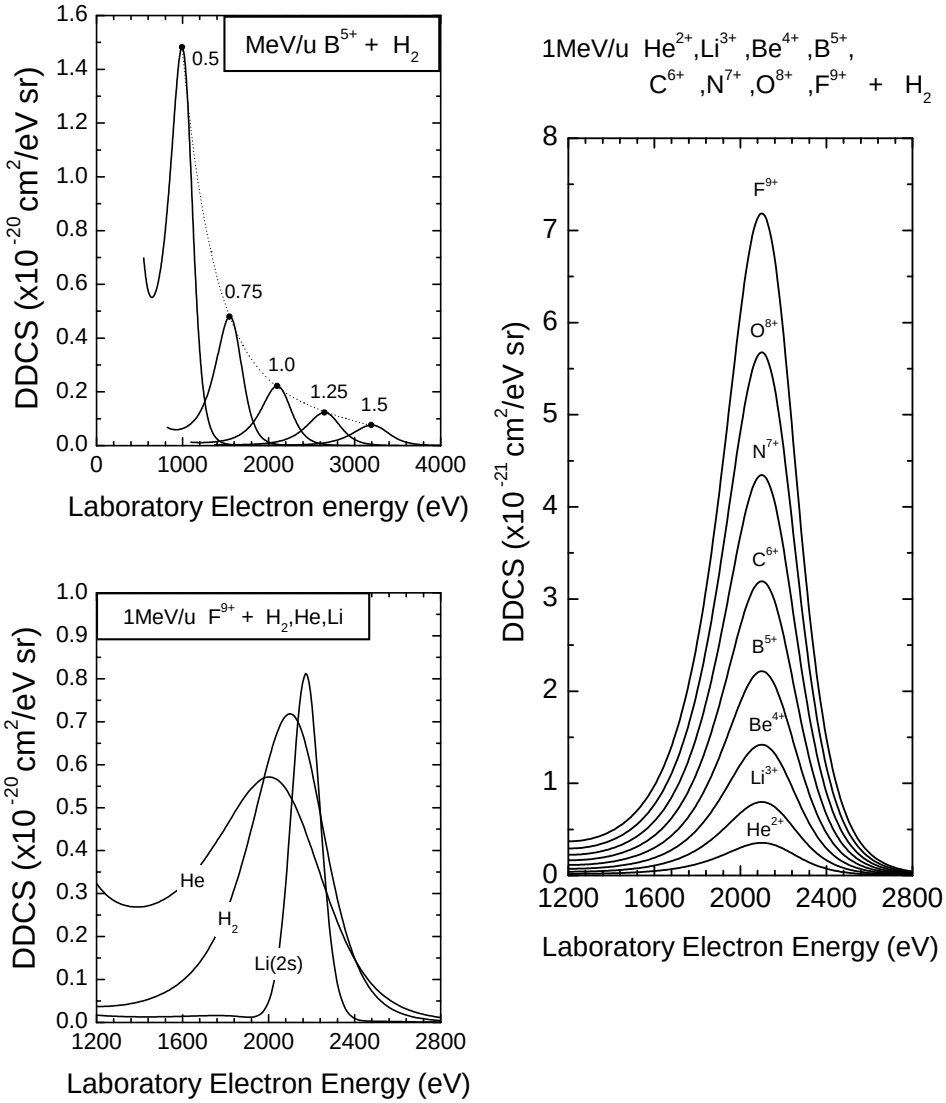


Figure 9: Theoretically calculated IA–Rutherford BEe DDCSs. [*Top-Left*]BEe DDCSs in collisions of $B^{5+} + H_2$ as a function of the projectile energy. [*Bottom-Left*] BEe DDCSs in collisions of 1 MeV/u $B^{5+} + H_2$, $He$ and $Li$ targets. [*Right*] BEe DDCSs in collisions of 1 MeV/u $Z_p^{Z_p+} + H_2$, where $Z_p$ is the projectile atomic number, as a function of bare nucleus charge.

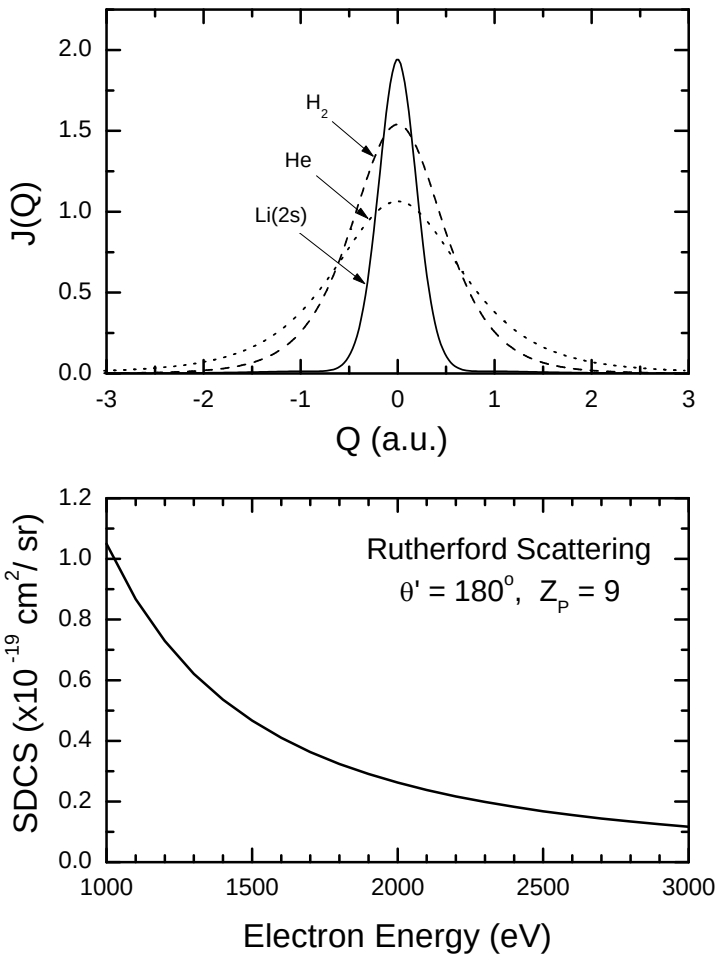


Figure 10: [*Top*] Compton profiles for $H_2$, He and Li. [*Bottom*] The single differential Rutherford cross section for nuclear charge $Z_p = 9$ and scattering angle of $\theta' = 180°$.

## 2.4 Conclusions

In summary, Zero–degree projectile spectroscopy is shown to be a very powerful tool for high resolution studies of projectile electrons and related phenomena. The

strength of ZAPS lies in the kinematic advantages of broadening minimization at 0°, the access to the whole electron energy spectrum, and the ability to detect very low energy electrons. To date, the ZAPS technique has utilized two-stage (tandem) slit spectrometers providing unique information on state-selective differential cross-sections for basic collision mechanisms. However, tandem slit spectrometers' greatest disadvantage is the large amount of time consumed to collect a single spectrum. The use of very small apertures (1–2 mm for the second stage analyser) along with the dramatic transmission reduction in the deceleration mode of operation, necessitates the use of relatively large beam currents (typically 50–100 nA) to maintain experimental acquisition times at the 12–24 hr. level. A typical high resolution spectrum needs at least 24 hours of data recording. Therefore, experiments utilizing low beam currents ($< 10$ nA) or attempting to measure very low cross section processes (DDCS $< 10^{-22}$ cm$^2$ / eV sr) are practically forbidden for parallel plate tandem spectrometers.

In this work, a position sensitive detector instead of an exit slit is used in a single stage hemispherical deflector analyser (HDA), which increases the data collection efficiency by more than a factor of 100. Even though such a spectrometer is typical in today's modern electron spectroscopy for chemical analysis (ESCA) experiments, its utilization at zero-degrees entailed special considerations, since small slits could not be used at the entrance. Instead, a focusing/decelerating lens system is incorporated, resulting in a virtual slit entrance by focusing while at the same time decelerating

the electrons for improved energy resolution.

Table 1: The doubling, shifting, stretching and enhancing frame transformation kinematic effects of an Auger peak are summarized for $\theta = 0°$ detection. All the possible cases are determined by the projectile rest frame emission angle $\theta'$ and the relation between the projectile velocity $V_p$ and the electron velocity at the projectile rest frame $v'$.

| $\theta'$ | $v'$ | $t$ | $\zeta$ | Doubling | Shifting | Stretching | Enhancement |
|---|---|---|---|---|---|---|---|
| | | $\frac{1}{2}mV_p^2$ | $\sqrt{\frac{t}{\epsilon'}}$ | | $\frac{\epsilon}{\epsilon'} = (1 \pm \zeta)^2$ | $\frac{\Delta\epsilon}{\Delta\epsilon'} = \lvert 1 \pm \zeta \rvert$ | $\frac{\frac{d^2\sigma}{d\Omega d\epsilon}}{\frac{d^2\sigma}{d\Omega' d\epsilon'}} = \lvert 1 \pm \zeta \rvert$ |
| 0 | $v' \geq V_p$ | $\epsilon' \geq t$ | $\zeta \leq 1$ | NO | $> 1$ | $> 1$ | $> 1$ |
| 0 | $v' < V_p$ | $\epsilon' < t$ | $\zeta > 1$ | YES | $> 1$ | $> 1$ | $> 1$ |
| $\pi$ | $v' < \frac{V_p}{2}$ | $\epsilon' < \frac{t}{4}$ | $\zeta > 2$ | YES | $> 1$ | $> 1$ | $> 1$ |
| $\pi$ | $v' = \frac{V_p}{2}$ | $\epsilon' = \frac{t}{4}$ | $\zeta = 2$ | YES | 1 | 1 | 1 |
| $\pi$ | $\frac{V_p}{2} < v' < V_p$ | $\frac{t}{4} < \epsilon' < t$ | $1 < \zeta < 2$ | YES | $< 1$ | $< 1$ | $< 1$ |
| $\pi$ | $v' \geq V_p$ | $\epsilon' \geq t$ | $\zeta \leq 1$ | NO ELECTRON DETECTION AT $\theta = 0°$ | | | |

# 3 Experimental Arrangement

## 3.1 Experimental Setup

The experimental setup was developed at the J. R. Macdonald Laboratory at Kansas State University (KSU) by E.P. Benis and T.J.M. Zouros [**?**]. A top view of the laboratory is shown in Fig. **??**. The ion beam is obtained at the desired energy from the tandem Van de Graaff accelerator and transferred to the experimental area. Negative ions are produced by the sputter ion source, extracted from the source at an energy of approximately 70 keV and mass-analysed by a 20° analysing magnet. They are then injected into the tandem Van de Graaff accelerator to be accelerated at the terminal voltage, +V. For the KSU tandem $V_{max} \simeq 7\,MV$. The accelerated negative ions reach the tandem tank half way, where the maximum positive terminal voltage, +V, occurs, and collide with a thin carbon foil or a low density gas (usually $N_2$). As a result, negative ions are stripped from their electrons, and the positive ions produced by the collision are furthermore accelerated to the end of the tandem tank, which is at the ground potential. The final energy gain for an ion of initial and final mass $m_i$ and $m_f$, respectively, and final charge q is $E = (q + m_f/m_i)V$. Usually $m_f$=$m_i$ (i.e. $F^{q+}$ ions are obtained from $F^-$) and then the energy gain is E

= (q + 1) V, with energy measured in MeV and the terminal voltage in MV.

The stripping process inside the accelerator produces a distribution of charge states at different intensities and energies. The charge-state and energy of the beam are pre-determined to maximize the final beam intensity.

The charge q-distribution of the foil-stripping process can be estimated using *Marrion and Young* [**?**] nuclear reaction analysis table. In the JRM laboratory, the expected current of all charge states is predicted within the order of magnitude using the TANDEM program.

The charge-state selection is obtained in the first 45° analysing magnet (see Fig. **??**). The magnet was calibrated with an NMR device, which is more accurate than the terminal voltage meter. For this reason, the analysing magnet is set at the Hall Probe Voltage value (HPV) determined by the NMR frequency, and the terminal voltage is tuned in order to maximize the beam current in the current meter (Faraday Cup) after the analysing magnet. A feedback system, using the difference of the beam currents measured at a pair of slits placed in between the two 45° analysing magnets, automatically adjusts the beam energy to the one set by the magnet. Therefore, the beam energy along with the beam current are kept constant through the measurement.

After passing the first 45° analysing magnet the ion beam is transferred through a second 45° magnet in order to enter the Linear Accelerator (LINAC). The LINAC can be used to further accelerate or decelerate the ions. After the LINAC the beam

is bent through a 90° magnet to the direction of the beamline in use. It passes at 0° through the first switching magnet and is then bent at 15° left with respect to the beam direction, by the second switching magnet to the experimental setup.

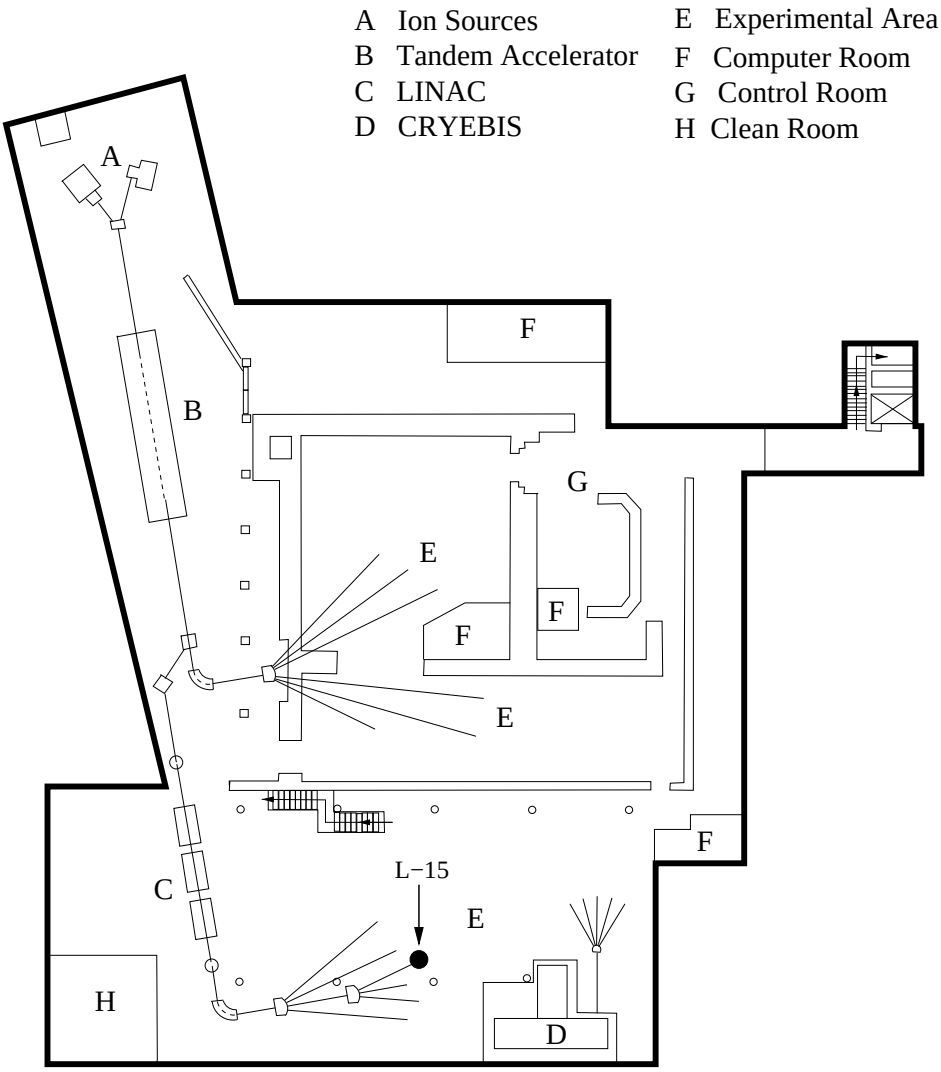


Figure 11: Top view of the J. R. Macdonald Laboratory. The ZAPS experimental station is shown at L-15

The ion beam trajectory is controlled and monitored by magnets, magnetic and

electrostatic deflectors, focusing lenses, valves, Faraday cups and Beam Profile Monitors. It should be noted that the operation of the tandem accelerator and the transportation of the ion beam to the target region are done by the experimenters in the main control room.

In the case that the beam current of a charge state q is predicted to be too low for the experimental requirements by the TANDEM program (i.e. less than ∼50nA for the tandem spectrometer or less than ∼1nA for the hemispherical spectrograph), a technique called "post-stripping" is applied. In this technique a lower charge state, where the beam is more intense, is selected from the first 45° analysing magnet. The lower charge state is further post-stripped by passing through a thin carbon foil (5 $\mu g/\mathrm{cm}^3$) that is placed, via a movable rod, perpendicular to the ion beam direction. These rods are also located in the regions between the two 45° magnets and before the LINAC analysing magnet. The new charge distribution has a maximum current at higher q-values, which may produce more intense beams for higher charge states. The desired charge state for the experiment is then selected from the LINAC analysing magnet and directed up to the experimental region.

The beamline is located on the 15° left (L-15) port of the second switching magnet (see Fig. **??**). Two pairs of 4-jaw slits, separated by a distance of 1m, were used to collimate the beam down to a 1×1 mm$^2$ cross-section. Due to the focusing properties of the switching magnet, the upstream slits were set wider open than the downstream ones. Typical collimation values are 3×3 mm$^2$ and 1×1 mm$^2$ for

the upstream and the downstream slits, respectively. The spatial beam distribution could be monitored with an oscilloscope and a Beam Profile Monitor (BPM). The latter is located between the two pair of slits. The beam current was maximized at the Faraday Cup (FC) after the second pair of 4-jaw slits and then passed through the apertures of the gas-cell and the spectrograph to the last FC (see Fig. **??**), using the switching magnet, the quadrupole and the magnetic deflectors further upstream.

It is very important for Zero-degree Auger Projectile Spectroscopy that the ion beam does not come in contact with any of the spectrograph apertures, since in this case the secondary electron production will dominate and pollute the spectra (especially for a single stage spectrometer). For this reason large apertures with diameters of 4 mm for the lens entrance, 6 mm for the analyser entrance, and 9 mm for the analyser beam exit were used (see Fig. **??**), so that after a tight beam collimation, the current measured at any of the spectrograph apertures resulted in a zero reading. It was found that the spectrum was not affected much by the secondary electron emission produced at the surface of the gas-cell apertures.

Another important issue is that when the beam is obtained by passing through the foil, the current in the last FC decreases with time. This effect reflects the change in the stripping foil thickness, resulting in a slightly lower beam energy and therefore a different beam trajectory through the second switching magnet. It would be a mistake in this case to re-tune the magnet in order to maximize the beam current at the last FC. The different beam energy would result in a shift in

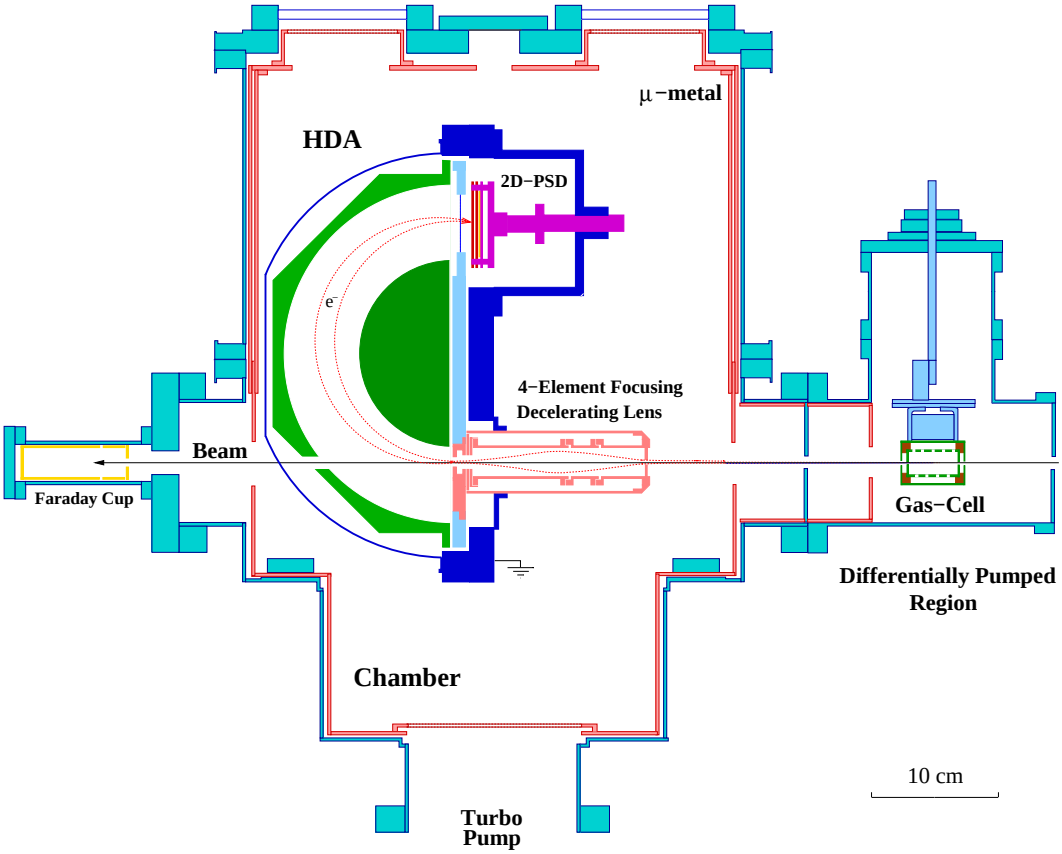


Figure 12: The zero-degree experimental setup from Ref. [?]: The ion beam interacts with a gaseous target in a cell and exits through a hole at the back of the spectrograph. Electrons ejected from the collision in the gas-cell are focused into the hemispherical analyser and detected at the 2D-PSD.

the projectile electron spectrum. Instead, the foil is moved slightly to ensure that the beam collides with an unused part of it. The movable rod, used for replacing the foils, is loaded with 12 foils.

A side view of the zero-degree experimental setup is shown in Fig. **??**. The chamber consists of two cylindrical parts 400 mm diameter each. The lower part of

the chamber supports the hemispherical spectrograph and is mounted on a specially designed base so that it can be moved upwards, sideways or tilted across the beam direction. A connection of the chamber and the beamline pipe via a bellow, allows for an easy alignment of the spectrograph along the beam axis. The chamber alignment is done with the use of a levelled telescope to match the standard for JRM laboratory beamline height of 1.74 m (68.5″). The upper part of the chamber is removable for greater accessibility and manipulation of the components inside.

The chamber is magnetically shielded with an inner cylinder made of $\mu$-metal aimed to reduce the earth's magnetic field to a few mGauss. $\mu$-metal cylinders were also used between the collision region and the chamber. Measurements of the magnetic field inside the chamber, using a magnetic probe, showed that even when the switching magnet – which is located 2 m away from the chamber – was operated at its highest experimentally allowed values, it didn't exceed the value of 10 mGauss in any direction.

The gas-cell consisted of two coaxial cylinders. The inner cylinder was 36mm long with a diameter of 20 mm while the outer cylinder was 50 mm long with a diameter of 34mm. The two cylinders were made of brass and were electrically isolated. Each cylinder had removable entrance and exit circular apertures. The apertures of the outer cylinder were also electrically isolated from the main part of the cylinder, so that the beam current could be monitored at the entrance, middle and exit of the gas-cell. This information was quite helpful in transporting the ion beam through

the cell. Also the electrical isolation of the inner cell from the outer, was used for biasing the inner cell to negative voltage values, in order to accelerate and distinguish between electrons generated inside the gas-cell from those generated outside the gas-cell (as for example in metastable Auger decays). The inner cylinder openings of the apertures were 2.5 mm in diameter, while the entrance and exit openings of the outer cylinder apertures, used in most of the experiments, were 1.5mm and 3mm, respectively. The gas-cell was placed at the top of a 101.6mm (4″) diameter 5-way cross, in front of the chamber. It was mounted on a specially designed movable base so that it could be moved upwards and sideways for easy alignment of the whole apparatus. The distance between the center of the gas-cell and the entrance of the lens was 264mm.

## 3.2 Vacuum

The chamber was pumped by a 450 l/s turbomolecular pump while the target area was differentially pumped through a 250 l/s turbomolecular pump. Two cylindrical baffles were placed on either side of the gas-cell to further improve the differential pumping. The chamber pressure was measured with a thermocouple and an ion gauge, controlled automatically by the Ion Gauge Controller (Kurt J. Lesker model 4400). The gas pressure was measured by a baratron manometer (MKS model 390HA) connected to a feedback system (MKS: needle valve model 248A, controller model 250B, signal controller model 270) so that the measured pressure remained at

a predetermined fixed value during the measurement. The rest of the beamline up to the switching magnet (about 2 m long) was pumped by a 170 l/s turbomolecular pump. Viton O-rings were used in all joints. After pumping, while heating the system using fiber lines up to 70 °C for many weeks, a base chamber pressure of $1.5 \times 10^{-7}$ Torr was achieved. A study of the chamber pressure as a function of the gas-cell pressure was performed in Ref. [?] for $H_2$ and He gases. The results are shown in Fig. **??**.

The reason for higher chamber pressures in the case of $H_2$ compared to He can be understood qualitatively according to the following arguments. The effective pumping speed of $H_2$ is higher than the effective pumping speed of He. This means that the pressure measured at point x will be higher for $H_2$. Actually, it can be shown that $P_{H_2} \simeq (\frac{C_{H_2}}{C_{He}})^2 \; P_{He}$ with $C_{H_2} > C_{He}$, where $C_{H_2}$ and $C_{He}$ are the conductances for $H_2$ and He, respectively. Therefore, part of the difference is due to the different effective pumping speeds. Also the sensitivity of the ion gauges to these two gases is different. The sensitivity for $H_2$ is about 3 times higher than for He. This means that the pressure reading for $H_2$ will be about 3 times higher than for He. It should be mentioned here that the baratron used for measuring the gas-cell pressure reads the actual pressure independent of the gas. Fig. **??** (right), showing the ratio of the chamber pressure with $H_2$ gas in use to the chamber pressure with He gas in use as a function of the gas-cell pressure is plotted, indicates that the two previous arguments

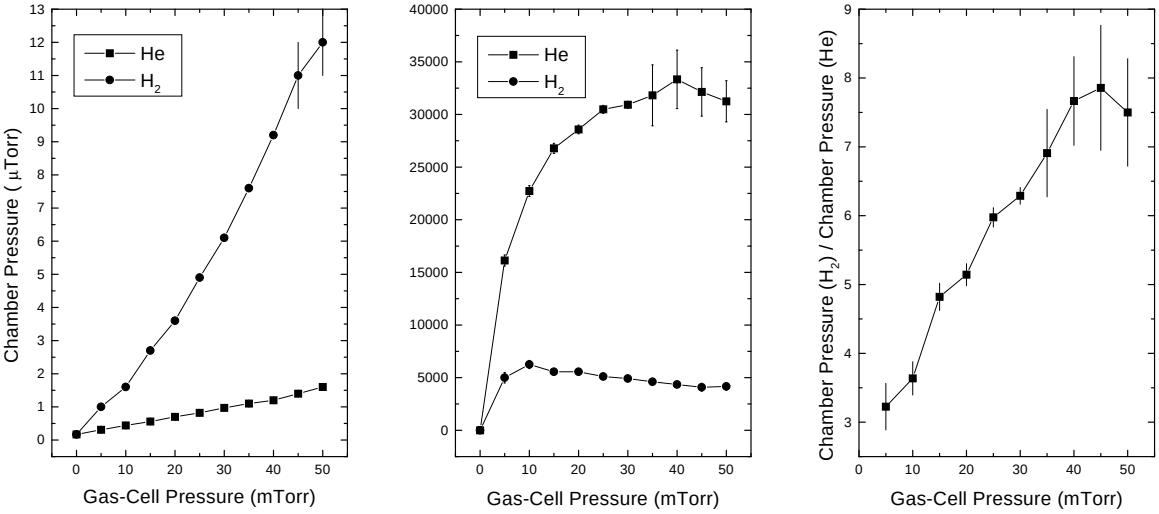


Figure 13: [*Left*] Chamber pressure as a function of the gas-cell pressure for the gases of $H_2$ and He. [*Middle*] Ratio of gas-cell pressure to chamber pressure as a function of the gas-cell pressure. An average ratio of about 30,000 for He targets is established at gas-cell pressures between 15 and 50 mTorr, while an average ratio of about 5,000 for $H_2$ targets is established at gas-cell pressures between 5 and 50 mTorr. [*Right*] Ratio of the chamber pressure with $H_2$ gas in use to the chamber pressure with He gas in use as a function of the gas-cell pressure.

do not justify the ratio behavior. It predicts a fixed difference between the two gas cases but not a gas-cell pressure dependent one. This gas-cell pressure dependence can be understood if a back-streaming is established in the turbomolecular pump of the differentially pumped region. Unfortunately there were not any gauge meters used in the differentially pumped region for measuring the foreline pressure, therefore there is no direct way to justify this statement.

In conclusion, an average gas-cell pressure to chamber pressure ratio of about 30,000 for the case of He and 5,000 for the case of $H_2$, was established, for gas-cell pressures ranging form 15 to 50 mTorr and 5 to 50, respectively, as can be clearly seen in Fig. **??** (middle).

## 3.3 The Spectrograph

The spectrograph, utilizing a hemispherical analyser, a 4-element focusing lens and a two-dimensional position sensitive detector (2D-PSD) is shown in Fig. **??**. Both the analyser and lens were made of aluminum with their inner surfaces coated by soot to reduce secondary electron emission [**?**]. An additional shield placed around the outer hemisphere was found to be necessary, substantially reducing background electrons. The four-element focusing lens, which is illustrated in detail in Fig. **??**, provides a virtual slit for the incoming electrons by focusing them at the entrance of the analyser. The lens also can be used to decelerate the electrons (high resolution or deceleration mode) while focusing them for improved energy resolution. The entrance lens element $V_{L6}$ is always grounded, while the exit lens element is on potential $V_{L2} = V_P$, which is also grounded when running in the low resolution (non-deceleration) mode. The 2D-PSD consists of a pair of 40 mm active area multichannel plates (MCP) and a resistive anode encoder (RAE). The entire detection system is mounted in its own cylindrical casing and further shielded from background electrons.

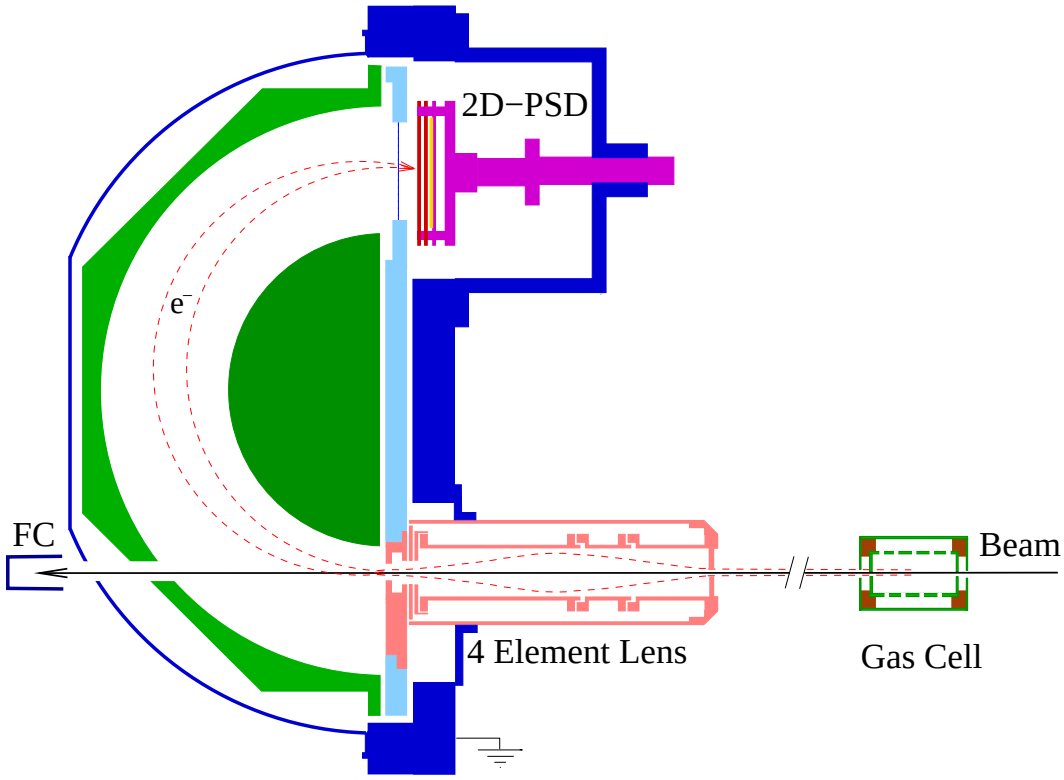


Figure 14: The hemispherical paracentric spectrograph for ZAPS [?]. Note the asymmetric position of the entrance aperture on the analyser. The voltage notation corresponds to the different electrodes. Existing sapphire ball insulation between the different electrodes is not shown. Some important distances of the experimental geometry are given in Table **??**.

The analyser consists of two hemispherical shells with outer $R_2$ and inner $R_1$ radii of 130.8 mm (5.15″) and 72.4 mm (2.85″), respectively. The two shells are supported on a cylindrical base plate from which they are electrically isolated with carefully positioned sapphire ball insulators. The base plate constitutes the relative ground of the analyser and can be biased independently with a plate voltage $V_p$,

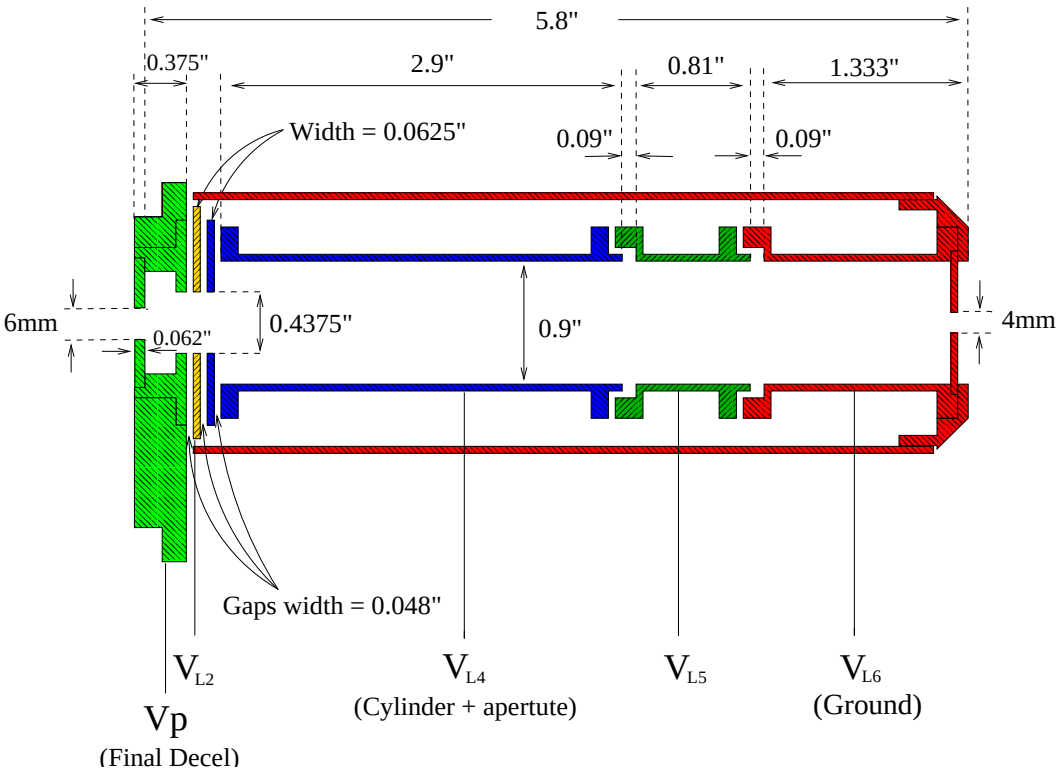


Figure 15: The 4-element electrostatic focusing and decelerating lens.

when deceleration of electrons prior to analysis is required. The four-element lens is also supported from this plate with the exit lens element and base plate being on the same potential $V_p$. Apertures of 4 mm and 6 mm were used at the entrance and exit of the lens, respectively. In the exit part of the analyser there is a 60 mm circular opening where the detector is mounted. The basic geometrical parameters of the ZAPS setup are given in Table **??** at the end of this chapter.

On the exit side of the analyser a 90% transmission nickel grid was stretched over the large exit aperture to shield the inside of the analyser from external fields. This is typically done in all electrostatic spectrometers incorporating a large area PSD. This

grid was also on potential $V_p$. Another 90% transmission grid was also placed on the PSD cylindrical casing about 9 mm from the front of the first MCP. Initially, this grid was placed for controlling the detection energy of the electrons, but along the way, it proved an indispensable component when the spectrograph is run in high resolution mode. That grid was set at slightly more negative voltages than $V_p$ (usually at $V_p$ - 48 V). The two hemispheres with the common base plate are supported on a second plate which constitutes the absolute ground of the spectrograph. Sapphire ball insulators were used for electrical isolation of the various components of the spectrograph.

## 3.4 The Position Sensitive Detector

The two-dimensional position sensitive detector (PSD), consists of two microchannel plates (MCP) of 40mm diameter and a resistive anode encoder (RAE). The use of two MCP at the orientation shown in Fig. **??** is known in the literature as the *Chevron* arrangement. The PSD is mounted on a ceramic base along with the four 1nF capacitors needed for the signal decoupling (see Fig. **??**).

An MCP is an array of $10^4 - 10^7$ channel multipliers (microdynodes) oriented parallel to one another. Typical channel diameters are in the range 10 - 100 $\mu$m and have length to diameter ratios between 40 and 100. A typical distance between microdynode centers is 50 - 150 $\mu$m. A brief summary of the channel multiplication mechanism is given below.

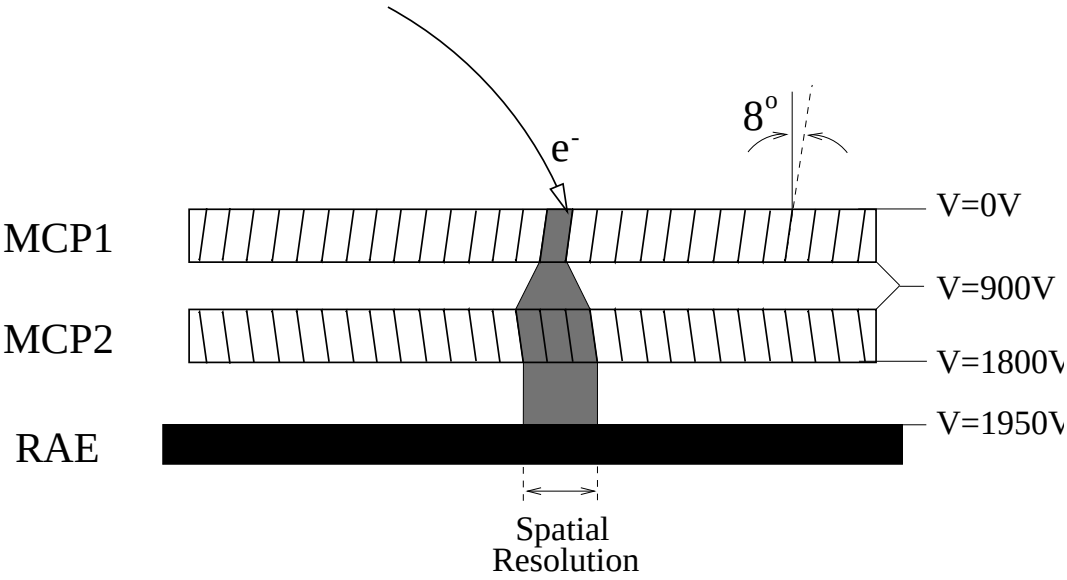


Figure 16: The operation of chevron arrangement microchannel plate (MCP) of use in the HDA Position Sensitive Detector (PSD).

An electron entering a channel of the first microchannel plate produces an average of $\delta^n$ electrons at its exit, where $\delta$ is the average production of secondary electrons per collision with the channel wall, and n is the number of collisions. The procedure is repeated for the second microchannel plate, resulting in an overall amplification factor of $10^6 - 10^7$. Electrons are then collected through an extraction voltage of ~150V on the RAE surface. RAE's resistance is of the order of 1 GΩ. The spot size of the electrons on the RAE determines the spatial resolution of the PSD (see Fig. ??).

Secondary electron yield (known as MCP gain) depends on the overall MCP voltages and is limited by the space charge saturation effects at the rear of the

second MCP. In the saturated operation the output signal does not vary in amplitude with respect to input events, which is the basic assumption for particle detection independent of their energy. Normally, voltages are set at values where maximum gain is established, i.e., where saturation effects appear. The Chevron MCP is a common method for producing space charge saturated output pulses. PSD voltages given in Fig. **??** were typically used.

In the Chevron type MCP, the orientation of the channel axis is tilted at a small angle ($\pm 8°$) with respect to the MCP normal. This geometry inhibits positive ions produced at the output of the rear plate (by electron collisions with the residual gas molecules) to drift back into the channel input, producing additional secondary electrons ("ion after pulses"). The Chevron MCP geometry also forces electrons entering the MCP perpendicular to the channel plate surface, to hit the channel wall early enough, leading to the production of space charge saturated pulses.

## 3.5 Electronics and Data Acquisition System

In Fig. **??** the electronics diagram is shown. Approximately 1pC signals were decoupled by the 1nF capacitors giving rise to small negative pulses of the order of 1mV. [2] The four capacitors, used for the four corner signals, were mounted on the same stand as the MCP inside the vacuum, minimizing in this way any electrical noise that could be picked up by the wires, in case the signal decoupling had taken

[2]Note that $\sim 10^7$ electrons which is the output saturated pulses of the MCP equals $\sim$1pC.

place outside the chamber. The mV signals were driven to the preamplifiers via coaxial cables. Preamplifiers (model PC142IH ORTEC) and dual main amplifiers (model TC247 TENNELEC) were used to produce the final bipolar pulses at the desired amplification, which depended on the input signals of the ADC in use. For example, the AD811 ORTEC model accepted up to 4 Volts peak-to-peak signals while the 7164 PHILLIPS model up to 10 Volts.

The data-acquisition system used at the J. R. Macdonald Laboratory is a VME-based system. Its main hardware components are the CAMAC subsystem, the VME front-end and the back-end host computer. The basic VME front-end consists of a VME crate with one Motorola MVME167 68040 CPU module and one CES CBD-8210 CAMAC branch driver module. The back-end host computer is a VAX station 4000/96 running the XSYS data acquisition software package (Indiana University Cyclotron Facility). Event data may be recorded on a tape or a disk drive attached to the back-end host computer.

The signals from the four corners of the PSD were digitized at the ADC and their pulse height distribution was obtained. The pulse heights were digitized and distributed in 2048 channels as shown in Fig. **??**(a)-(d). It is essential to produce good quality pulse height distributions. Typical electron distributions show a very sharp rise and a long tail (i.e. most electrons give rise to small height pulses, since electrons have lower ionization ability on the MCP dynode surfaces than the ions). The good quality of the PSD image depends primarily on the amplification at the MCPs

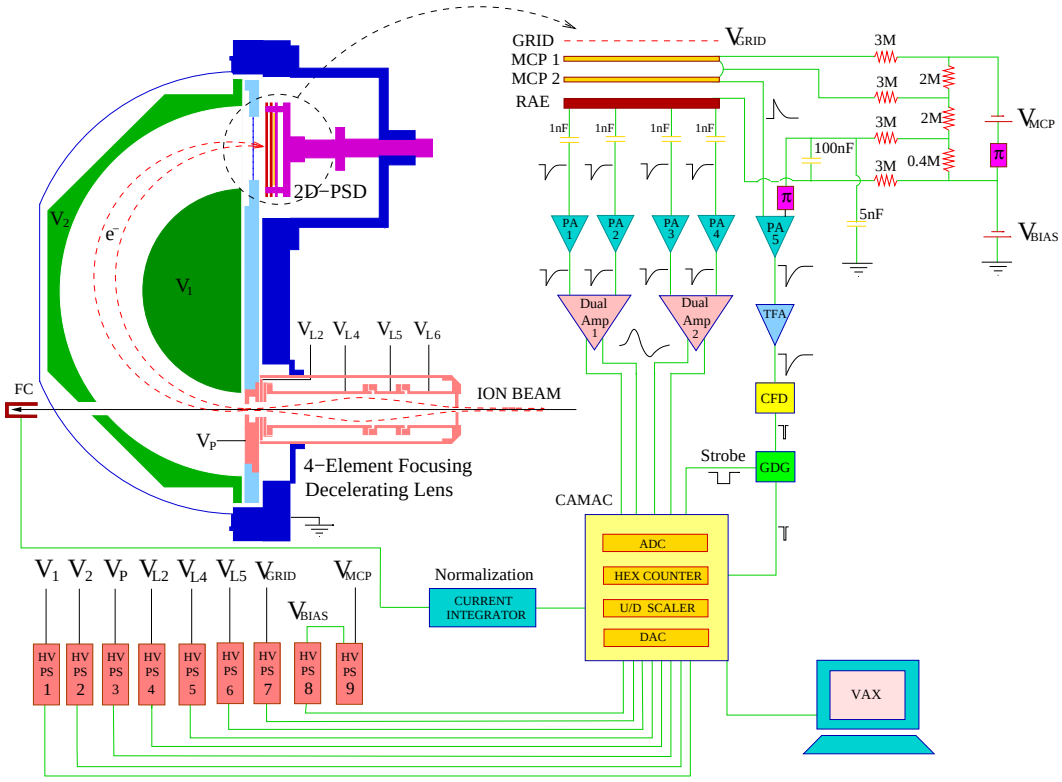


Figure 17: The electronics diagram. PG: Pulse Generator, PA: PreAmplifier, Dual Amp: Dual Amplifiers, TFA: Timing Filter Amplifier, CFD: Constant Fraction Discriminator, GDC: Gate and Delay Generator, ADC Analog to Digital Converter, $\pi$: $\pi$-filter for electronic noise reduction.

(i.e., saturated operation mode). Noise elimination and proper thresholds (Constant Fraction Discriminator) set in the electronics are of considerable importance too.

The position information (X,Y) is derived from the four corner signals ($X_1$, $X_2$, $Y_1$ and $Y_2$) according to the formulas:

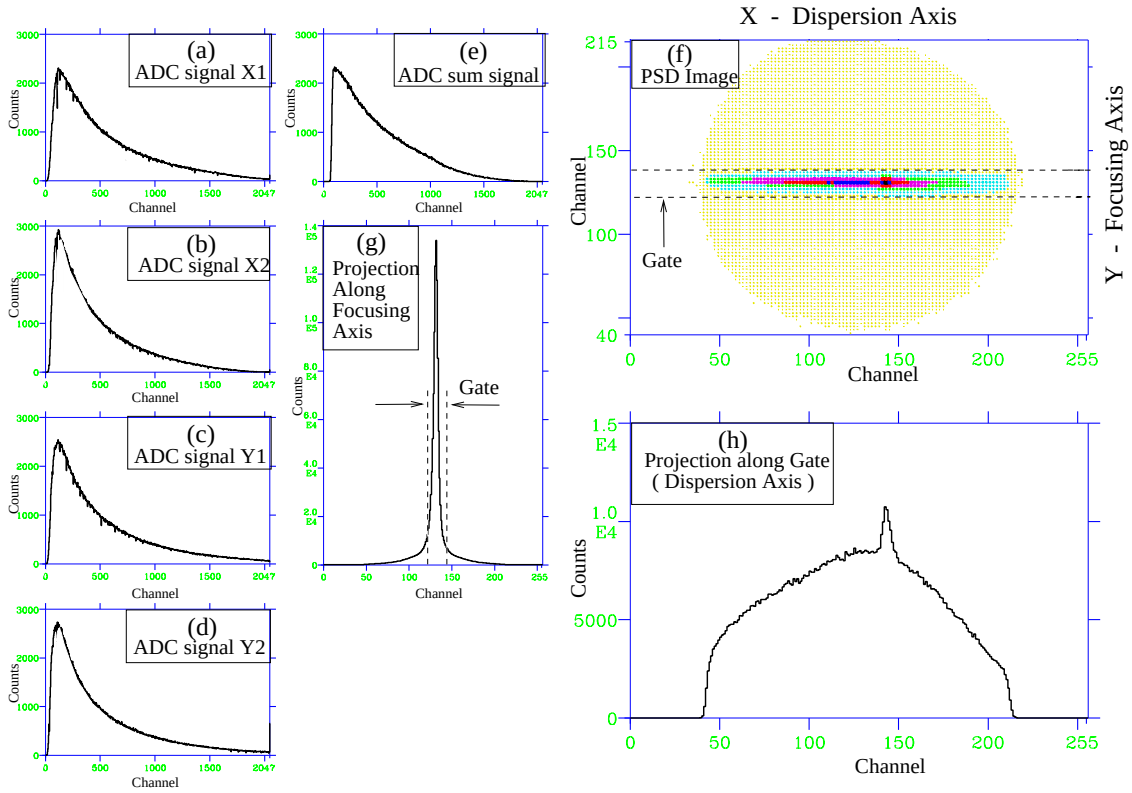


Figure 18: XSYS data acquisition system output. (a) – (d) The four PSD corners pulse height distribution signals. (e) The pulse height distribution of the sum of the four signals. (f) The PSD image constructed from the four PSD corner signals. (g) Projection of the PSD image along the focusing axis. (h) Projection of the PSD image confined by the gate along the dispersion axis.

$$X = \frac{X_1 + Y_1}{X_1 + X_2 + Y_1 + Y_2}, \qquad Y = \frac{X_2 + Y_1}{X_1 + X_2 + Y_1 + Y_2} \tag{33}$$

Therefore a two dimensional image is constructed from the four corner signals, showing the information of the electron position detection of Fig. **??**(f). The dimen-

sion of this 2D array was chosen to be 256×256, which was found adequate without taking up too much disk space. [3]

Due to the double focusing properties of the HDA, the electrons are detected along a narrow strip on the PSD surface as shown in Fig. **??**(f). One could argue that the use of a 2D-PSD instead of a 1D-PSD – since electrons are focused on a narrow strip – is not really essential. However, during the development and mastering of the detection system, the two dimensional information was very helpful in understanding the origin of the background spurious electrons, detected all over the PSD area, especially in high resolution mode. A one dimensional detector would give very poor information on facing the secondary electron emission problem. In addition, the correct circular image of the 2D-PSD is considered to be a sensitive test for checking proper setup operation.

The length of the strip is the dispersion (energy) axis while the width depends solely on the focusing quality of the analyser. Assuming that the magnification of the hemispherical analyser is one, the width would be equal to the focusing trace of the electron beam image at the exit of the lens (entrance of the analyser). A projection of the whole spectrum along the Y-axis (focusing axis) gives a distribution of the

[3] It has been mentioned that the FWHM resolution was measured to be 3.5 channels when an array of 256×256 channels was in use. The use of an array of 128×128 channels would result in a FWHM of 1.75 channels, degrading in this way the energy resolution, as the whole peak would be detected only in three channels, which is not adequate. On the other hand a choice of an array of 512×512 would result in much larger space consumption both in hard disk and memory.

FWHM which can be viewed as the parameter needed to be minimized in order to achieve good focusing conditions.

The spectrum is obtained by setting a gate around the upper and lower ends of the strip width, and projecting the points summed along the y-channels per x-channel, onto the dispersion axis as seen in Fig. **??**(h). The strip width binding box, shown in Fig.**??**(g), corresponds to less than ∼5% of the maximum height of the distribution projected along the focusing axis, when the spectrograph is run in the low resolution mode.

All the above data manipulation was done using the XSYS software data acquisition package. Basic data acquisition codes specialized for the 2D detection were built, in addition to FORTRAN codes, which helped with the software control of the power supply voltages and the general manipulation of the measurement. The "raw" data were seen on the computer screen the way they are presented in Fig. **??**. All the information needed for the proper operation of the system is available in this figure, while most of the changes that can take place during the experiment are computer controlled. Thus, the detection system is largely automated and the experiment can be run easily even by only one experimenter.

## 3.6 Dead Time

Every ADC requires a certain time to digitize the analog input signal in order to send it to the next level of acquisition, i.e., the front-end computer. The time needed

for this conversion process, which is independent of the input signal amplitude and proceeds in parallel for all the ADC channels (inputs), is called "dead time", due to the fact that a pulse will not be counted if it arrives during the conversion time interval. For example, the digitization time of the AD811 ORTEC is 80$\mu$s, while the PHILLIPS 7164 is 7.8$\mu$s. In addition, the data acquisition system itself also has dead time. The dead times involved in the measurement are the following:

- Front end processor overhead: 29$\mu$s
- Time per CAMAC command: 2.5$\mu$s
- Transfer time for word to VAX: 1.6$\mu$s

Four parameters are read from the ADC (the signals of the four corners of the resistive anode) and thus the dead time of the data acquisition system is: $29 + 4\times(2.5 + 1.6) = 45.4\mu$s. Use of the AD811 ORTEC ADC would increase the dead time up to 125.4$\mu$s, while the 7164 PHILLIPS ADC would increase it up to 53.2$\mu$s. The maximum count rates arising from the previous cases are 8kHZ and 19kHz respectively, assuming that the events are regular. However, the random nature of the real events reduces substantially the maximum count rate. In the case of the 7164 PHILLIPS ADC in real experimental conditions, the count rate was limited down to 2kHz in order to have a dead time of less than 30%.

In order to measure absolute cross sections the knowledge of the total dead time of the data acquisition system is needed. For this an output NIM signal from the

Discriminator was used to monitor the real count rate through a CAMAC scaler, which counts up to several MHz without any dead time. (The scaler is reading each pulse and every 5sec it provides the data to the computer while it is still accumulating new data). The ratio of the total counts of the scaler to the total counts of the ADC gives the dead time correction (DTC) that can be used to correct the data.

Table 2: Basic geometrical parameters of the ZAPS setup (see Fig. **??**).

| Quantity | Symbol | Value |
|---|---|---|
| Outer radius | $R_1$ | 72.4 mm |
| Inner radius | $R_2$ | 130.8 mm |
| Paracentric entry | $R_0$ | 82.6 mm |
| PSD diameter | $\mathrm{d}_{PSD}$ | 40 mm |
| Gas-cell length | L | 50 mm |
| Gas-cell apertures diameters | | |
| (Ion beam entry-to-exit) | | 1.5, 2.5, 2.5, 3 mm |
| Gas-cell to lens entry distance | l | 264 mm |
| Lens entry aperture diameter | $\mathrm{d}_{LE}$ | 4 mm |
| Lens exit aperture diameter | | 6 mm |
| Analyser beam exit aperture diameter | | 9 mm |
| Full angular acceptance $\left[= \arctan\left(\frac{d_{LE}}{l}\right)\right]$ | $\Delta\theta$ | 0.868° |
| Full acceptance solid angle $\left[= \frac{\pi d_{LE}^2}{4l^2}\right]$ | $\Delta\Omega$ | $1.8 \cdot 10^{-4}$ sr |

# 4 Metastable Fraction Determination: Theoretical Description

## 4.1 Background and Motivation

Experimental measurements of various collision cross sections for fast He-like ions require quantitative information on the fraction of ions in a long-lived $1s2s\,^3S$ metastable state present in two-electron beams. The knowledge of this fraction is necessary for the absolute cross section measurements of numerous processes including dielectronic recombination, transfer excitation, capture of a target electron, inelastic scattering or recently discovered superelastic scattering of target electrons from highly charged metastable ions [?].

A number of experimental techniques have been developed for the calculation of the metastable fractions over the years, and several measurements of the metastable fraction for various He-like ions have been reported in the literature. However, there are only a few experimental studies available so far that provide systematic information on the energy and foil thickness dependence of the metastable content in these beams [**?**,**?**,**?**]. Terasawa *et al.*, [?] measured the fraction of metastable ions

in fast $F^{7+}$ beams, produced in carbon foils. This study is based on target K x-ray production versus projectile ion charge state in subsequent collisions and relies on a large K-shell to K-shell vacancy transfer cross section. This limits the method to nearly symmetric collision systems with an observable target x-ray yield. The study revealed a relatively high, up to 30%, fraction of $1s2s\,^3S$ ions in the emerging beams, which was not understood by theory. In Ref. [?] the fraction of metastable He ($1s2s\,^3S$) produced by electron-capture of slow (25-90)-keV $He^+$ ions in $H_2$ gas was measured by photon-particle coincidence. The study showed that the fraction of metastable ions was equal to 70%. The same study revealed that the conventional beam attenuation technique [?], which is extensively used for the determination of the metastable fraction, substantially underestimates the metastable population of He-like beams.

Until now, however, the unified treatment that accounts for a wide range of beam energies and target densities, critical for the metastable population of two-electron ions, has not yet come forth. Almost no data are available on metastable ion production in slow collisions with foils, and very little is known about the energy dependence of the metastable content in ion beams produced in collisions with gas targets. That creates a major problem in determining absolute cross sections for collisions with He-like ions, since theoretical calculations are very often unable to predict the correct fractions. Therefore, the goal of the present investigation was to measure the metastable fraction for the He-like isoelectronic sequence to establish a

benchmark for various absolute measurements in metastable ion-atom collisions.

## 4.2 Experimental Technique for the Determination of the Metastable Fraction in He-like Ions

He-like ions produced in collisions of primary beams with foils or gases eventually end up in the ground $1s^2\,{}^1S$ or metastable $1s2s\,{}^3S$ states. The goal is to develop a technique that will allow to determine the fraction of He-like ions in the metastable $1s2s\,{}^3S$ state. The experimental idea is based on measurements of the Auger electron emission from the doubly excited states of Li-like ions, formed in collisions of He-like ions with gas targets $(H_2, He)$, as shown in Fig. **??**. Since the 1s2s2p ${}^4P$ state is produced only from the metastable $1s2s\,{}^3S$ component of the beam, its Auger decay intensity is proportional to the number of ions entering the target area in the $1s2s\,{}^3S$ state. The projectile ground state component can be assessed using the electron emission from the $1s2p^2\,{}^2D$ state, formed by Resonant Transfer Excitation (RTE) from the $1s2s\,{}^1S$ ground state ions. The $1s2p^2\,{}^2D$ state also may be formed by a non-resonant transfer excitation (NTE) from the $1s2s\,{}^3S$ state, however the NTE cross section at the energies used in this study is expected to be negligible [?]. For the given collision parameters, the measured electron yields emitted at zero degrees from these two states are given by

$$Z(\,^4P) = N_m n \sigma_{Capture} \xi_{\,^4P} \eta \Delta\Omega \frac{W_{\,^4P}(\theta)}{4\pi} \tag{34}$$

$$Z(\,^2D) = N_g n \sigma_{RTE} \xi_{\,^2D} \eta \Delta\Omega \frac{W_{\,^2D}(\theta)}{4\pi} \tag{35}$$

where $N_g$ and $N_m$ are the number of projectile ions in the ground and metastable states, respectively, at the final target area, n is the target number density, Z is the Auger yield, $\eta$ is the spectrometer efficiency, $\Delta\Omega$ is the effective solid angle, $\sigma_{RTE}$ and $\sigma_{Capture}$ are the RTE and electron capture cross sections for the formation of the $^2D$ and $^4P$ states, respectively. The $W(\theta)$ factors account for the angular distribution of the Auger electron emission. We assume that the emission from the $^4P$ state is isotropic and, therefore, for zero–degree measurements $W_{\,^4P}(\theta) = 1$. For the RTE angular distribution $W_{\,^2D}(\theta)$ has been calculated according to Refs. [?, **?**].

The metastable beam fraction is defined as the ratio of ions in the metastable $1s2s\,^3S$ state to the total number of ions in the beam

$$F = \frac{N_m}{N_m + N_g} = (\frac{N_m}{N_g} + 1)^{-1} \tag{36}$$

and can be expressed in terms of the electron emission from doubly excited states $^2D$ and $^4P$, using Eq. **??** and incorporating the angular distribution factor $\mathrm{W}^{2D}(\theta)$ into the RTE cross section:

$$F = (\frac{Z(\,^2D)\,\sigma_{Capture}\,\xi_{\,^4P}}{Z(\,^4P)\,\sigma_{RTE}\,\xi_{\,^2D}} + 1)^{-1} \tag{37}$$

Since for both the $^2D$ and $^4P$ states, the parameters n, $\eta$ and $\Delta\Omega$ from Eq. **??** are the same, they do not appear in the expression for the metastable fraction.

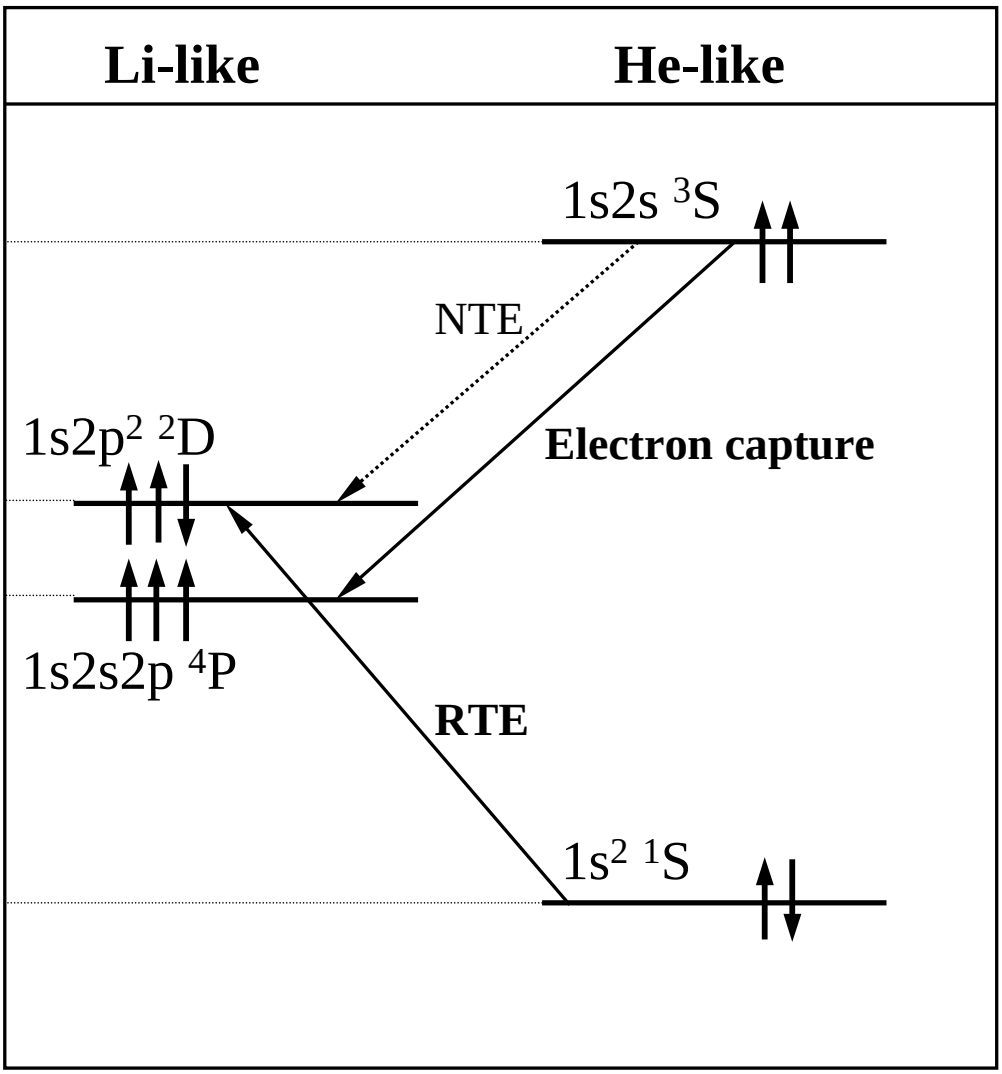


Figure 19: Formation mechanisms of the doubly excited states of Li-like ions resulting from collisions of metastable He-like ($1s^2\,{}^1S, 1s2s\,{}^3S$) beams with gas targets.

This substantially reduces the absolute experimental error since the effects of

the target pressure variation and the uncertainties in spectrometer efficiency as well as in the experimental solid angle are excluded.

The 1s2s2p $^4P$ state is metastable itself with the lifetime [**?**], which is comparable to the ion's time–of–flight in the gas cell, therefore the deexcitation behavior along the projectile trajectory should be taken into account. This correction is made by considering only some fraction, R, of $^4P$ ions that decay inside the gas cell. Numerically, this fraction can be found by integrating over the gas cell, assuming the statistical distribution for all $^4P_J$ states:

$$R = \sum_J a_J \, \xi_{^4P_J} (1 - \frac{L_J \, (1 - e^{1 - \frac{L_{cell}}{L_J}})}{L_{cell}}) \tag{38}$$

here, $L_{cell}$ is the length of the gas cell, $L_J$ is the deexcitation length of an ion in the $^4P_J$ state, given by $L_J = t_{^4P_J} Vp$ , where $t_{^4P_J}$ is the lifetime of the $^4P_J$ state, Vp is the projectile velocity, $\xi_{^4P_J}$ is the Auger yield of the $^4P_J$ state and $a_J$, given by

$$a_J = \frac{2J + 1}{\sum_J (2J + 1)} \tag{39}$$

is the statistical weight of the $^4P_J$ level.

In calculating the metastable fraction, the Auger emission from $^4P$ ions should enter Eq. **??** only if Auger electrons were produced inside the gas cell. Consequently, all the $^4P$ electrons that decayed outside the gas cell need to be excluded from the experimental measurements. This is done by applying a small voltage (20-30 V) to the gas cell, which decelerates all the electrons produced inside of it, splitting the

$^4P$ Auger line in a spectrum in two parts. The area of the Auger peak with the lower energy is then taken into the calculation using Eq. **??**

With these considerations included, the metastable beam fraction is given by

$$F = (\frac{Z(\,^2D)\,\sigma_{Capture}\,R}{Z_{cell}(\,^4P)\,\sigma_{RTE}\,\xi_{^2D}} + 1)^{-1} \tag{40}$$

here $Z_{cell}(^4P)$ is the Auger electron emission from 1s2s2p $^4P$ ions that decay within the gas cell.

The final expression for the metastable fraction, Eq. **??**, relies on experimental parameters – Z($^2D$), $Z_{cell}(^4P)$, obtained from the electron spectra, and theoretical parameters – $\sigma_{RTE}$ , $\sigma_{Capture}$, $\xi_{^2D}$, available in the literature. The Auger yield for the $1s2p^2\,^2D$ state was evaluated from autoionization and fluorescence rates, obtained by running the COWAN code. Since the rates for radiative transitions are much smaller than the Auger rates, the Auger yields for all investigated ions were assumed to be 1. Similarly, the Auger yields for the 1s2s2p $^4P$ state were found to be very close to unity for all Z less than 8. Auger yield for $O^{5+}$ and $F^{6+}$ ions were taken from Ref. [?] and are given in Table **??** below:

The single differential RTE cross section for the $1s^2\,^1S$ to $1s2p^2\,^2D$ transition can be evaluated within the Impulse Approximation (IA) [?], the process, relating electron-ion cross sections to ion-atom scattering, also more recently referred to as the electron scattering model. Within this approximation the RTE cross section is given by

Table 3: Auger yields for the decay from the 1s2s2p $^4P$ state.

| Ion in the Li-like charge state | J = 1/2 | J =3/2 | J = 5/2 |
|---|---|---|---|
| $O^{5+}$ | 0.967 | 0.701 | 0.9998 |
| $F^{6+}$ | 0.928 | 0.416 | 0.9997 |

$$\frac{d\,\sigma_{RTEA}}{d\,\Omega} = \Omega_{RES}\,\frac{J(Q)}{V_p + Q}\,\frac{W(\theta)}{4\pi} \tag{41}$$

where J(Q) is a Compton profile of the target, $V_p$ - projectile velocity, Q is the component of the target electron momentum in the direction of the beam, $\Omega_{RES}$ is the resonant excitation-scattering cross section calculated using the LS-coupling scheme [?], and $W(\theta)$ is the angular distribution factor, which in case of the zero degree electron emission angle $\theta$ simply equals 2L+1. Zero degree RTE cross sections have been measured previously and compared to calculations based on the electron scattering model [?, **?**], resulting in a good agreement. To minimize the error due to the Impulse Approximation, which requires the projectile velocity to be much larger than the orbiting velocity of a target electron, the $H_2$ molecules with loosely-bound electrons were chosen as a target.

The total electron capture cross sections $\sigma_{Capture}$ to the He-like ($1s2s\,^3S$) metastable beam component were obtained assuming isotropic emission of Auger electrons from

the 1s2s2p $^4P$ state. The empirical scaling rule [**?**] was used to derive total capture cross section for the experimental projectile energy range. This technique has been tested by comparing capture cross sections with some available experimental results for the $F^{7+}$ on $H_2$ collision system [?].

One important aspect that needs to be discussed is the possible presence of $1s2s\,^1S$ metastable state in the ion beam, production of which in collisions with foils is inevitable. The lifetime of this state has been used to calculate the fraction of $1s2s\,^1S$ ions at the target area. Table 4 below shows $1s2s\,^1S$ lifetimes and corresponding fractions for beam velocities close to K–shell electron orbiting velocities.

According to Table 4 the lifetime of the metastable $1s2s\,^3S$ state is fairly long compared to the time beams travel to the gas cell, therefore the reduction of the metastable component along the beamline path is negligible. Even in the case of $F^{7+}$ ($1s2s\,^3S$) ions that have the shortest lifetime ($\approx 9\mu s$), 99.7% of the initially produced at 20MeV metastable ions will reach the target. Ions produced in the metastable $1s2s\,^1S$ state will also reach the target (see Table 4). However, the presence of this state does not affect the metastable fraction determination (**??**), since the $^1S$ state ions cannot populate either the $^4P$ state, due to spin conservation considerations or the $^2D$ state, as RTE is energetically not allowed and NTE is negligible. Nevertheless, the metastable fraction should be corrected to include the $^1S$ state at the target area.

Table 4: Lifetimes and fractions of $1s2s\,^1S$ and $1s2s\,^3S$ ion beams that reach the target area at $v_p/v_k$ =1.

| Projectile Z | Lifetime (ms) | | Fraction at the target area, $\lambda$ | |
|---|---|---|---|---|
| | $1s2s\,^1S$ | $1s2s\,^3S$ | $1s2s\,^1S$ | $1s2s\,^3S$ |
| 5 | 0.0055 | 48.0 | 0.820 | 1.000 |
| 6 | 0.00302 | 20.6 | 0.738 | 1.000 |
| 7 | 0.00106 | 3.95 | 0.477 | 0.9998 |
| 8 | 0.000433 | 0.962 | 0.205 | 0.9993 |
| 9 | 0.000198 | 0.277 | 0.036 | 0.9976 |

$$F_{corr} = \frac{N_{^3S}}{N_{gr} + N_{^3S} + N_{^1S}} \tag{42}$$

Assuming statistical population of J levels, a ratio of $N_{^1S}/N_{^3S} = 1/3$ should be established at the stripping region and the correction for the $1s2s\,^3S$ metastable fraction will be expressed as

$$F_{corr} = F\,\frac{1}{1+\frac{\lambda}{3}*F} = F(1 - F*\frac{\lambda}{3}) \tag{43}$$

where $\lambda$ is the fraction of ions initially produced in the $^1S$ state that reached the gas cell (see Table 4). For the observed values of metastable beam fractions ($< 30\%$) the second term in Taylor expansion will not exceed 6-7% and is neglected in this work, as it is well within the experimental uncertainties.

## 4.3 Proposed Model for the Calculation of the Metastable Fraction

In this section an attempt is made to describe production mechanisms of the $1s2s\,^3S$ state in foils for the purpose of numerical predictions of metastable fractions for systems that were not studied experimentally. In order to simplify the theoretical study of the processes contributing to the formation of the metastable He-like ions, the incident beam was assumed to be in the Li-like charge state. The validity of this assumption has been verified by measuring the production of $1s2s\,^3S$ metastable ions in foils using both Li-like and once negatively charged ($B^{1-}$) incident beams. It has been demonstrated that the final fraction of metastable ions was the same. Fig. **??** shows two processes that may contribute to the formation of the $1s2s\,^3S$ state ions in cascading collisions with foil atoms. The first mechanism to be discussed is the ionization of the K-shell electron in the Li-like ion resulting in a $1s2s\,^3S$ state

(Fig. **??**(a)). Its contribution can be evaluated, assuming that the $1s^2\,{}^1S$ ground state ions are produced by the ionization of the 2s electron of the incident Li-like projectile. Using the K, L- shell vacancy production cross sections, estimated by scaling the PWBA calculation for $H^+ + H$ collisions, it was demonstrated that the metastable fraction calculated within this model is only 1.5-2% for the energy range where the maximum is expected. Since this value is significantly lower than the metastable fraction measured in the experiment (26%), the above suggested mechanism is thus shown to have a negligible contribution to the formation of the metastable ions. To confirm this result experimentally, the fractions of metastable $1s2s\,{}^3S$ ions produced by stripping He- and Li-like incident beams were compared and found to be equal within the experimental error.

The second process, contributing to the formation of the $1s2s\,{}^3S$ state is the production of ground state H-like ions followed by subsequent electron capture into the 2s state of the projectile (see Fig. **??**(b)).

Before proceeding with numerical estimates using this assumption, it is possible to run a simple test of the proposed model. The production of $1s2s\,{}^3S$ metastable ions should be proportional to the production of H-like charge state in foils. It is known experimentally that the production of He-like ions in foils and gases yields different metastable fractions (see the next chapter). If we assume that cross sections for electron capture of a 2s electron to H-like ion are approximately equal for both gas and foil targets,

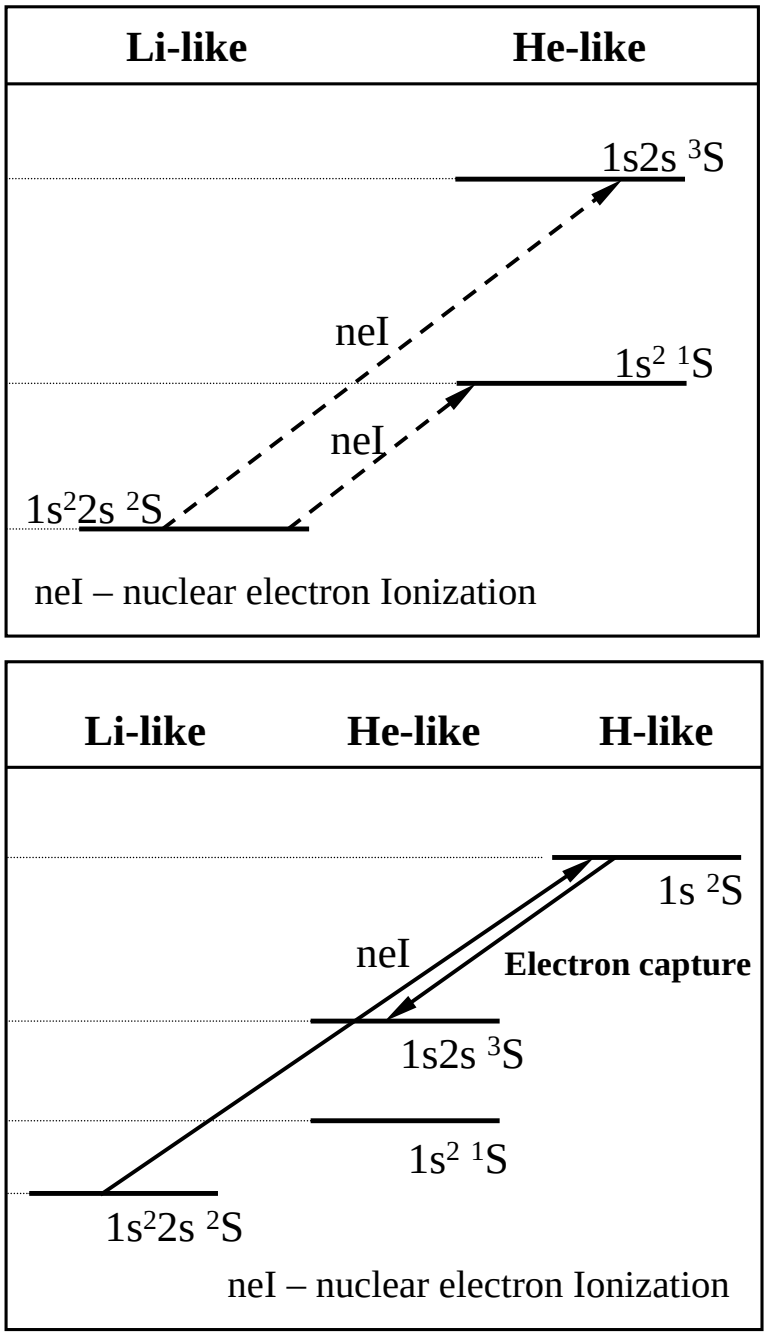


Figure 20: Two possible formation mechanisms of metastable $1s2s\,^3S$ state from the ground state of Li-like ions.

then the ratio of the metastable fraction produced in gas to the fraction produced in a foil will simply be the ratio of H-like charge state fractions in gases versus foils.

$$\frac{F_{gas}}{F_{foil}} \approx \frac{M_1}{N_1} \tag{44}$$

where $M_1$ and $N_1$ are H-like charge state fractions for $N_2$ gas and carbon foil, respectively. This equation has been tested for He-like $B^{3+}$ beams. Metastable fractions in ion beams produced in carbon foils and $N_2$ gas were measured experimentally, and the empirical values of charge state fractions $M_1$ and $N_1$ that enter Eq. **??** were obtained from Ref. [**?**] The ratios from the left and the right hand sides of Eq. **??** were compared and plotted in Fig. **??** versus the metastable ion production energy. The graph reveals the apparent correlation between the predicted and experimental ratios, which suggests that the proposed mechanism is the dominant contribution to the production of the $1s2s\,^3S$ metastable state.

Considering the two–step process, proposed immediately above to be dominant in the formation of the $1s2s\,^3S$ state in collisions of fast ionic beams with foils, we can proceed with theoretical estimates of the metastable fraction in He-like ions. The comparison in Fig. **??** demonstrated that the formation of the metastable $1s2s\,^3S$ ions in collisions with both solid and gas targets is proportional to the production of K-shell vacancies in the primary beams. This result gives rise to a model illustrated in Fig. **??**, where the formation of the $1s2s\,^3S$ state from Li-like incident beams in the foil is shown. Upon entering the foil, primary beams will end up in various charge

states, as shown. According to the study mentioned above, only H-like ions with a 1s electron will substantially contribute to the formation of the $1s2s\,^3S$ state. Li-like ions initially ionized to the He-like charge state are known to be dominantly in the ground state [**?**]. As shown in Fig **??**, the emerging He-like ion beam will consist of two parts: (i) one part is $N_{22}$ , which is the fraction of Li-like ions initially ionized to the He-like charge state (these ions have a small fraction $F_2$ of the metastable $1s2s\,^3S$ state), (ii) the other part is $N_{12}$, which is formed from H-like ions in the foil that subsequently undergo an electron capture as they exit the foil (these ions have a fraction $F_1$ of the metastable $1s2s\,^3S$ state).

The metastable $1s2s\,^3S$ ion fraction F is defined as the ratio of metastable ions to the total number of He-like ions in the beam after passing through the foil and can be expressed as

$$F = \frac{N_{met}}{N_{met} + N_{ground}} = \frac{F_1 N_{21} + F_2 N_{22}}{N_{21} + N_{22}} \approx \frac{F_1 N_{21}}{N_2} \tag{45}$$

where $F_1$ and $F_2$ are the fractions of metastable $1s2s\,^3S$ ions in $N_{21}$ and $N_{22}$ beams, respectively. As it has been demonstrated above, $F_2$ does not exceed 1.5%, therefore, it has been neglected in the last step.

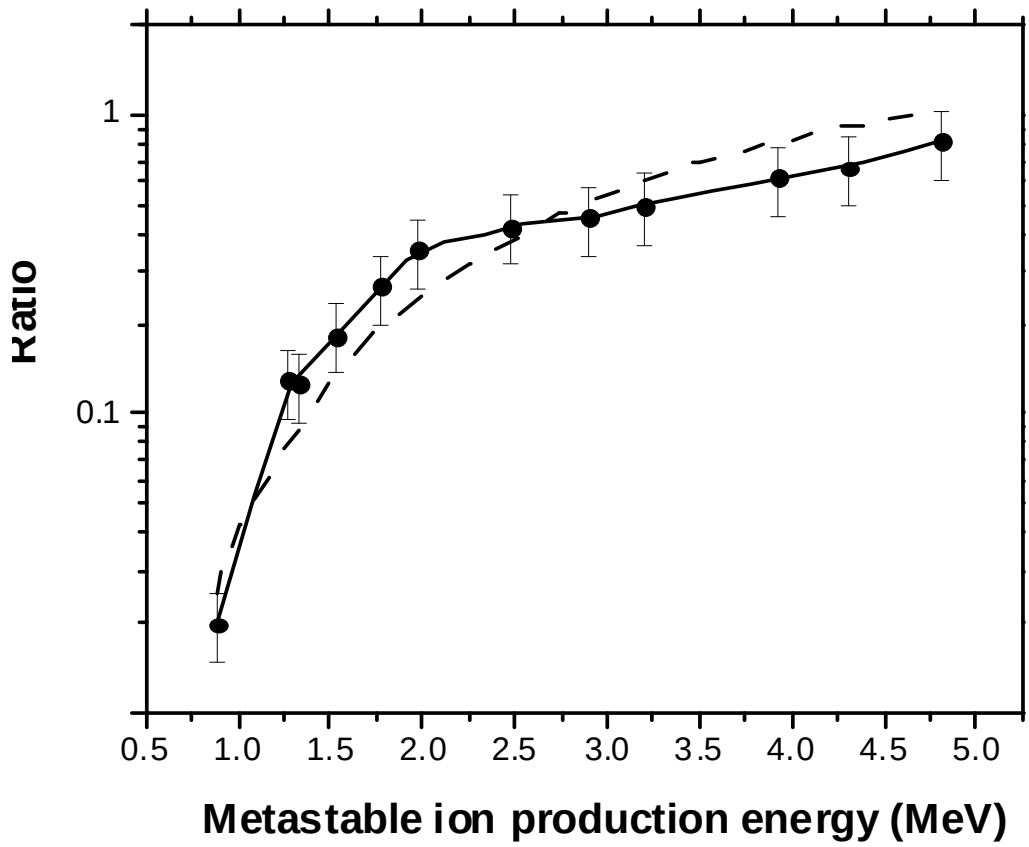


Figure 21: The comparison of predicted and observed ratios of the metastable fraction produced in $N_2$ gas to the metastable fraction produced in a foil. Circles - experimentally observed ratio of metastable fractions - $F_{gas}/F_{foil}$. Dashed line - the ratio predicted by the proposed model - $M_1/N_1$.

$N_2$ is the fraction of the He-like charge state in the emerging beam. The $N_{21}$ can be expressed as

$$N_{21} = \frac{N_1 N_2'}{N_1'} \tag{46}$$

where $N_1$ is the charge state fraction of H-like ions, $N_1'$, $N_2'$ are H- and He-like charge

state fractions, respectively, produced from a primary H-like beam. The metastable $1s2s\,^3S$ ion fraction can thus be expressed as

$$F = \frac{N_1 N_2'}{N_2 N_1'} F_1 \tag{47}$$

Since the capture of an electron to a $1s\,^2S$ ion will eventually result in both ground $1s^2\,^1S$ and the long-lived metastable $1s2s\,^{3,1}S$ states, the fraction $F_1$ is simply the ratio of electron capture cross section to the $1s2s\,^3S$ state to the the electron capture cross sections to the other states,

$$F_1 = \frac{\sigma(1s2s\,^3S)}{\sigma(1s^2\,^1S) + \sigma(1s2s\,^{3,1}S)} \tag{48}$$

In the next section, the model, described above, will be used for comparison with experimental results.

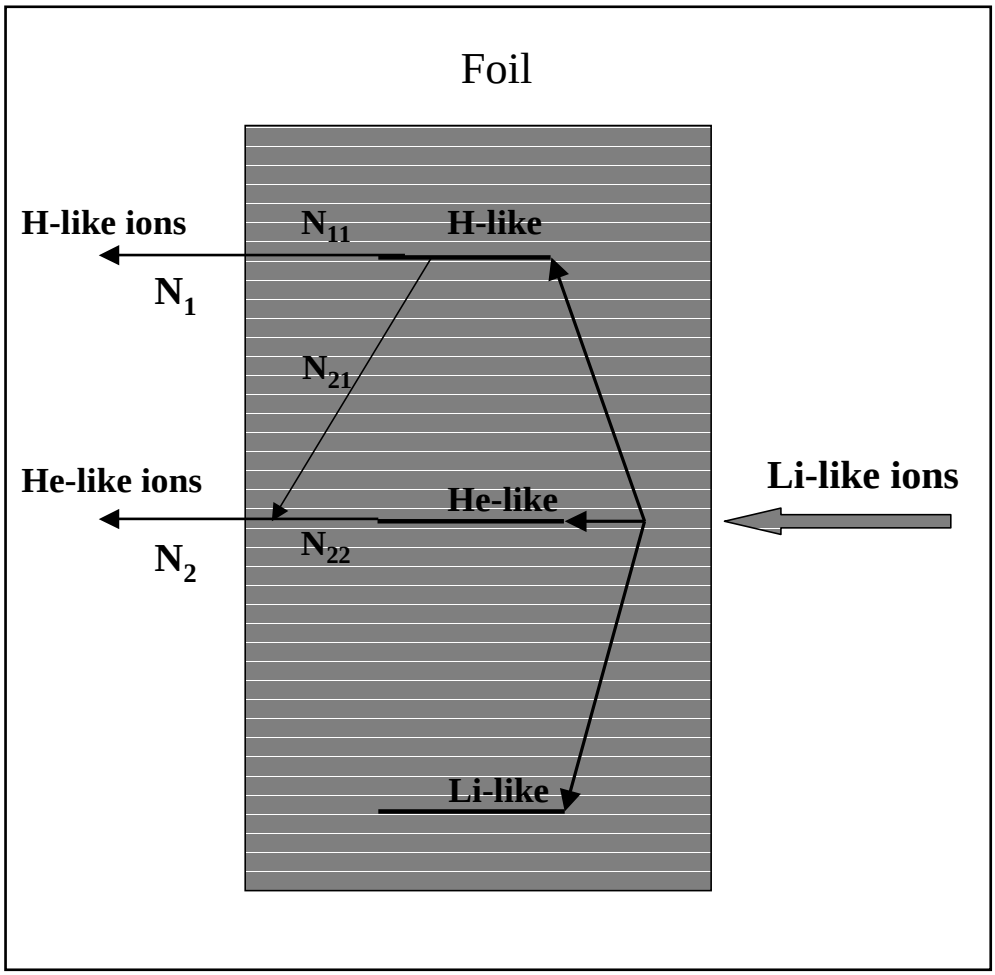


Figure 22: Production of metastable He-like ions in a foil from the incident Li-like beam.

In the next section, the model, described above, will be used for comparison with experimental results.

# 5 Metastable Fraction Determination: Experimental Results

## 5.1 Metastable Fraction in $B^{3+}$ Beams Produced in Foil and $N_2$ Gas Targets

The experimental technique used for the determination of the metastable fraction is described in the previous section. It is based on measurements of the electron emission from the doubly excited states of Li-like ions, formed in collisions of metastable He-like ions with gas targets ($H_2$, He). In order to increase the range of metastable ion production energies, desired beams were produced both inside of the tandem at the terminal using 5 $\mu g/cm^2$ carbon foils and after the tandem in 5 $\mu g/cm^2$ carbon foils. In the first case the metastable ion production energy differs from the final energy of the beam, at which the doubly excited states are formed, by a factor of q+1, where q is the ionic charge state. In the second case, both the metastable ion production energy and final beam energy are the same.

First, spectra obtained for $B^{3+}$ ions produced in $N_2$ gas at the terminal will be discussed. Since the positive ions are accelerated after stripping, the final energy of

$B^{3+}$ beams is greater than the production energy at the terminal by a factor of four. The left column in Fig. **??** shows two examples of Auger electron spectra obtained in the collision of 5.1 and 7.1 MeV $B^{3+}$ ions on $H_2$. The corresponding metastable ions were produced in an $N_2$ gas at the collision energies of 1.27 and 1.77 MeV, respectively. The Auger electrons at 157.0 eV and 166.5 eV, attributed to the 1s2s2p $^4P$ to $1s^2\,{}^1S$, and the $1s2p^2\,{}^2D$ to $1s^2\,{}^1S$ Auger decay, were observed. In Fig. **??**(a, left column), which shows the spectrum taken at the metastable production energy of 1.27 MeV, the intensity of the $^4P$ Auger line is significantly smaller than that of the $^2D$ line, even though the electron capture that contributes to the formation of the $^4P$ has a larger cross section than RTE at this beam energy. This fact can be interpreted in terms of a very small fraction of metastable $1s2s\,{}^3S$ ions in the incident beam, which is also supported by calculations using Eq. **??**, which gives a value of only 3%. In contrast, as presented below, the Auger spectrum measured with ion beams, produced in carbon foils at the same energy (see the right column of Fig. **??**(b)), has a much more intense $^4P$ line, resulting in a metastable fraction of 26%. Fig. **??**(b, left column) shows the Auger spectrum taken with ion beams, produced in $N_2$ gas at the higher energy. In this case, the intensity of the $^4P$ line has increased relative to the intensity of the $^2D$ line, indicating an increase in the metastable fraction. Measurements of the Auger yield were taken for a number of ion beam energies, and the fraction of metastable $1s2s\,{}^3S$ ions was calculated using Eq. **??**.

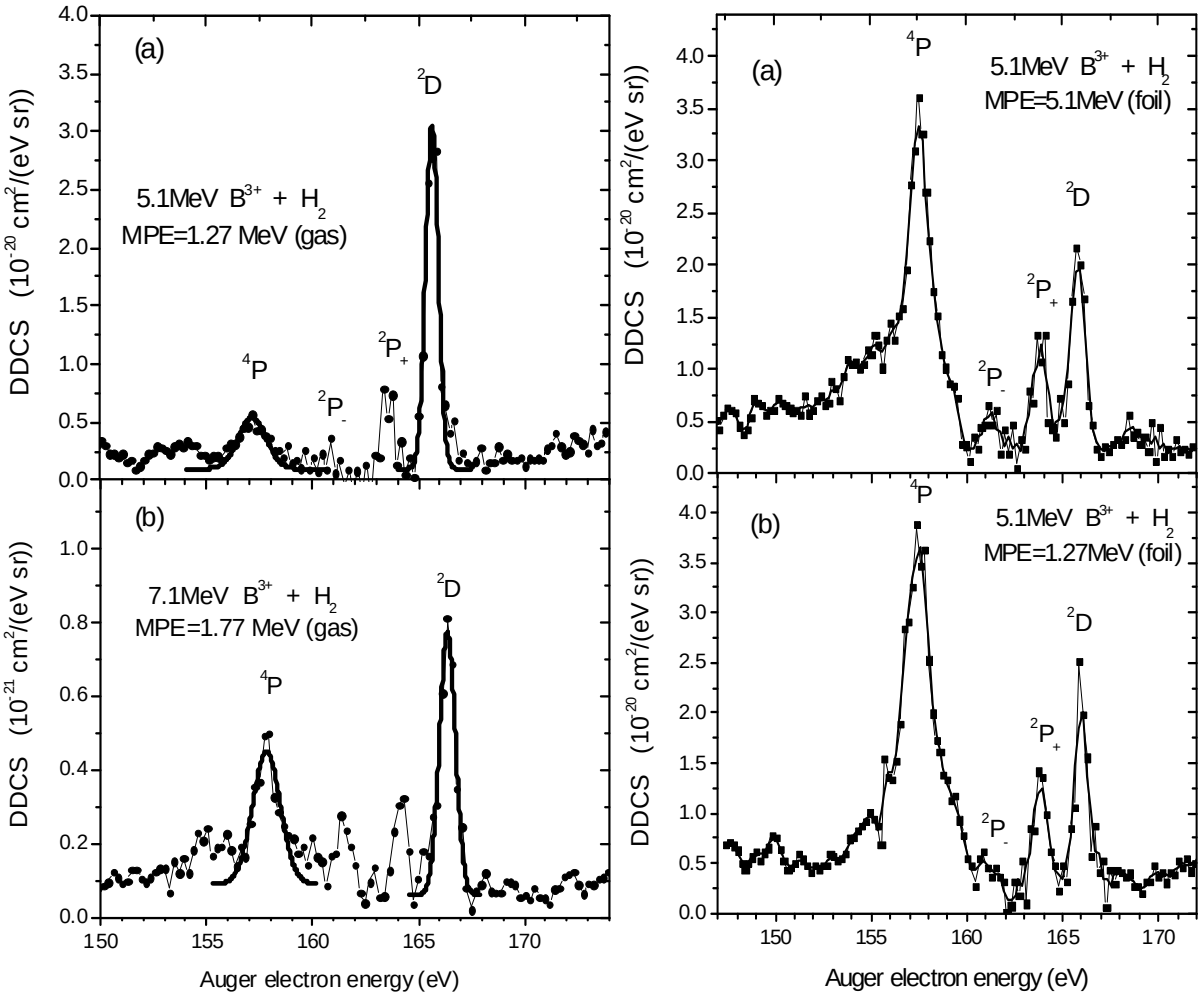


Figure 23: The left side of the figure shows zero degree Auger spectra measured for $B^{3+} + H_2$ collisions at the projectile energies of 5.1 and 7.1MeV. The $B^{3+}(1s^2\,{}^1S, 1s2s\,{}^3S)$ beam was obtained in collision of primary $B^{1-}$ with $N_2$ gas at the metastable production energies (MPE) of (a) 1.27 and (b) 1.77 MeV, respectively. The right side of the figure shows $B^{3+}(1s^2\,{}^1S, 1s2s\,{}^3S)$ beams produced in a carbon foil at two different metastable production energies (MPE) of (a) 5.1 and (b) 1.27 MeV, respectively.

The results are shown in by open circles in Fig. **??**. It is clearly seen that very few metastable ions are produced by stripping in gas if the production energy is lower than 1 MeV. These observations demonstrate that nearly pure ground state two-electron ion beams can be produced.

Also, it is evident from the figure that the metastable fraction increases with the increasing energy reaching the saturation when the $B^{1-}$ projectile velocity is near the H-like $B^{4+}$ 1s electron orbital velocity. This result is consistent with the theoretical model given in the previous chapter for the metastable ion production mechanism.

In carbon foils $B^{3+}$ beams were produced in two different ways: one by stripping the ion beam inside of the tandem at the terminal and the other by stripping the ion beam in a foil after the tandem. By using this method it was possible to produce $B^{3+}$ ions at two different metastable beam production energies with the same final beam energy, which gives the advantage of measuring the relative metastable fraction at two production energies independent of the electron capture or RTE cross sections. The right column of Fig. **??** shows two examples of Auger electron spectra obtained in the collision of 5.1 MeV $B^{3+}$ ions on $H_2$.

These spectra were obtained with two beams that were produced in different ways with stripping energies of 5.1 and 1.27 MeV, respectively. The ratio of intensities of $^4P$ to $^2D$ lines in the spectra does not change much from the lower to the higher energies; consequently, the metastable fractions are also approximately the same.

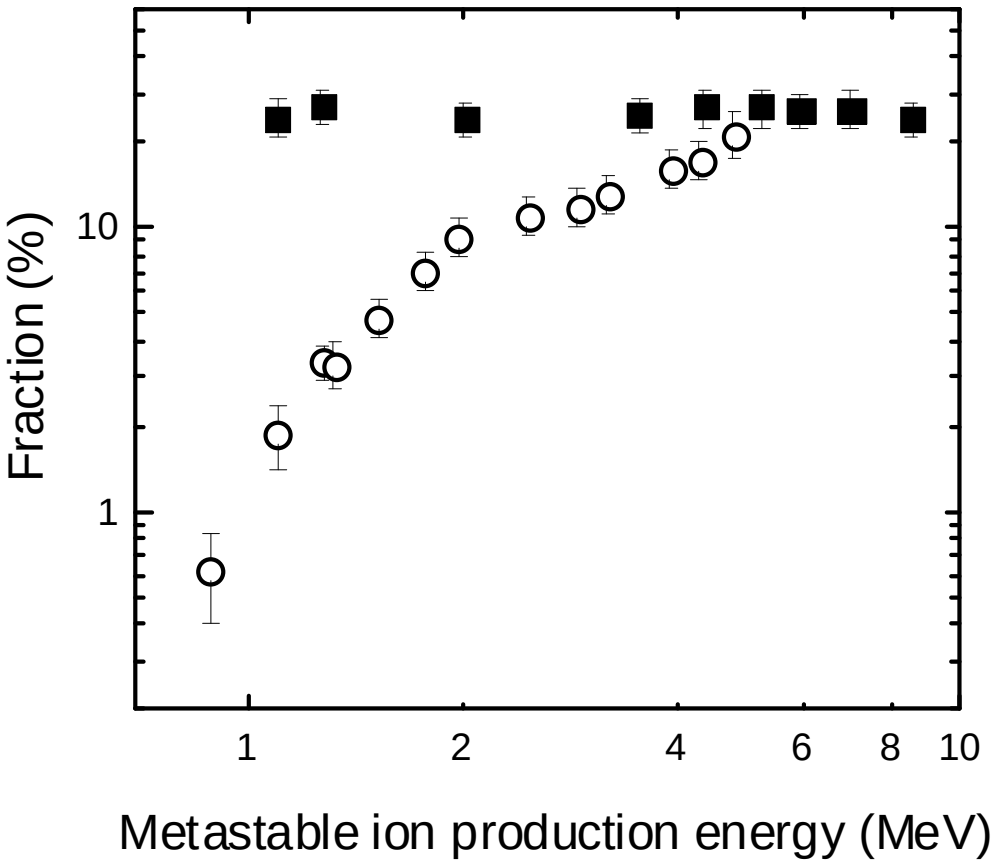


Figure 24: The metastable fraction F $=B^{3+}(1s2s\,^3S)/B^{3+}(1s^2\,^1S, 1s2s\,^3S)$ versus the stripping energy. Circles - the metastable fraction of the ionic beam produced in $N_2$ gas, squares - the metastable fraction of the ionic beam produced in carbon foils. The error bars correspond to the statistical uncertainty and are plotted at the 90% confidence level.

Further measurements over the metastable ion production energy range of 1-8.5 MeV have confirmed that the metastable fraction is the same for all production

energies and equals approximately 26%. These results are plotted as squares in Fig. **??** along with the metastable fraction resulting from the gas stripping.

The experimental data demonstrates a significant difference in the energy dependence of the metastable fraction between ion beams produced in foils and ion beams produced in $N_2$ gas (Fig. **??**). This result confirms predictions made in the previous chapter (see Fig. **??**) that the metastable fraction in He-like beams produced in a gas is an increasing function of the projectile energy.

## 5.2 Metastable Fraction in Fast He-like F, O, N Beams

First we would like to discuss measurements of the metastable fraction in He-like $F^{7+}$ beams. These ions were produced in 5 $\mu g/cm^2$ carbon foils both inside of the tandem at the terminal and in the poststripping foil after the tandem.

Figure **??** shows two examples of Auger electron spectra obtained in the collision of 25.3 $F^{7+}$ ions on $H_2$. Although final energies of these two beams are the same, the metastable ions were produced in two different ways as described above i.e., at 25.3 MeV (Fig. **??**(a)) and at 25.3/8 = 3.16 MeV (Fig. **??**(b)). In Fig. **??**(a) the ratio of the 1s2s2p $^4P$ to $1s2p^2\,^2D$ intensities exceeds that of in Fig. **??**(b). This indicates a greater content of metastable ions in $F^{7+}$ beams produced at 25.3 MeV. Further measurements at other production energies revealed that the metastable fraction increases with metastable ion production energy and reaches the maximum value of approximately 26% as shown in Figure **??**. Since the metastable fraction

in He-like ions is expected to maximize when the ratio of the projectile-foil relative velocity to the K shell velocity of $1s$ electron equals unity, the fraction is plotted in units of this ratio, $v_P/v_K$. The metastable fractions measured for $B^{3+}$ beams are shown in the same figure for comparison.

The metastable fraction measured for $O^{6+}$ ions, shown by solid triangles in Fig. **??**, attains the same maximum value of 26%, when $v/v_K$ =1. However, the energy dependence of the metastable fraction is different from that of both $F^{7+}$ and $B^{3+}$ ions, which is particularly evident at low energies.

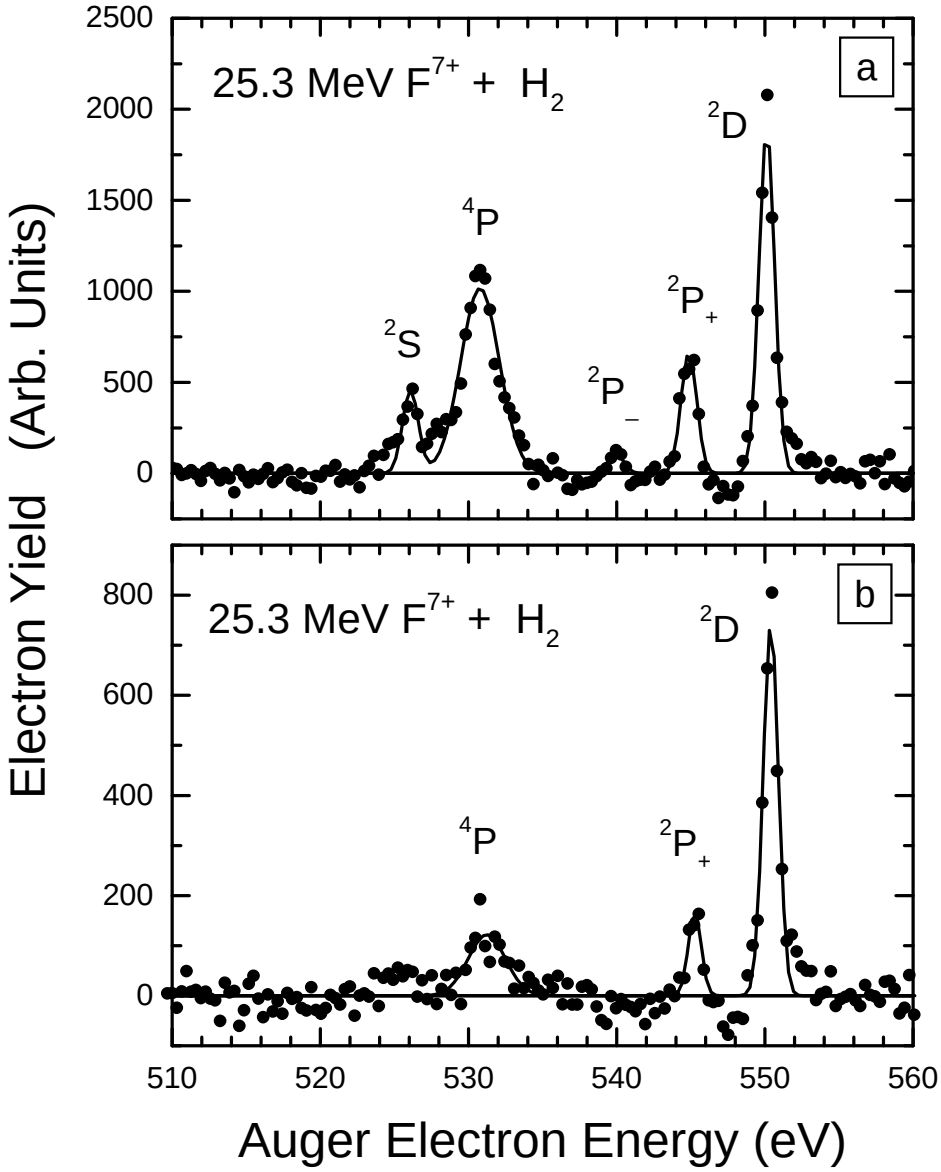


Figure 25: Zero-degree Auger spectra measured for 25.3 MeV $F^{7+}$ on $H_2$ collisions. $F^{7+}$ ($1s^2\ {}^1S$, $1s2s\ {}^3S$) beams were produced in carbon foils at two different metastable production energies of a) 25.3 MeV and b) 3.16 MeV, respectively.

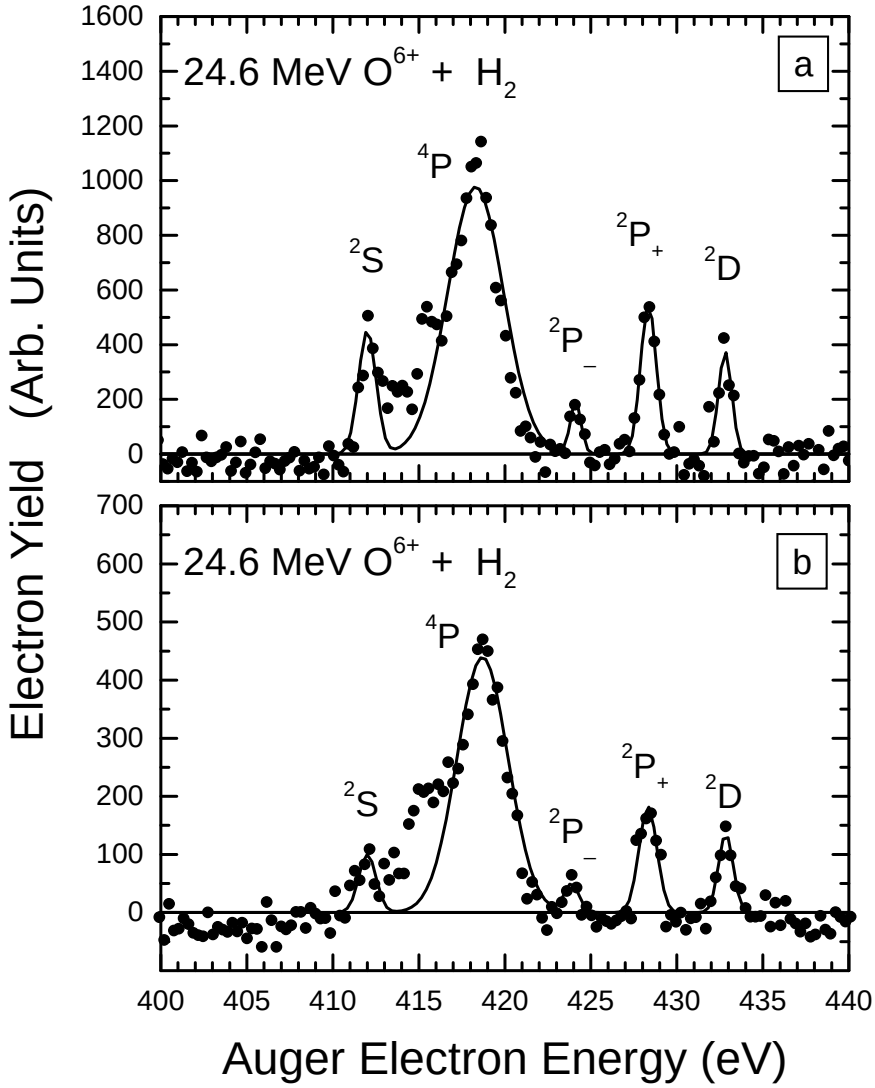


Figure 26: Zero degree Auger spectra measured for 24.6 MeV $O^{6+}$ on $H_2$ collisions. $O^{6+}$ ($1s^2\ {}^1S$, $1s2s\ {}^3S$) beams were produced in carbon foils at two different metastable production energies of a) 24.6 MeV and b) 3.5 MeV, respectively.

Two Auger electron spectra resulting from the collision of 24.6 MeV $O^{6+}$ on $H_2$

are shown in Figure **??**. Metastable ion production energies, in this case, were 24.6 MeV and 24.6/7 = 3.5 MeV, respectively. Since intensity ratios of 1s2s2p $^4P$ to $1s2p^2\,^2D$ peaks are approximately equal in both spectra, the two beams have about the same fractions of metastable $1s2s\,^3S$ ions. Additional measurements made at different beam energies revealed a constant metastable fraction of about 26% with a small dip around $v_P/v_K = 0.65$.

The presence of this dip is due to the competition between the two processes, involved in the production of the $1s2s\,^3S$ state: the production of ions incident on the foil and the single-electron capture to the $1s2s\,^3S$ state. The cross section for the first process increases as a function of the projectile velocity, whereas, the electron capture decreases with increasing projectile velocity. Thus, the resulting probability for the metastable ion production may have a minimum.

Only one measurement was taken for He-like $N^{5+}$ beams due to ion source limitations. The experimental data point has been measured for the projectile velocity, $v/v_K = 0.87$, which is close to the expected maximum of the metastable content. The metastable fraction was found to be 24% and is close to metastable fractions found for $B^{3+}$, $O^{6+}$ and $F^{7+}$ ions at the same beam velocity.

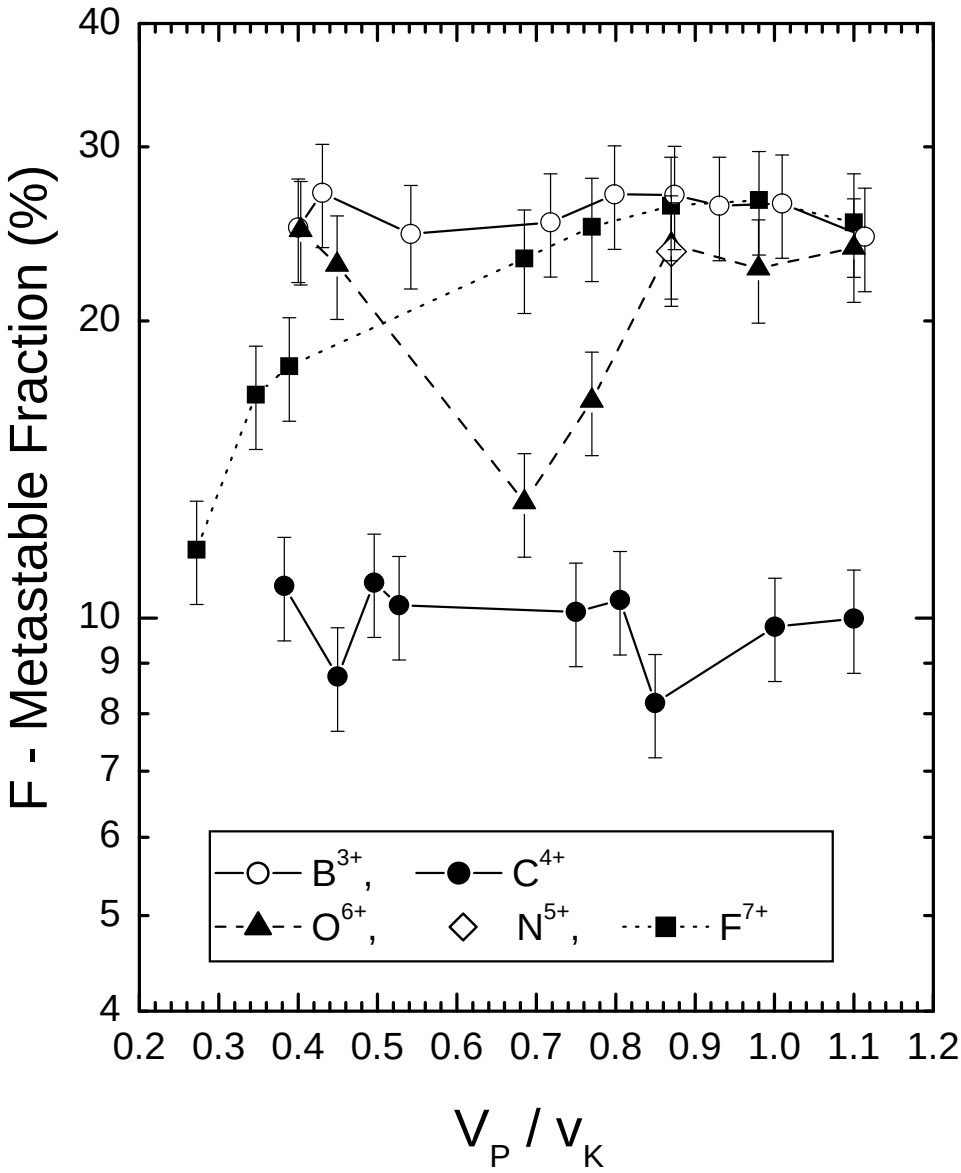


Figure 27: The metastable fraction F in He-like B, C, N, O, and F beams versus the projectile velocity in units of projectile K-shell electron velocity. The error bars correspond to the statistical uncertainty and are plotted at the 90% confidence level. Lines are drawn to guide the eye.

## 5.3 Metastable Fraction in $C^{4+}$ Beams: Influence of K-vacancy Sharing

Significant deviation from the metastable fraction of He-like ions discussed above has been observed for $C^{4+}$ beams where the fraction of metastable $1s2s\,^3S$ ions turned out to be relatively lower. Measurements show that $C^{4+}$ beams produced in a foil contain only 10% of the ions in the $1s2s\,^3S$ state (Fig. **??**) independent of the production energy within the investigated range. The observed difference between metastable fractions for $C^{4+}$ and other He-like ions can be understood if K-vacancy sharing between the projectile and the target is taken into account.

The K-vacancy transfer probability in near-symmetric collisions ( $C^{4+}$ on Carbon foil ) is known to be close to 1/2 [**?**]. In this case, the K vacancy in an incident metastable $C^{4+}$ ion will be transferred to the target atom, leaving approximately half of the projectile ions in the ground state, which is consistent with the observed metastable fraction. Since the K-vacancy transfer probability for other He-like beams is about one order of magnitude smaller than that for $C^{4+}$ ions, the reduction of corresponding metastable fractions is negligible.

## 5.4 Model Calculations for the Fraction of Metastable Ions

In order to test the accuracy of the model for the calculation of the metastable fraction, proposed in the previous chapter, all parameters entering Eq. **??**, $N_1, N_2, N_1', N_2'$,

and $F_1$ were evaluated experimentally. In this case, the discrepancy between the measured metastable fraction and the metastable fraction obtained using Eq. **??** can only arise due to the model itself or the statistical uncertainty. The latter is not expected to exceed 20%.

Charge fractions $N_1$ and $N_2$ were determined by means of the magnetic separation of the H- and He–like charge states, respectively for H–like beams incident on the thin Carbon foil, as shown in Fig. **??**(a). Similarly, charge fractions $N_1'$ and $N_2'$ were determined by the magnetic separation of the H- and He–like charge states, respectively for Li-like beams, as shown in Fig. **??**(b). All measurements were performed with $B^{3+}$ ions. The remaining parameter, $F_1$, is the fraction of He-like ions in the $1s2s\,^3S$ state, formed from H-like beams. $F_1$ has been determined experimentally by measuring the metastable fraction in $B^{3+}$ ions produced in collisions of $B^{4+}$ beams with carbon foils. Finally, the fraction of $1s2s\,^3S$ ions in the beam has been calculated using Eq. **??**. The model calculations were made for two different ion energies. The resulting values of metastable fractions are compared to the existing experimental data for $B^{3+}$ ions in Table **??**.

The discrepancy between the measured and calculated fractions is within the experimental uncertainty for measurements of the charge state fraction.

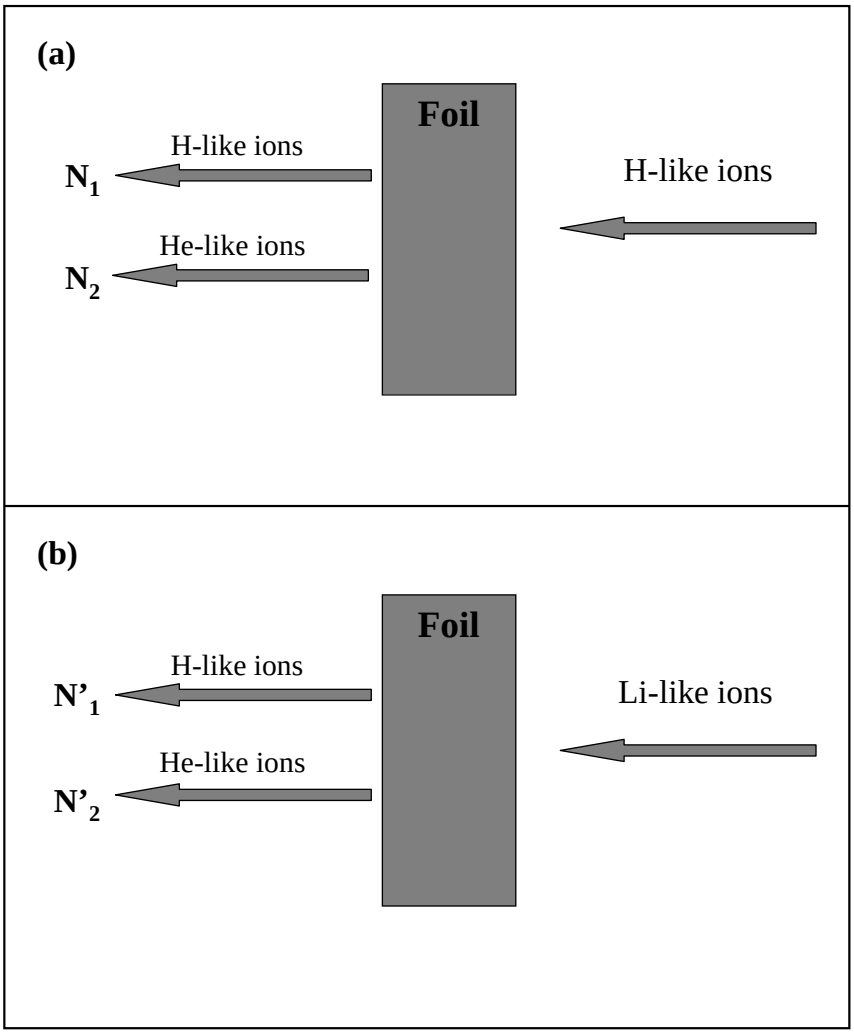


Figure 28: Techniques for measurement of charge state fractions $N_1, N_2, N_1', N_2'$

Table 5: Comparison of the calculated and measured metastable fractions for $B^{3+}$ beams.

| Metastable ion production energy (MeV) | Metastable fraction | |
|---|---|---|
| | Experiment | Model calculation |
| 3.5 | 26±6% | 33.8 |
| 5.1 | 26±6% | 23.4 |

## 5.5 Foil Thickness Considerations

The proposed model implies a certain correlation between the foil thickness and the fraction of metastable ions in emerging beams. Therefore several different foil thicknesses have been used in measuring the fraction of $1s2s\,^3S$ ions in 13.3 MeV $C^{4+}$ beams. Since the incident beam energy does not change in this test, the error arising from uncertainties in the RTE and electron capture cross sections is eliminated. The results are shown in Fig **??** along with the metastable fraction in ion beams produced in the $N_2$ gas. There is only a small difference in metastable ion fraction of beams produced in 2 and 5 $\mu g/cm^2$ foils. However, the fraction decreases when 1 $\mu g/cm^2$ foil is used and it's even lower in the case of the $N_2$ gas. This result is supported by the fact that according to the model the metastable fraction is proportional to the

production of H-like $C^{5+}$ ions, which, in turn, is reduced for thin foils or gases. In the later cases, charge equilibrium is not reached for the K–shell of the projectile. Finally, since the present study of the metastable fraction energy dependence was made using the beams produced in 5 $\mu g/cm^2$ foils, the results are not expected to vary with small changes in foil thickness.

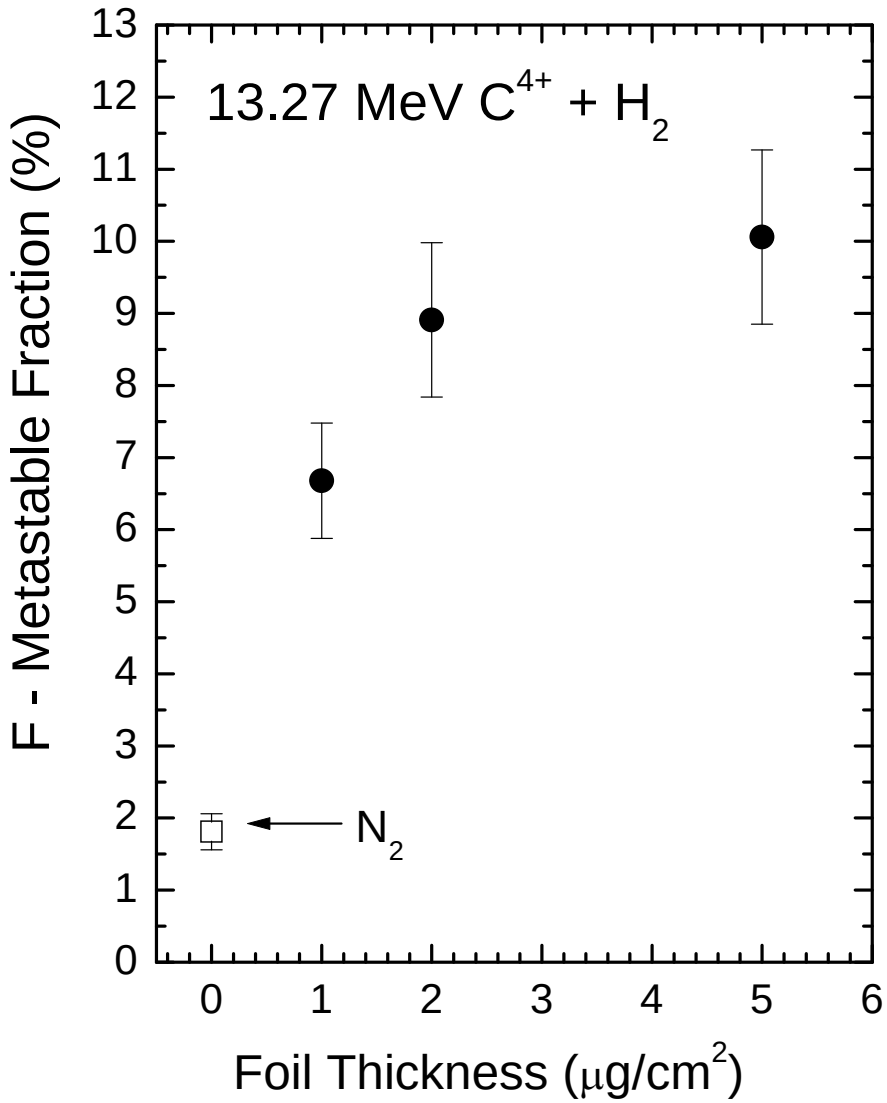


Figure 29: The metastable fraction F in 13.27 MeV $C^{4+}$ beams as a function of foil thickness. The error bars correspond to the statistical uncertainty and are plotted at the 90% confidence level.

# 6 Experimental Study of the Triply Excited $B^{2+}$ $(2s2p^2\,{}^2D)$ Resonance

## 6.1 Background and Motivation

The excitation and decay dynamics of triply excited states have become the subject of intense recent experimental and theoretical interest. Studies of ions with an empty K shell provide new information on the correlated motion of a pair of electrons in the field of a nucleus. A number of transitions to states with an empty K shell were observed for Li I and Be II using the foil excitation technique [**?**, **?**, **?**, **?**]. The first observation of the transition to the $2s2p^2\,{}^2D$ triply excited state from the $1s2s\,{}^3S$ state was done for B and F Li-like ions [**?**]. A new interest in the subject arose and many publications appeared in a short period of time with the advent of high brilliance light sources. Highly accurate measurements of the photoabsorption spectra have been made for transitions to a number of triply excited states in Li atoms [**?**, ?, ?, ?, ?, ?, ?]. The photoexcitation of ground state atoms or ions by a one photon process is, however, limited to ${}^2P^o$ final states due to the dipole selection rules. Consequently, triply excited states with other configurations have received less

attention and still pose experimental challenges. Absolute cross section measurements of the excitations to these hollow states, therefore, require different excitation techniques.

Simultaneous excitation of all three electrons from the ground state of Li-like ions directly into the $2s2p^2\,{}^2D$ state using either electron–electron or electron–photon interaction presents some experimental difficulties associated with small cross sections for the process. Alternatively, in ion–atom collisions, the excitation can be divided into two steps. First, one K shell vacancy can be produced in a primary Li-like beam after passing through a carbon foil. As a result, some of the emerging He-like ions will be in the excited metastable $1s2s\,{}^3S$ state, as discussed in the previous chapter. The fraction of ${}^3S$ ions in He-like beams, produced in the described way, is known. In the second step, the transition to the triply excited $2s2p^2\,{}^2D$ state is induced by colliding metastable ($1s2s\,{}^3S$) He-like beams with target gases. The use of initially pre-excited to the $1s2s\,{}^3S$ state ions makes it possible to isolate processes contributing to the formation of the $2s2p^2\,{}^2D$ state and thus, facilitates a critical comparison with recent theoretical results.

## 6.2 Experimental Details

He-like $B^{3+}$ beams were used for the investigation of triply excited resonances. Primary beams of boron ions in the 2+ Li-like charge state were produced in the accelerator terminal and then poststripped in a 5 $\mu g/cm^2$ carbon foil to achieve the

desired charge state of 3+. After passing the foil, $B^{3+}$ beams were focused into a 5 cm long differentially pumped gas cell, approximately 12 m downstream from the stripping region. In this arrangement 99.99% of the metastable $1s2s\,^3S$ ions (lifetime $\approx 100ms$) produced at 4 MeV will reach the target. The metastable population of the beam is independent of the production energy for this case (see Fig. **??**) and equals 26-27%.

The state of interest, $2s2p^2\,^2D$, is formed in collisions of metastable $1s2s\,^3S$ ions with hydrogen gas by Resonant Transfer Excitation (RTE). It is a two-electron process where a weakly bound target 1s electron is transferred to a 2p orbital of the projectile and simultaneously excites the 1s projectile electron to a 2p state. The single differential RTE cross sections can be evaluated within the Impulse Approximation (IA) [?], the process relating electron-ion cross sections to ion-atom scattering, also more recently referred to as the electron scattering model. The RTE cross section is given below

$$\frac{d\,\sigma_{RTEA}}{d\,\Omega} = \Omega_{RES}\,\frac{J(Q)}{V_p + Q}\,\frac{W(\theta)}{4\pi} \tag{49}$$

where J(Q) is a Compton profile of the target, $V_p$ is a projectile velocity, Q is the component of the target electron momentum in the direction of the beam, $\Omega_{RES^-}$ is the resonant excitation-scattering cross section calculated using the LS-coupling scheme [?], and $W(\theta)$ is the angular distribution factor, which, in case of the zero degree electron emission angle $\theta$ simply equals 2L+1 [**?**]. By matching the theoretical

RTE cross sections to the measured ones, the experimental determination of the autoionization rate that enters Eq. **??** as a factor is possible. In order to achieve experimental conditions close to the ones described by the Impulse Approximation, requiring that the projectile velocity should be much larger than the orbiting velocity of a target electron, $H_2$ molecules with slow loosely-bound electrons were chosen as a target. In this case, the uncertainty of measurements of the autoionization rate due to the possible error in IA is estimated to be less than 10% [?].

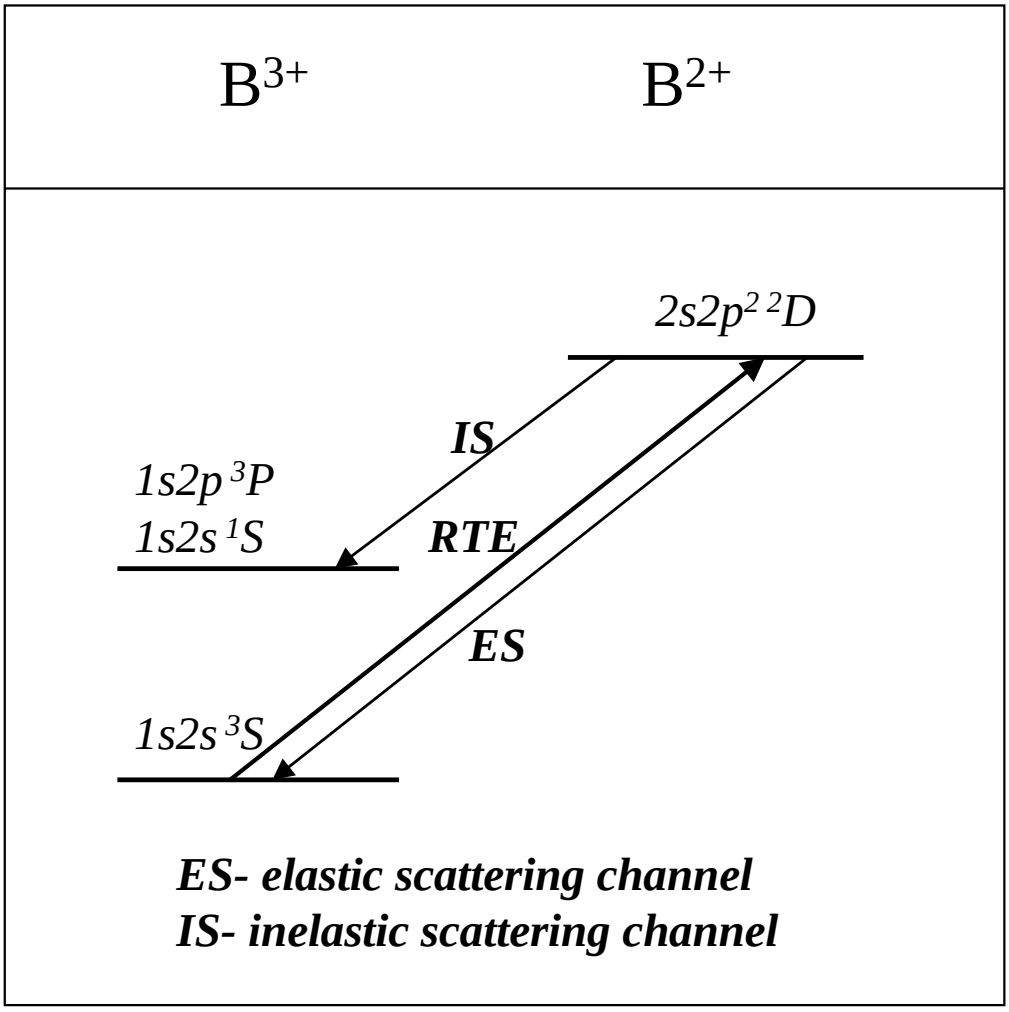


Figure 30: The formation and decay diagram of the triply excited resonance $2s2p^2\,{}^2D$, produced in collisions of the metastable $B^{3+}(1s2s\,{}^3S)$ ions with an $H_2$ target.

Since the radiative decay rate for the $2s2p^2\,{}^2D$ state is negligible [?], the resonance decays primarily by emitting Auger electrons to the $B^{3+}(1s2s\,{}^3S)$, the elastic scattering channel and to the $B^{3+}(1s2s\,{}^1S)$ and $B^{3+}(1s2p\,{}^3P\ )$, the two inelastic

scattering channels, as shown in Fig. **??**.

## 6.3 Results: Absolute Cross Sections and Decay Rates for the $B^{2+}$ ($2s2p^2\,{}^2D$) Resonance

Figure **??** shows an example of Auger electron spectra measured in collisions of 5.1 MeV $B^{3+}$ ions on $H^2$. The Auger electrons at 200.5 eV and 204.9 eV, emitted from the $2s2p^2\,{}^2D$ state were observed. Using the recent calculation of the Auger energies for various decay channels from the $2s2p^2\,{}^2D$ state [?] it was possible to identify the observed transitions. The more pronounced peak at 204.9 eV was attributed to the $1s2s\,{}^3S$ elastic Auger decay channel. The peak at 200.5 eV consists of the two unresolved $1s2p\,{}^3P$ and $1s2s\,{}^1S$ inelastic Auger decay channels. The separation in Auger energy between these two states is approximately 0.15 eV, which makes the task of measuring individual cross sections extremely difficult. However, their combined contribution is measurable and was used to estimate the branching ratio for the $1s2s\,{}^3S$ decay channel providing another test of theory. No evidence of Auger electrons corresponding to $1s2p\,{}^1P$ Auger decay was observed, which is consistent with the available theoretical predictions estimating that the contribution of this decay channel to the total autoionization rate is negligible for ions with $Z < 10$. Since the Auger decay channels for the $2s2p^2\,{}^2D$ state are limited to the ones described above, the unambiguous identification of the relaxation for this state has been made.

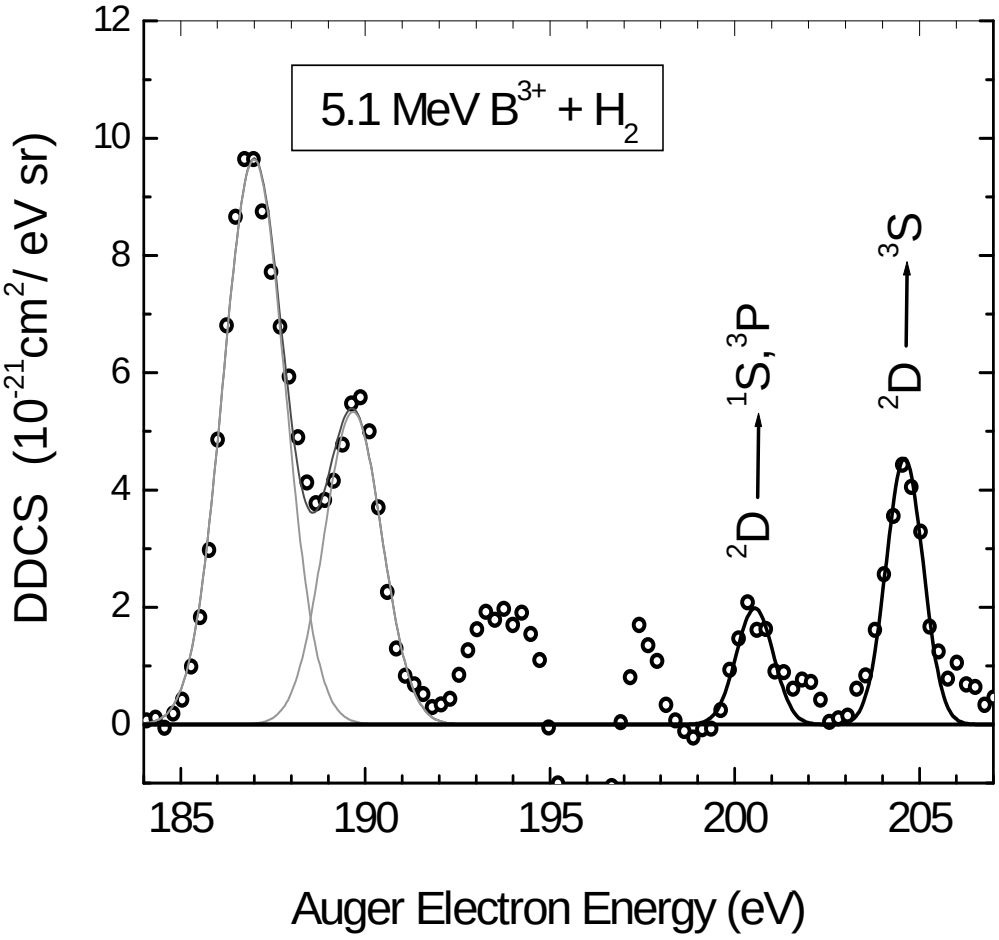


Figure 31: Zero degree Auger projectile electron spectra measured in 5.1 MeV $B^{3+}+H_2$ collisions are presented. Auger electron peaks at 200.5 eV and 204.9 eV are attributed to the $1s2p\,^3P, 1s2s\,^3S$ and to the $1s2s\,^3S$ Auger decay channels from the $2s2p^2\,^2D$ state, respectively. The solid lines are the Gaussian fits to the two Auger electron peaks.

The absolute differential cross sections for the $1s2s\,^3S$ to $2s2p^2\,^2D$ excitation followed by the more pronounced decay to the $1s2s\,^3S$ state were obtained from the

Auger spectra. The resonant behavior of the $1s2s\,^3S$ to $2s2p^2\,^2D$ transition has been confirmed by measuring the Auger yield at six collision energies in the range of 2-7 MeV. The fraction of $B^{3+}$ ions in the metasable $1s2s\,^3S$ state equaled approximately 26.5%. Figure **??** shows the resulting single differential cross section (SDC) versus the projectile energy. For comparison the zero degree RTE cross section calculated within the IA using the autoionization rate from Ref. [?] is given. Theory was found to best fit the experimentally observed Compton profile of the transition, if scaled by a factor of 0.61. In addition, the theoretical RTE cross section integrated over projectile energies has been compared to the integrated experimental SDC and found to match the latter if multiplied by a factor of 0.59, which is close to the factor obtained by fitting the theory to the experimental data, indicating that the contribution to the formation of the triply excited state is limited to RTE only and the theoretical description of the target Compton profile is correct. Nevertheless, the resulting difference between measured and predicted differential cross sections exceeds the absolute experimental error of 25% calculated by taking the quadrature sum of the statistical and absolute uncertainties.

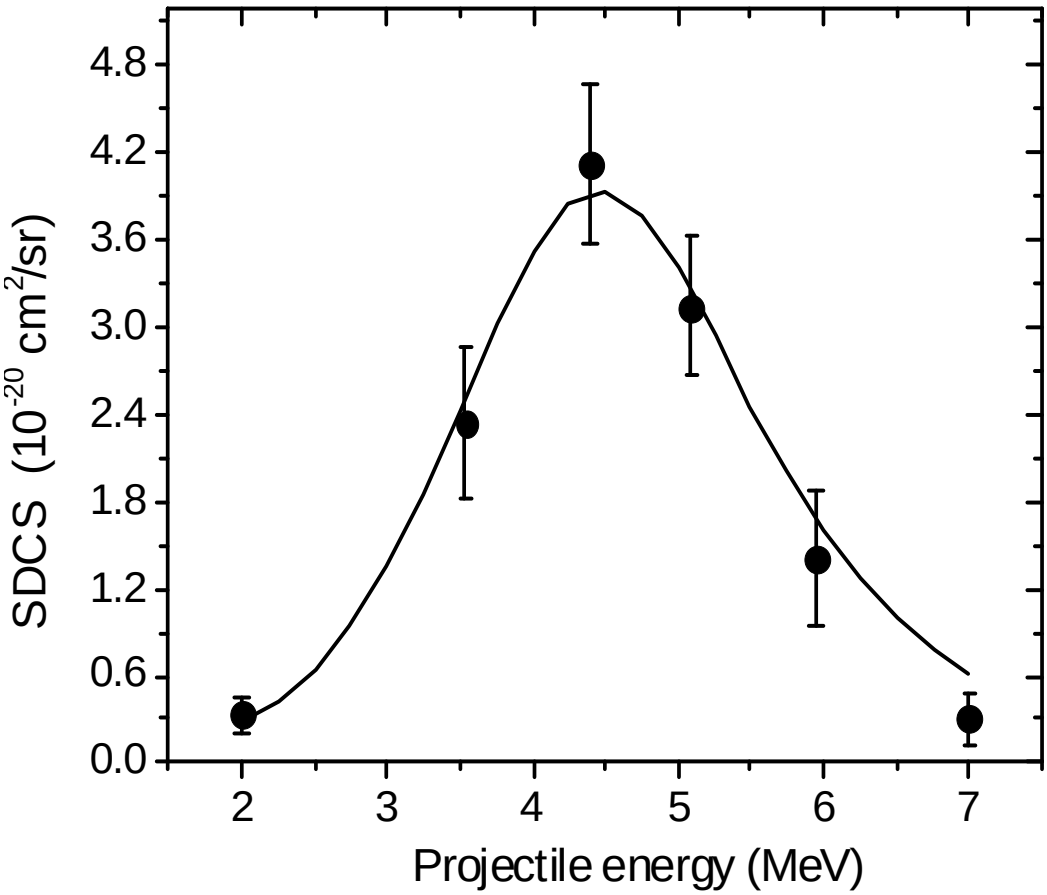


Figure 32: Measurements of single differential cross sections for the $1s2s\,^3S$ to $2s2p^2\,^2D$ excitation followed by the Auger decay to the $1s2s\,^3S$ state as a function of the projectile energy. The theoretical single differential cross section, calculated using the available autoionization rates [?], was multiplied by a factor of 0.61 to fit the experimental data. Error bars represent the statistical error.

Since the technique used for the calculation of RTE cross sections is known to be accurate for collisions of fast ions with hydrogen targets, the observed discrepancy

between theory and experiment is expected to arise mainly from the two theoretical parameters used in the calculation; the total autoionization rate and the relative Auger rate for the particular decay channel. Due to the negligibly small radiative decay probability for the $2s2p^2\,{}^2D$ state, the relative Auger rate for a particular channel is equal to the branching ratio for this channel and can be obtained directly from the experimental data. The branching ratio for the $1s2s\,{}^3S$ Auger decay branch is given as

$$B({}^3S) = \frac{Y({}^3S)}{Y({}^3S) + Y({}^1S) + Y({}^3P)} \tag{50}$$

where Y is the measured electron emission from the particular state. The resulting branching ratio is independent of the electron spectrometer constants, metastable population of the beam or the target pressure, and the formation mechanism of the $2s2p^2\,{}^2D$ state. Therefore, the absolute error for this measurement is limited to the statistical uncertainty of the experiment. Since the branching ratio, B(${}^3S$), is independent of the beam energy, the statistical uncertainty of the measurement can be minimized by using the experimental data taken at the resonant energy of 4.4 MeV. Finally, the branching ratio for the $1s2s\,{}^3S$ decay channel from the $2s2p^2\,{}^2D$ state was found to be $62 \pm 8\%$, where the absolute error is the statistical uncertainty of the measurement estimated at the 90% confidence level. The branching ratio obtained from the theoretical Auger rates [?] is 57%, which is in good agreement with our results presented in Table **??**.

We can now conclude that the difference between measured and predicted abso-

Table 6: Measured and calculated autoionization rates, branching ratios and widths for the triply excited $2s2p^2\,{}^2D$ state of $B^{2+}$.

| | Present data | Theory from Ref. [?] |
|---|---|---|
| Autoionization rate ($sec^{-1}$) | $34.8 \pm 8.5$ x $10^{13}$ | 57 x $10^{13}$ |
| Width (eV) | $0.23 \pm 0.6$ | 0.38 |
| Branching ratio ($1s2s\,{}^3S$) | $62 \pm 8\%$ | 57% |

lute cross sections arises from the remaining theoretical parameter used in calculation of the RTE cross sections, namely, the autoionization rate.

## 6.4 Concluding Remarks

The knowledge of the metastable fraction has been used in the experimental study of the triply excited $2s2p^2\,{}^2D$ resonance produced by resonant transfer excitation of the metastable $B^{3+}$ component of the beam. Measurements of the Auger electron emission at zero degrees were used to determine the absolute cross sections for the formation of the triply excited $2s2p^2\,{}^2D$ state and the branching ratios of the corresponding elastic and inelastic electron scattering channels. The results were

compared to existing theoretical calculations for the Auger decay rates.

It was demonstrated that the experimentally measured autoionization rate for the elastic decay channel from the $2s2p^2\,{}^2D$ state is significantly lower than the one calculated within the $1/Z$ expansion method, although the experimental branching ratio for this channel is in full agreement with the theory.

# 7 Triple Electron Capture in Fast Ion–Atom Collisions

## 7.1 Introduction

Multiple electron capture in collisions of highly charged ions with multielectron atoms or molecules has become a very active area of atomic physics research in the last decade. Transfer processes with more than two active electrons represent a fundamental problem of a many-body dynamic system, thus providing tests for most contemporary atomic models. The present understanding of multiple electron transfer has come from numerous experimental and theoretical studies primarily in terms of the classical quasimolecular description of the process. To date, however, a unified treatment that accounts for a wide range of energies, has not yet come forth. In particular, the role of electron-electron correlation effects in multielectron capture sill remains unclear, raising the demand for a more comprehensive model.

The investigation of multiple electron transfer processes has been stimulated by the introduction of more advanced ion sources during the 1980s, as attested by a number of experimental publications [?, ?, ?, ?, ?, ?, ?]. Projectile charge-change,

recoil-ion production and total charge-transfer [?, ?, ?, ?, **?**, **?**] cross sections were obtained for collisions of $Ar^{q+}$, $I^{q+}$ and $Xe^{q+}$ projectiles with various targets. Triple electron capture stabilization ratios were investigated by measuring the visible photon emission from Rydberg transitions [**?**]. The Auger electron spectroscopy was initially implemented in coincidence experiments with charge-state analyzed recoil ions [?, ?] and then subsequently employed in time-of-flight (TOF) triple-coincidence with scattered projectile and target ions to study collisions of $O^{7+}$ and $^{15}N^{7+}$ with Ar gas targets [?, ?]. The use of Auger electron spectroscopy in ion-beam and ion-beam–recoil-ion experiments made it possible to account for the projectile or excited target charge change caused by the Auger decay following the collision. Thus, light elements, for which Auger decay is dominant, were included in the multielectron capture studies.

Theoretically, the quantum-mechanical or even semiclassical treatment of collision systems with more than two active electrons is generally a difficult task since a large number of reaction channels are involved. In view of that, the simple classical overbarrier model [**?**] was extended [?, ?] to account for multielectron processes. Predictions of this model have been found to be in reasonable agreement with the experimental results. However, due to the fact that it ignores the electron-electron correlation and oversimplifies the electron transfer processes, the model could not give a precise description of multiple electron capture in slow collisions [**?**], whereas the breakdown of the first Bohn approximation at higher impact velocities (v > 1

a.u.) makes this representation inapplicable in the case of fast ion-atom collisions. An alternative treatment of multielectron transfer processes has been introduced by the independent electron model utilizing the uncorrelated Hartree-Fock approximation [**?**]. This study was focused on double electron capture in $He^{++} + He$ collisions at high impact velocities, allowing for the extension to systems with more than two electrons. Resulting in a overall favorable agreement with experiment, this work indicated the diminishing role of the electron correlation effects at increasing impact velocities.

Experimental investigation of multiple electron transfer resulting from fast, highly charged ion-atom collisions is hampered by the rapid fall off of capture probabilities with the increasing velocity of the ion. To the best of our knowledge, the study of true triple electron capture in fast (v > 1 a.u.) collisions has not yet been attempted experimentally. Meanwhile, the problem of multiple electron transfer at high impact velocities becomes more appealing, instigated by the dominant role of the process in populating lower-lying multiexcited states, recently a very dynamic area of atomic physics research. Additional incentives to investigate multielectron processes in fast collisions are provided by their importance in such diverse areas as high temperature plasma studies, astrophysics, and laser technology.

As previously mentioned, the extended classical overbarrier model (ECB) cannot be utilized for predictions in fast ion-atom collisions, due to the fact that the interaction time at higher projectile velocities is not long enough for target electrons

to be molecularized. In light of that, greater confidence is given to the independent particle model that includes the possibility of simultaneous capture of two or more electrons at similar internuclear distances by essentially unscreened projectile ion potential.

The excited states of light projectiles decay mainly by emitting Auger electrons, thus favoring the use of Auger electron spectroscopy. In addition, the very low probability of the multielectron capture at high velocities necessitates the use of highly efficient spectrographs in such measurements.

In this work, high resolution zero-degree Auger electron projectile spectroscopy has been used to study triple electron capture to doubly excited KLL states of carbon in collisions of fast (v = 4.5-6.6 a.u.) $C^{6+}$ ions with Ar gas targets. Absolute single differential cross sections (SDCS) have been obtained from the double differential cross section (DDCS) spectra and used to test the predictions of the independent particle model, in which the simultaneous capture of all three target electrons is assumed. Single electron capture probabilities, employed by the model, were calculated using the two-center semiclassical close-coupling method [**?**], based on an atomic orbital expansion. In order to allow a comparison of the measured zero-degree differential cross sections with calculated total cross sections, Auger electron emission from the doubly excited KLL states was assumed isotropic. Model calculations were found to be in a good agreement with the experimental data. The influence of the present study on the understanding of projectile screening and

electron-electron correlation effects in multiple electron capture is discussed.

## 7.2 Experimental Procedure

The experiments were performed in the J. R. Macdonald Laboratory at Kansas State University, using the 7 MV EN tandem Van de Graaff accelerator. The $C^{6+}$ beam was magnetically selected after colliding the primary Li-like $C^{3+}$ beam with a 5 $\mu g/cm^2$ carbon foil, and then focused into a 5 cm long differentially pumped gas cell. In collisions with Ar atoms, doubly excited KLL states of $C^{3+}$ ions were populated. These states decay dominantly by emitting Auger electrons at energies corresponding to the $1s^2\,{}^1S$ ground state transition.

The Ar gas target was maintained at constant pressure, utilizing a feedback-controlled baratron gauge. The target pressure was set at appropriate values to assure single collision conditions. Figure **??** shows the target pressure dependence of the Auger electron emission from the KLL states of the 13 MeV $C^{3+}$ ions. The number of detected electrons increases linearly with the target pressure in the range of 0–40 mTorr, while it decreases to zero when the gas flow is turned off. Consequently, the double collisions are still negligible up to Ar gas pressures of 40 mTorr.

A potential source of an experimental uncertainty is the possible beam contamination with $C^{5+}$ and $C^{4+}$ ions. In this case, the KLL states of $C^{3+}$ may be populated by single or double electron capture from the residual gas. In relation to that, the effect of the vacuum pressure on the KLL Auger electron emission was studied. The

bare $C^{6+}$ ions travel a distance of about 2 m after the analyzing magnet at a residual gas pressure of $1 \times 10^{-6}$ Torr before entering the gas cell.

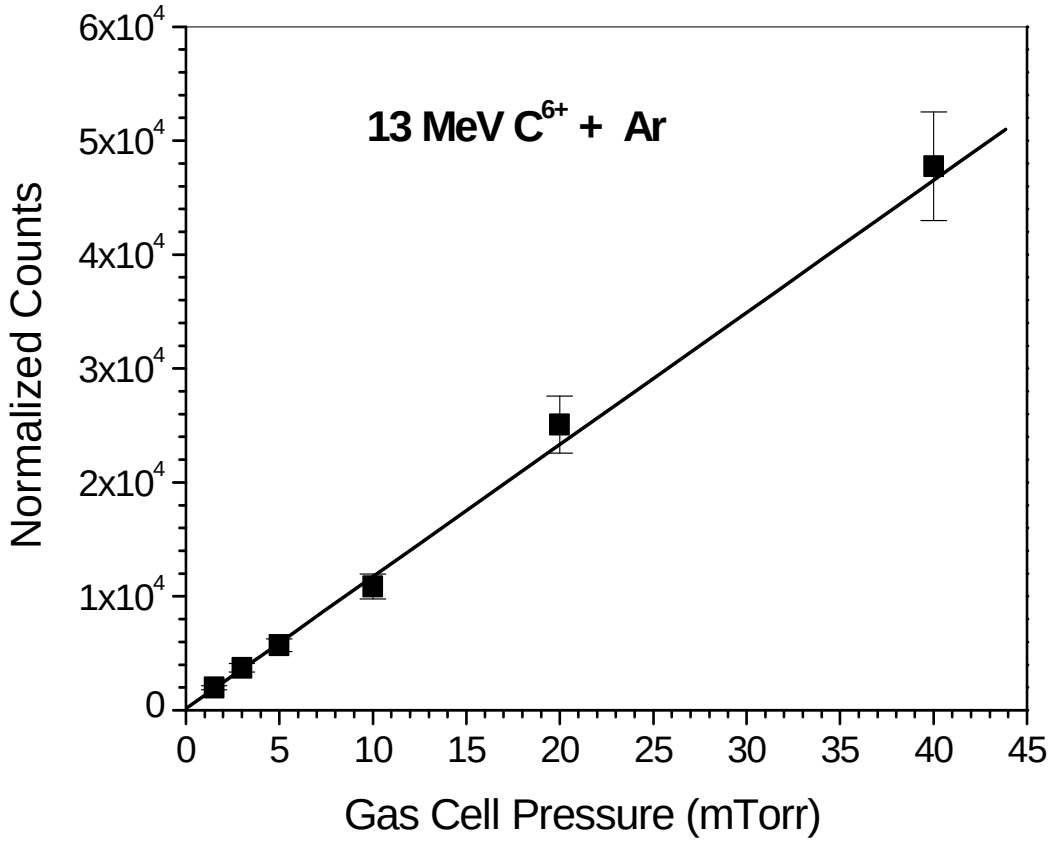


Figure 33: Target pressure dependence for the KLL Auger electron emission in 13 MeV $C^{6+} + Ar$ collisions. The solid line represents the linear fit to the experimental data.

To evaluate the contribution of a possible contamination, the vacuum pressure between the analyzing magnet and the gas cell was increased by a factor of 100, up to $1 \times 10^{-4}$ Torr, and the measurement of the Auger electron emission from KLL lines was repeated. Figure **??** shows two KLL spectra taken for the 13 MeV $C^{6+}$+ Ar collision system, normalized to the beam current. The open circles represent the

data taken with the lower vacuum pressure of $1 \times 10^{-6}$ Torr, and the solid circles represent the data taken with the higher vacuum pressure of $1 \times 10^{-4}$ Torr. There are five peaks formed by an Auger decay of doubly excited KLL states of $C^{3+}$ in the spectra. For both vacuum pressure settings the integrated KLL Auger electron emission is the same. Therefore, the formation of $C^{5+}$ or $C^{4+}$ ions between the analyzing magnet and the gas cell that contribute to the population of KLL states is negligible. Consequently, the above study clearly showed that the observed doubly excited states of $C^{3+}$ are formed in a single collision of $C^{6+}$ ions with Ar.

## 7.3 The Independent Particle Model

Since the independent particle model generally does not specify a certain treatment of the involved electrons, a brief description of its features, used in this study, is given. Screening dynamics of the incident projectile ion by captured target electrons play an important role in understanding multielectron processes in highly charged ion-atom collisions.

In the case of high impact velocities, if several electrons are transferred during the collision, the projectile's energy levels will not fully readjust to reflect the dynamics of the changes due to the insufficient interaction time. Therefore, the projectile charge will be only partly screened during the collision by captured electrons. In order for the interaction time to be considered small, the impact velocity has to exceed the projectile's orbital velocity of a state to which the target electron is

transferred. In the investigated system, 6-13 MeV $C^{6+}$+ Ar, impact velocities (4.5 - 6.6 a.u.) are greater than K (4.2 a.u.) and L ( 2.1 a.u.) shell velocities of the projectile.

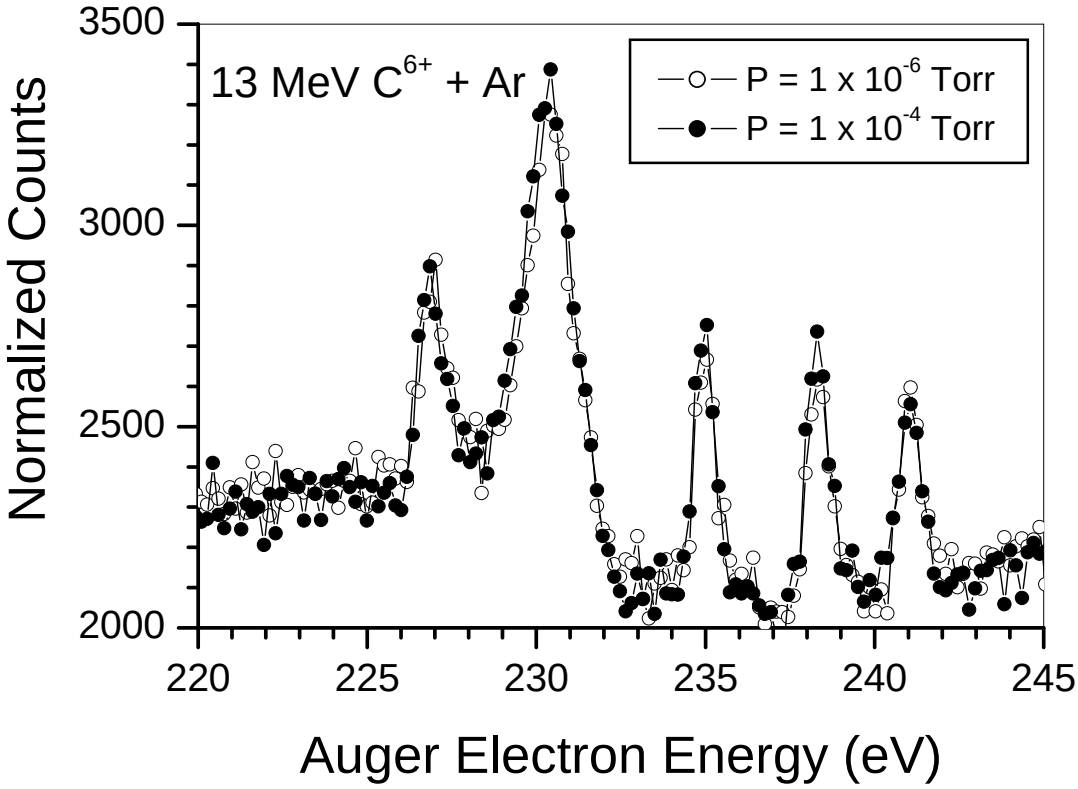


Figure 34: 13 MeV $C^{6+} + Ar$ Auger electron spectra measured with low and high vacuum pressure in the area between the analyzing magnet and the gas cell. Solid circles represent experimental data taken with a vacuum pressure of $1 \times 10^{-4}$ Torr, and open circles represent experimental data taken with a vacuum pressure of $1 \times 10^{-6}$ Torr.

As was mentioned above, the ECB model cannot be employed in this case since the collision time is not sufficient for target electrons to be molecularized. Instead, captured electrons rather should be treated as independent particles, captured by an unscreened potential. The total triple electron capture probability, P, is then a

statistical product of single electron capture probabilities. The detailed calculation of P from single electron capture probabilities is presented at the end of this section.

The two-center semiclassical close-coupling method, based on an atomic orbital expansion, has been used to calculate single electron transfer probabilities. The method is found to be quite successful in explaining the state selective electron transfer cross sections, at least for loosely–bound outer shell electrons. The motion of the projectile is approximated by a classical trajectory and the target electrons are treated quantum mechanically. For treating electron capture from the inner shells, an independent electron model is used, and the active electron is described by a model potential fitted so that the binding energies of the inner-shell electrons are reproduced. Although the possible role of outer shell electrons, (the so-called Pauli exchange effect), is not included explicitly in theory, it may be partially accounted for in using a model potential.

Since the triple electron capture process is expected to have a very low cross section at high collision energies, the collision system should be optimized to increase the electron transfer probabilities. This can be achieved by matching the electron orbital velocities of the target and the projectile. In Fig. **??** the energy level diagram for $C^{5+}$ and neutral Ar is shown. It is clearly seen that the binding energy for the Ar L shell is located between K and L shell energy levels of $C^{5+}$. Thus, the electron capture probability from the Ar L shell to the K and L shells of $C^{5+}$ is enhanced. At the same time, the contribution from K and M shells to the total

capture is significantly reduced, as can be seen from the work of Rødbro *et al* [**?**], where contributions from K, L and M shells of Ar into the total single electron capture cross sections are compared for fast proton on Ar collisions. In addition, the Nikolaev Oppenheimer-Brinkman-Kramers (OBK) approximation [**?**] was used in this study to evaluate the influence of capture probabilities from K, L and M shells of Ar numerically. The results were divided by a factor of 3, as it is well known that the Nikolaev OBK approximation overestimates the capture cross section by this factor [?]. It was shown that for the investigated collision energy range of 0.5-1.1 MeV/u, the K shell contributes less than 0.01%, and the M shell contributes about 0.5% into the total capture. Therefore, target electrons are mainly captured from the L shell and transfer probabilities from K and M shells of Ar are negligible.

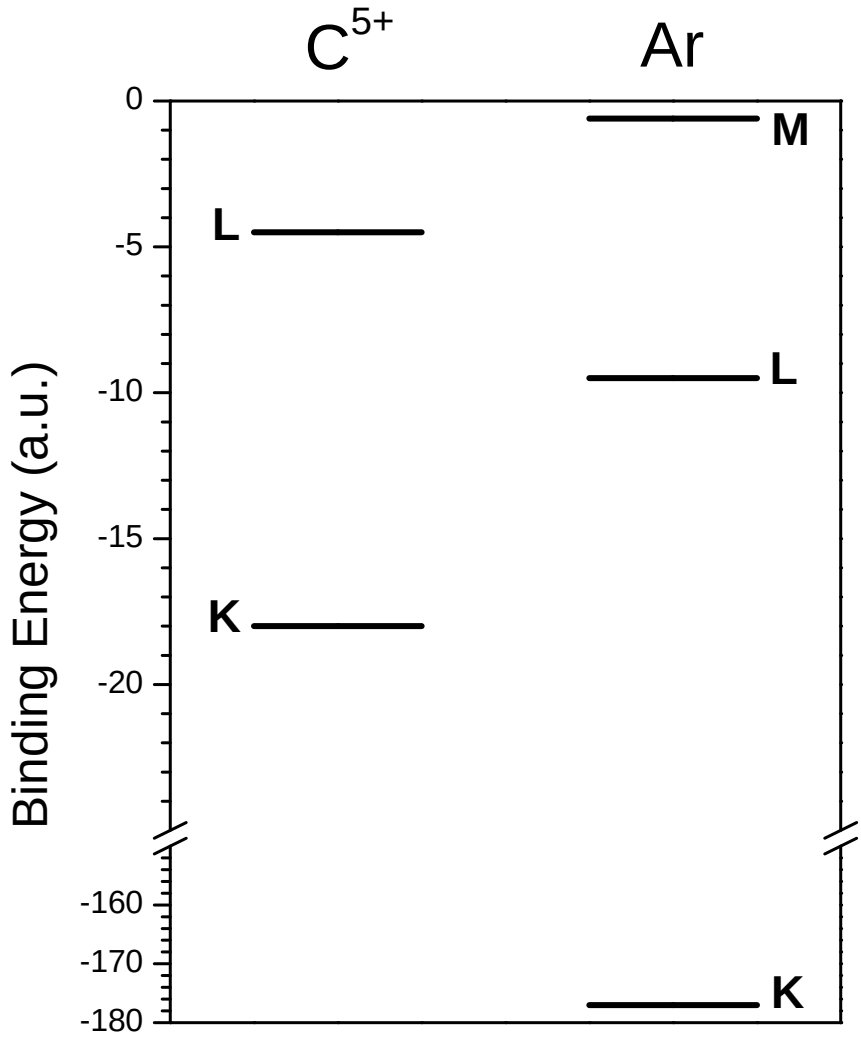


Figure 35: The energy level diagram for the $C^{6+}$ + Ar collision system. K and L shell binding energies of $C^{5+}$ match the L shell binding energy of Ar, which maximizes the electron transfer probability.

The L shell of Ar consists of three energetically resolved sublevels (nlm), recognized in the non-relativistic close coupling code as: 2s0, 2p0 and 2p±1, filled with 2, 2, and 4 electrons, respectively. Out of these 8 electrons, one is captured to the K shell (1s0) of $C^{6+}$, and two others are captured to the L shell (2s0, 2p0, 2p±1). If $C^j$ is the number of possible ways for any three electrons from the L shell of Ar in a certain electron configuration j to be captured to the KLL state in carbon, then the total triple electron capture probability can be expressed as

$$P(b) = \sum_j C^j \prod_{i=1}^{3} P_i^{kj}(b) \prod_{i=4}^{8} Q_i^j(b) \tag{51}$$

where j is the sum over possible statistical configurations. $P_i^{kj}$ is a probability for the $i^{th}$ electron of Ar in the j level (2s0, 2p0, 2p±1) to be transferred to the k level (K or L shells) of $C^{6+}$. $Q_i^j$ is a probability for the $i^{th}$ electron of Ar in the j level not to be transferred to either the K or L shell of $C^{6+}$.

## 7.4 Results and Discussion

Figure **??** shows the Auger electron spectrum measured in collisions of 13 MeV $C^{6+}$ ions with Ar gas targets. The formation of the $C^{3+}(1s2l2l')$ doubly excited states, namely $1s2s^2\,{}^2S$, $1s2s2p\,{}^4P$, $[1s(2s2p)^3P]\,{}^2P_-$, $[1s(2s2p)^1P]\,{}^2P_+$ and $1s2p^2\,{}^2P\,{}^2D$, which Auger decay to the $C^{4+}(1s^2)$ ground state, are prominent. All the above states were populated by triple capture, which allows for the population of all possible Li-like doubly excited states. Therefore the ${}^2S$, ${}^2P$ and ${}^4P$ states corresponding to the $1s2p^2$

configuration are also populated. However, the $^2P$ and $^4P$ states are not allowed to Auger decay to the $C^{4+}(1s^2)$ ground state due to parity conservation considerations, and the $^2S$ state has a very low Auger decay rate.

In order to determine the experimental SCDS for the population of the Li-like doubly excited states via triple capture, the area under the peaks was obtained after fitting the DDCS data with Gaussian distributions, as can be seen in Fig. **??**. The integrated area was then converted to SDCS after accounting for certain corrections, as discussed below.

First, in order to correct the experimental cross sections for the undetectable in this study x-ray decay channel, the Auger yields, $Y$, for the observed transitions were evaluated from theoretical autoionization and fluorescence rates [?, **?**, ?].

Also, the decay path of the metastable $1s2s2p\,^4P$ state was taken into account. It is a metastable state, with lifetimes of 25 ns for J=5/2, 9.1 ns for J=3/2 and 3.0 ns for J=1/2 [**?**,?], which are in general comparable to the ion's time of flight (TOF) in the gas cell (e.g., in the case of 13 MeV $C^{6+}$, TOF = 3.5 ns). However, due to the spectrograph geometry, electrons emitted in the area between the gas cell and the analyzer entrance still will be recorded, thus enhancing the electron yield of the state and also increasing the energy resolution of the line, as it is seen in Fig. **??**. The correct electron yield for the $1s2s2p\,^4P$ state was obtained after biasing the gas cell by a voltage of -30 V, which energetically separates the yield fractions originating from inside and outside the gas cell area.

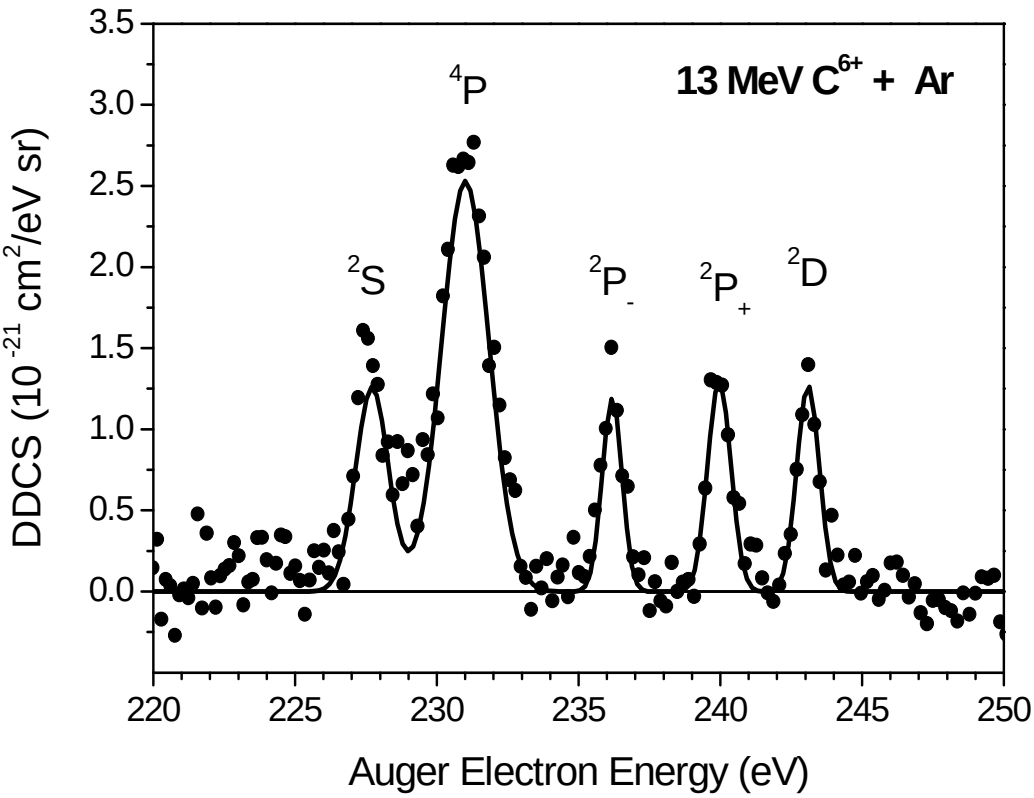


Figure 36: Absolute Auger electron DDCS spectra for the collision system of 13 MeV $C^{6+}$ + Ar, recorded at zero-degree with respect to the beam direction. The formation of the $C^{3+}(1s2l2l')$ $^2S$, $^4P$, $^2P_-$, $^2P_+$ and $^2D$ doubly excited states by triple electron capture, which Auger decay to the $C^{4+}(1s^2)$ ground state, is prominent. Note that the wider energy resolution of the $^4P$ peak is due to spectroscopic considerations (see discussion in section **??**). The solid line represents the Gaussian fit to the experimental data.

The total electron yield was then calculated from the available ion's time of flight and the exponential decay rate of the state [?]. The above corrections were included

in the same factor, $R$, for each collision energy. Finally, the four doubly excited states $^2D$, $^2P$, $^4P$ and $^2S$ corresponding to the same electron configuration, $1s2p^2$ , were populated by triple capture according to their statistical weight. However, since only the $^2D$ state is observed as discussed earlier, the production of other states was accounted for as shown by the inverse term in Eq. **??**.

Under the above considerations the single differential cross section for the triple electron capture to the KLL states of $C^{3+}$ is given by:

$$\begin{aligned}\left(\frac{d\sigma}{d\Omega}\right) &= \sum_i \left(\frac{d\sigma}{d\Omega}\right)^i \\ &= \sum_i Z^i_{exp} \frac{1}{Y^i_A} \frac{1}{R^i} \left[\frac{2J+1}{\sum_J (2J+1)}\right]^{-1} \end{aligned} \tag{52}$$

where $i$ is the sum over the observed KLL doubly excited states. In Table I, the discussed correction factors are presented for the 13 MeV $C^{6+}$ + Ar collision system.

The triple electron capture probability P(b) was obtained within the independent particle model as given by Eq. **??**. The total triple electron capture cross section, $\sigma$, was then determined after integrating the probability, $P(b)$, over the impact parameter, i.e.

$$\sigma = 2\pi \int_0^\infty P(b) b \, db. \tag{53}$$

In order to compare the independent particle model calculations with the exper-

imental zero degree SDCS, the total cross section $\sigma$ was differentiated with respect to the solid angle assuming an isotropic distribution for the KLL Auger electrons.

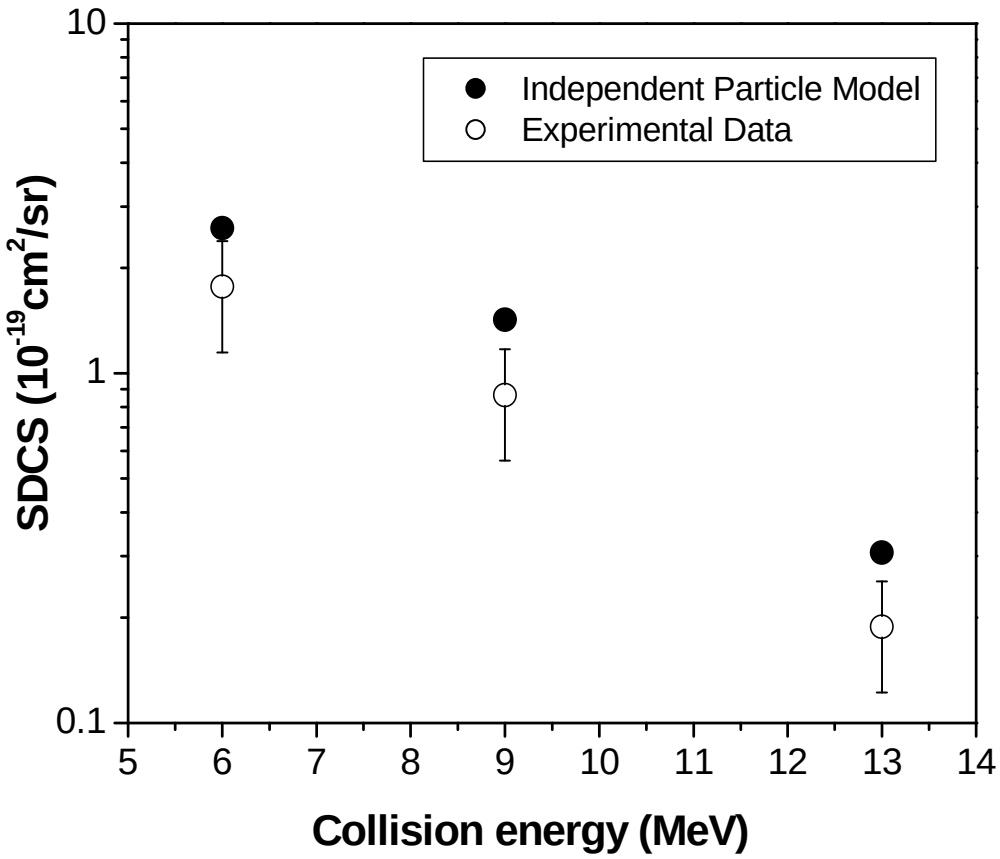


Figure 37: Absolute SDCS measurements of triple electron capture to the $C^{3+}$ KLL states, populated in fast collisions of bare carbon ions with Ar targets (open circles). Independent particle model calculations (solid circles) are seen to be in fairly good agreement with the data.

Thus, the calculated zero-degree SDCS for the triple electron capture to KLL states is finally expressed as

$$\frac{d\sigma(\theta = 0^\circ)}{d\Omega} = \frac{\sigma}{4\pi}. \tag{54}$$

In Fig. **??** the experimental zero degree triple electron capture cross sections to KLL states measured for 6, 9 and 13 MeV $C^{6+}$ + Ar collisions are compared with the independent particle model calculations for the corresponding collision energies. The experimental error bars are calculated by taking the quadrature sum of the statistical and absolute uncertainties. The latter incorporates mainly the electron detection efficiency of the spectrograph.

It is seen clearly from Fig. **??** that the independent particle model calculations systematically overestimate the experimental triple capture SDCS by a factor of about 1.5. The predicted collision energy dependence of the process is in good agreement with the experimental one. Considering the fact that theoretical single electron capture amplitudes contain certain errors not shown in Fig. **??**, the comparison gives enough evidence to conclude that the independent particle model provides an adequate description of the triple electron capture in fast ion-atom collisions, therefore validating physical ideas incorporated in the model. Specifically, the screening dynamics of the incident projectile ion by captured target electrons can be understood through simultaneous electron transfer, in which the energy levels of the projectile do not completely readjust during the course of the collision due to the insufficient interaction time. Therefore, if the impact velocity exceeds the projectile electron orbital velocities, the ion nucleus remains essentially unscreened during the collision. In addition, since the independent particle model does not account for the electron-electron correlation explicitly, the role of the electron-electron correlation

in triple electron capture by fast ions is believed to be not as significant as in slow collisions [?].

## 7.5 Conclusions

Zero-degree Auger electron spectroscopy has been used to determine the absolute single differential cross sections for triple electron capture to doubly excited KLL states of Carbon in collisions of fast (v = 4.5-6.6 a.u.) $C^{6+}$ ions with Ar atoms. Experimental data were used to test the predictions of the independent particle model that utilizes single electron capture probabilities calculated using the two-center semiclassical close-coupling method, based on an atomic orbital expansion. Single differential cross sections were obtained from the total cross section calculations after assuming an isotropic Auger emission. Model calculations were found to be in fairly good agreement with the experiment, signifying that the independent particle model provides an adequate description of the triple electron capture in fast ion-atom collisions. In particular, it was concluded that target electrons are captured simultaneously by an essentially unscreened potential of the projectile, reflecting the fact that the collision time is not sufficient for ion energy levels to readjust. Finally, present results support the fact that electron-electron correlation effects do not appear to be significant in multiple electron transfer at high collision velocities.

Table 7: Correction factors for the extraction of the experimental SDCS for the triple electron capture to the $C^{3+}$ KLL states, from the corresponding DDCS spectra. SDCS calculated within the independent particle model are also given. $Y$ is the Auger yield, and $R$ is the fraction of ions in the metastable $1s2s2p\,^4P$ state that decays after the analyzer entrance. Transition energies are given relative to the $C^{4+}(1s^2)$ ground state in units of eV. Both experimental and calculated SDCS are in units of $10^{-21} cm^2/sr$. All data are referred to the case of the 13 MeV $C^{6+}$ + Ar collision system.

| KLL State | Auger Energy | Integrated Peak Area | $Y$ | $R$ | Stat. Weight | $DCS_{exp}$ | $DCS_{th}$ |
|---|---|---|---|---|---|---|---|
| $1s2s^2\,^2S$ | 227.5[1] | 1.8±0.6 | ≃1[2] | 1.00 | 1 | 1.8±0.6 | |
| $1s2s2p\,^4P$ | 229.7[1] | 5.3±1.6 | ≃1[3] | 0.51 | 1 | 10.5±3.2 | |
| $1s2s2p\,^2P_-$ | 235.9[1] | 1.1±0.5 | 0.92[4] | 1.00 | 1 | 1.1±0.3 | |
| $1s2s2p\,^2P_+$ | 239.3[1] | 1.3±0.4 | ≃1[4] | 1.00 | 1 | 1.3±0.4 | |
| $1s2p^2\,^2D$ | 242.3[1] | 1.3±0.4 | ≃1[2] | 1.00 | 3 | 3.8±1.1 | |
| | | | | | SDCS(sum) | 18.6±0.6 | 30.6 |

# 8 Experimental Observation and Theoretical Calculations of Triply Excited $2s2p^2\ {}^2S^e$, ${}^{2,4}P^e$, ${}^2D^e$, and $2p^3\ {}^2P^o$, ${}^2D^o$ States of Fluorine

## 8.1 Background and Motivation

The study of triply excited states of atoms and ions presents new opportunities to probe multi-particle excitations of a quantum system, thus providing tests for the most advanced atomic theories. For these states, interelectronic correlation plays a crucial role in determining their properties. As a result, theoretical descriptions based on the conventional independent particle model fail completely. Triply excited states, in general, are difficult to produce from the ground state by single photon absorption or by electron impact excitation, since both processes rely on the weak electron-electron interaction to promote more than one electron in a single collision. Thus, only with the advent of intense light sources in the last decade have experimental studies of triply excited states in Li atoms been initiated. A number of these states have been investigated using photoion and photoelectron spectroscopy [?, ?, ?, ?, ?, ?]. These experiments have stimulated an avalanche of

theoretical calculations [**?**, **?**, ?, **?**, **?**] that, in general, described fairly well specific experimental results.

While the use of synchrotron radiation for such studies has yielded considerable information on triply excited states of Li atoms, the insufficient densities of ionic targets ruled out the possibility to investigate triply excited resonances in Li-like ions. Furthermore, the limited nature of the photoexcitation technique prohibited the population of quartet states. The absence of available experimental data for three electron ions has prevented theorists from pursuing a global understanding of triply excited states, such as new classification schemes, approximate quantum numbers, and possible approximate selection rules for the formation and the decay of these states.

In this work a new experimental method, relying on the strong electron-projectile Coulomb interaction, to efficiently form triply excited states of ions and atoms, has been developed. The states are produced via triple electron capture in energetic ion-atom collisions. By the proper selection of collision partners, any triply excited state of any ion can, in principle, be populated. The technique is demonstrated by studying the 2l2l′2$l''$ intrashell states of fluorine and experimental measurements are compared to theoretical calculations based on the hyperspherical close coupling method (HSCC). In particular, all $2s2p^2$ and $2p^3$ triply excited states of $F^{6+}$ ions are populated in collisions of bare 16 MeV $F^{9+}$ ions with Ar and Kr targets. Multiple transitions from these states into the continua of $F^{7+}$ are identified from the ejected

electron spectra in the direction of the ion beam and used to determine transition energies, branching ratios and absolute differential cross sections for the observed states. The experimental branching ratios are compared to available theoretical calculations.

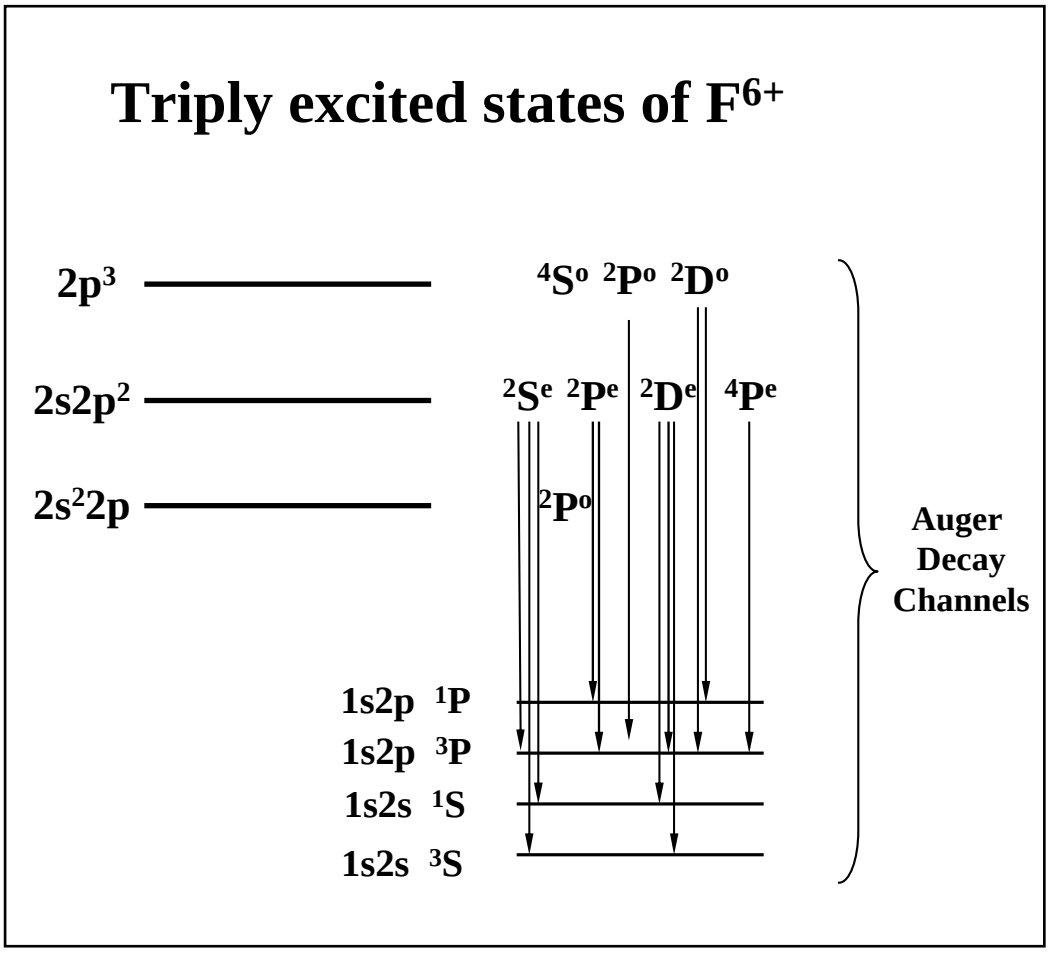


Figure 38: Possible Auger relaxation pathways from the triply excited states of Li-like fluorine into the continua of $F^{7+}$ ions.

Triply excited states have been previously observed in energetic ion-atom colli-

sions [?], however, since the states were formed via the excitation process, only a very few of them have been identified. Multiply excited states were also formed in low-energy ion-atom and ion-surface collisions, but the resolution in these experiments was not sufficient for the identification of individual states [**?**]. Recently, triply excited states of ions have been produced by resonant transfer and excitation (RTE) using metastable ion beams [**?**], as discussed in Chapter 6. Although, the technique has been successfully applied to measurements of autoionization rates and branching ratios in Li-like ions, the selectivity of the RTE process leads to the population of mainly $2s2p^2\,{}^2D^e$ states. The triple electron capture is a more robust method. In the present work only the $2l2l'2l''$ intrashell triply excited states are investigated, but the technique can be extended to the production of other hollow states by utilizing appropriate ion-atom collision systems.

## 8.2 Experiment

The present measurements were carried out in the J. R. Macdonald Laboratory at Kansas State University, using the 7 MV EN tandem Van de Graaff accelerator. Magnetically selected $F^{9+}$ beams were focused into a 5 cm long differentially pumped gas cell. The Auger electrons, resulting from the collision with argon, were emitted at energies corresponding to transitions of triply excited states to 1s2l final states of $F^{7+}$. Double differential cross sections (DDCS) were measured with a total uncertainty of 30%, calculated by taking the quadrature sum of the statistical

(20%) and absolute (25%) uncertainties. The latter incorporates mainly the electron detection efficiency of the spectrograph. Two potential sources of experimental uncertainties are represented by the possible contamination of $F^{9+}$ beams with other charge states and the double collisions in the gas cell. The single collision regime was established by setting the Ar target pressure at 20 mTorr, according to the study presented in Chapter 7. The analysis of the triple electron capture from Ar, in the previous Chapter, also shows that the formation of $F^{8+}$ or $F^{7+}$ contamination beams, which could contribute to the electron emission from populated states, is negligible. Consequently, it was demonstrated that the observed triply excited states of $F^{6+}$ are formed in a single collision of $F^{9+}$ ions with Ar.

In order to maximize the population of $2l2l'2l''$ triply excited states in $F^{9+}$ projectile ions, an appropriate atomic gas has to be chosen as a target. The probability for a target electron to be captured to the L shell of $F^{8+}$ is proportional to the overlap of electron momentum distributions (Compton profiles) in the initial and final states of the transferred electron. Figure **??** shows these Compton profiles for electrons both in K and L shells of fluorine (middle panel) and in L and M shells of Ar (bottom panel), chosen as a target atom. The top panel in Fig. **??** displays the overlap of Compton profiles in the incident ion frame of reference, so that the origin of electron momentum distribution for electrons in Ar is shifted from that of in F by a fixed ion–atom impact velocity. The area of the shaded region, which shows the overlap of fluorine and argon Compton profiles, is proportional to the electron

transfer probability.

It is apparent from the top panel of the figure that the transfer probability can be maximized by decreasing the relative ion–atom collision velocity. In this case, however, the electron transfer to the M (and higher) shells of fluorine will become significant, resulting in multiple Auger transitions, which will obstruct the identification of L shell triply excited states.

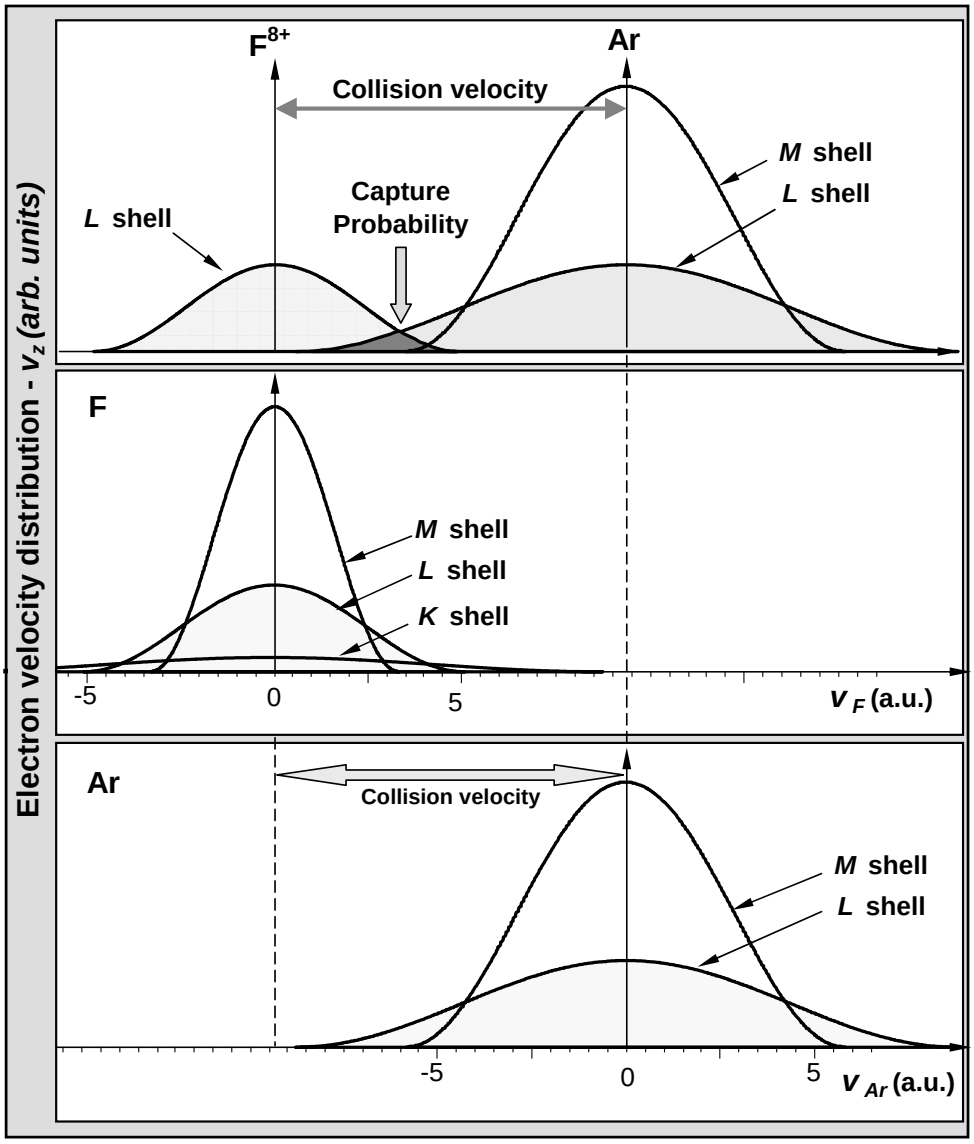


Figure 39: Visualization of the electron transfer probability. Electron momentum distributions (Compton profiles) are shown for the projectile ion (middle panel) and the target atom (bottom panel). The top panel shows the electron transfer probability, which is proportional to the overlap of electron Compton profiles of the target atom and the projectile ion.

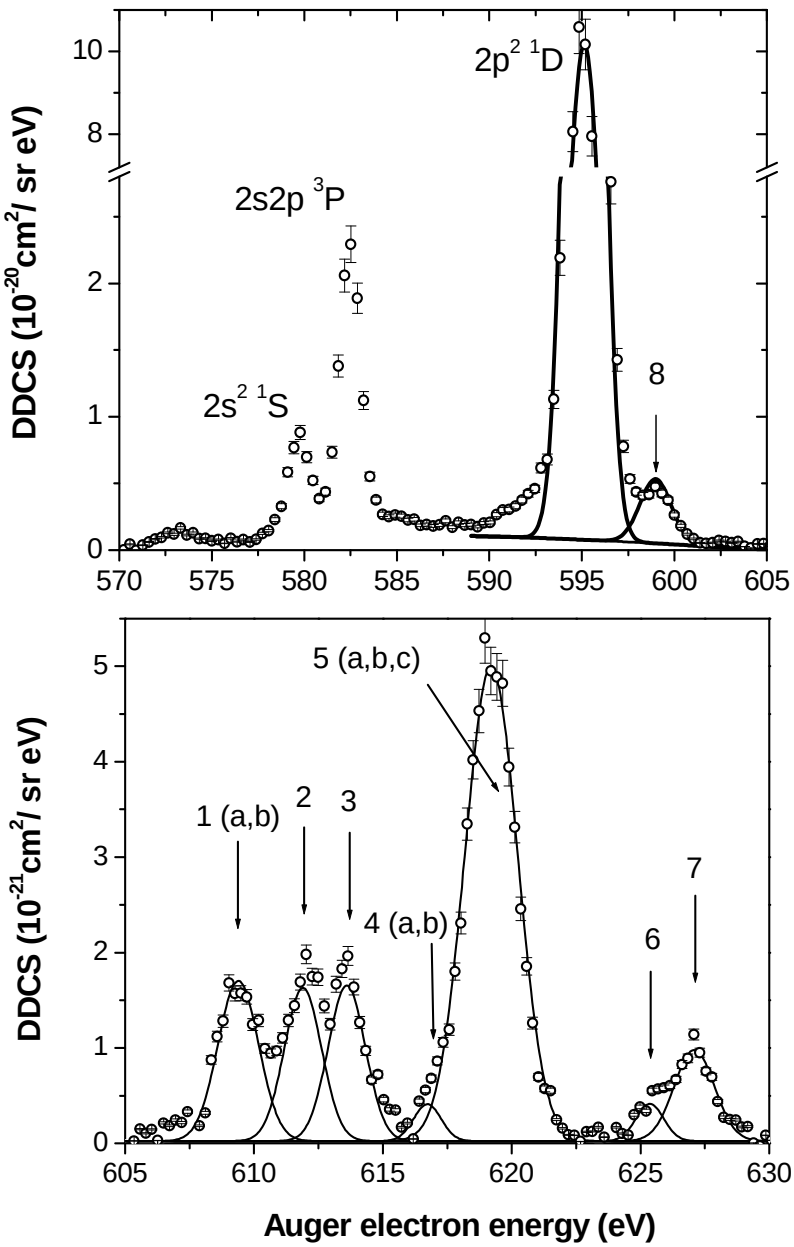


Figure 40: Present experimental measurements of Auger decay channels from the triply excited states of Li-like fluorine into the continua of $F^{7+}$ ions formed in 16 MeV $F^{9+}$ on Ar collisions. Peak labels are given in Table 8. The solid line represents the Gaussian fit to the experimental data.

It is also seen from the figure that for the present optimized collision system (i.e., 16 MeV $F^{9+}$ on Ar), the production of $n = 2$ triply excited states of fluorine is realized primarily by the transfer of $L$ shell electrons of Ar.

Since triply excited states are identified from the energies of the corresponding Auger transitions, formation of other states, which have Auger energies close to the investigated ones, should be avoided. For bare fluorine ions, the major possible contamination will come from the decay of the $2l2l'3l''$ states. In the present collision system, however, these states are hardly populated since electron capture from the $L$ shell of Ar to the n=3 shell of fluorine is very small, due to the difference in binding energies for these shells.

Figure **??** shows the measured Auger electron spectra resulting from the collisions of 16 MeV $F^{9+}$ ions on Ar. Auger electrons in the projectile rest frame energy range of 600–625 eV emitted from the $2s2p^2\,{}^2S$, ${}^2P$, ${}^2D$, ${}^4P$ and $2p^3\,{}^2P$, ${}^2D$ triply excited states were observed. The upper frame also shows Auger transitions from 2l2l′ doubly excited states, formed by double electron capture. Auger energies of these well known transitions were used for the precise energy calibration of the electron spectrometer. Peak assignments and Auger transition energies are presented in Table 8. For the 2l2l′2l″ triply excited states, we can still use the conventional independent particle designations. Each state decays by Auger emission to 1s2l singly excited states of $F^{7+}$. These measured energies are compared to theoretical predictions where the energies of the triply excited states are calculated using the

HSCC method.

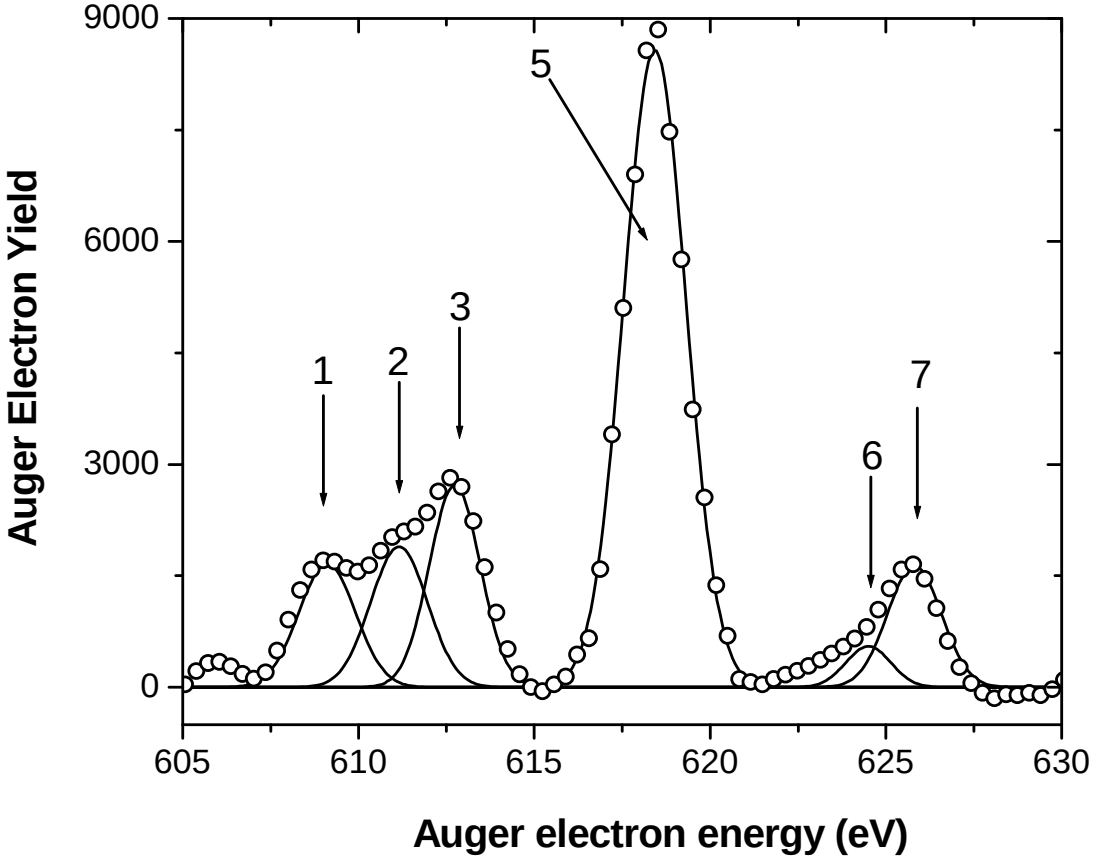


Figure 41: Present experimental measurements of Auger decay channels from the triply excited states formed in collisions of $F^{9+}$ ions on Kr. The solid line represents the Gaussian fit to the experimental data.

Clearly, there is a good agreement between the calculated Auger energies and the experimental results. All of the theoretical energies are within the experimental uncertainty of 0.25 %.

We note that the energies of $2l2l'2l''$ triply excited states of $F^{6+}$ also have been calculated using the 1/Z expansion [?] and truncated diagonalization [?] methods,

but these calculations show inferior agreement with the measurements.

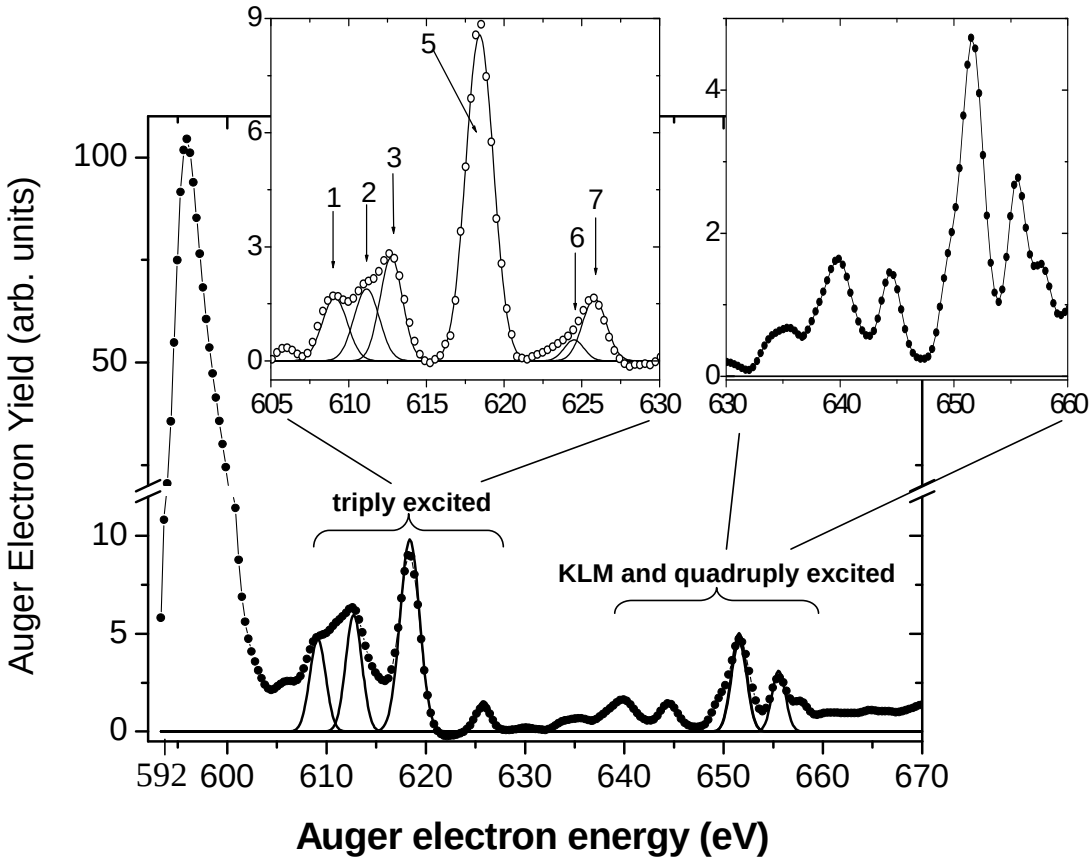


Figure 42: Present experimental measurements of Auger decay channels from the KLM and quadruply excited states formed in collisions of $F^{9+}$ ions on Kr. The solid line represents the Gaussian fit to the experimental data.

Triply excited states of fluorine were also produced in collisions of 16 MeV $F^{9+}$ ions with Kr gas (See Fig. **??**). The M shell of atomic Kr has a binding energy of $-5.62\,a.u.$, which ensures a significant electron transfer probability to the $n = 2$ level of $F^{8+}$. Moreover, since Kr electrons are transferred from the M shell, the number of

active electrons is 18, and the transfer rate is expected to be higher compared to the L shell of Ar. On the other hand, the larger cross section for the process may result in an appreciable amount of double collisions in the gas cell. In this case, absolute cross section measurements of triple electron capture from Kr targets will be less accurate than from Ar. Therefore, only experimental data obtained in collisions with Ar have been used to test the prediction of model calculations, presented later in this chapter.

Since $F^{9+}$ on Kr collisions result in the enhanced experimental statistics for the production of hollow states, these targets represent the best collision partner to probe the existence of $n = 2$ intrashell quadruply excited states, formed in quadruple electron capture. Figure **??** shows the Auger electron spectra for electron energies that correspond to the Auger decay from $n = 2$ intrashell quadruply excited states to $1s2l2l'$ doubly excited states of $F^{6+}$ ion. A number of well pronounced peaks at the high energy wing of the spectrum represent transitions from Auger KLM lines into the ground state of $F^{7+}$ ion and Auger transitions from $2l2l'2l''$ triply excited states are seen at the low energy side. Although no significant contribution from other states has been observed. The absence of Auger peaks corresponding to transitions from the $2l2l'2l''2l'''$ quadruply excited states indicates that both finer energy resolution and higher experimental statistics are needed for their observation.

## 8.3 Hyperspherical Close Coupling Calculations

One of the main goals for studying triply excited states is to find new approximate quantum numbers such that they can be ordered into new classification scheme.In the past decade, the investigation of triply excited states using hyperspherical coordinates resulted in the successful classification of both the $2l2l'2l''$ and $3l3l'3l''$ manifolds By analyzing the correlated motion of the three electrons, intrashell triply excited states of atoms have been classified akin to the different bending vibrational normal modes of an $XY_3$ molecule, with X being the nucleus and Y an electron. The classification, which was based on a model of three electrons on the surface of a sphere, has not yet been tested fully largely, due to the lack of information on the energies of triply excited states, either from accurate calculations or from experiments. As a result, the HSCC method for three-electron systems has been developed in order to obtain a larger set of accurate theoretical data for analysis. In the HSCC method, which has been extensively employed for the two-electron systems [**?**], the total wavefunction is expanded in analogy to the Born-Oppenheimer approximation but with the hyperradius as the adiabatic parameter. Figure **??** shows an example of the hyperspherical potential curves for the $^2P^o$ states of $F^{6+}$ in the region where $2l2l'nl''$ triply excited states are located. In the HSCC method the couplings among the potential curves are included and the solution of the coupled hyperradial equations allows one to obtain accurate energies and widths of the resonances. In

particular, the coupling with the family of curves with sharp descent is responsible for the Auger transitions to the singly excited states of $F^{7+}$. Specifically, the R-matrix propagation method has been used together with the slow variable discretization (SVD) procedure [**?**] to solve the coupled equations. Energy derivatives of the sum of the eigen-phases were obtained directly from the R-matrix at the fixed end point of the hyperradius $R \sim 10$ a.u., and fitted to a Lorentzian function to evaluate energies and widths. This technique allows to evaluate approximate energy

positions and total widths without applying boundary conditions at $R \to \infty$.

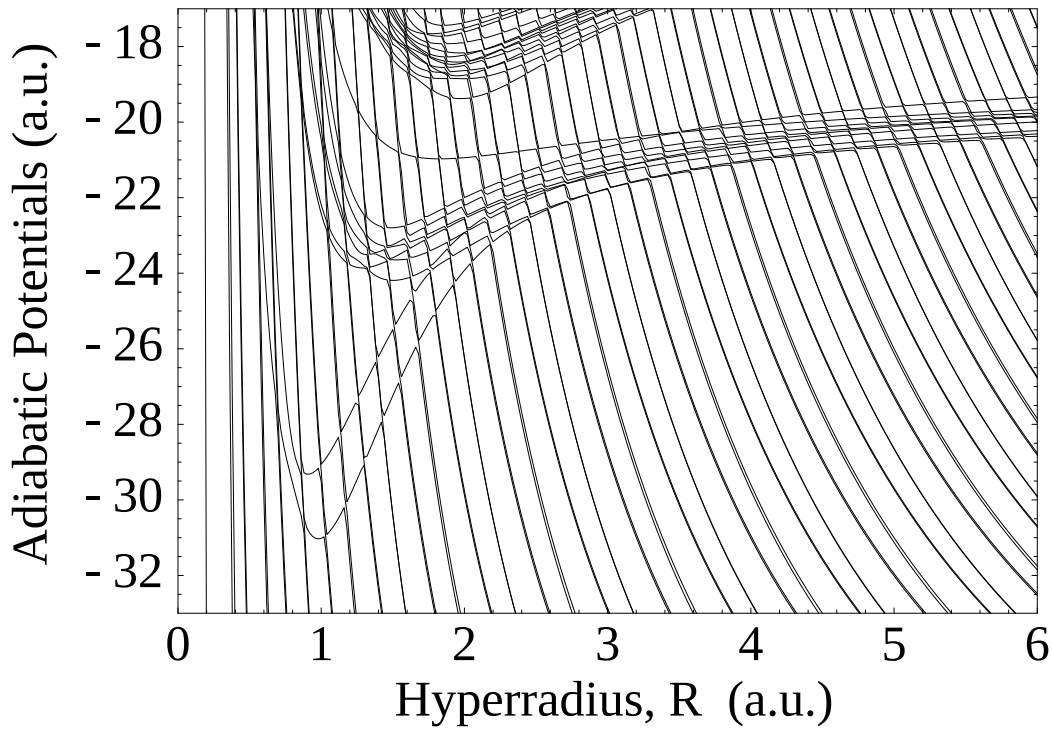


Figure 43: Adiabatic hyperspherical potential curves for $^2P^o$ states of $F^{6+}$ in the energy region of 2l2l′nl″ triply excited states. The two lowest attractive potential wells support the two intrashell states $2s^2 2p$ and $2p^3$ of this symmetry. The family of curves with fast descent represent continuum states of $F^{7+}$ which are coupled to triply excited states resulting in autoionization.

As explained earlier, triple electron capture is an efficient method for populating triply excited states without relying on the weak electron-electron interaction. To demonstrate the validity of this argument, we calculated the triple electron capture

cross sections within the independent electron approximation. In the first step, the probability for transferring an $L$-electron of Ar to the $2s$ or $2p$ states of $F^{8+}$ is calculated using the standard two-center atomic orbital expansion method. Then, the triple electron capture probability is calculated within the independent electron model, which follows a simple binomial distribution, as discussed in the previous chapter. By integrating over the impact parameter plane, the triple electron capture cross section for each triply excited state is then calculated assuming statistical populations of J–sublevels and the isotropic emission of Auger electrons. In Table 8, the theoretical differential cross sections for the zero degree Auger electron emission from the observed states are compared to experimental results. The agreement is quite acceptable in view of the complexity of the process. This confirms that triply excited states are formed mostly without relying on the weak electron-electron correlation. However, electron correlation does play a major role in the calculated energies and the decay widths of triply excited states.

## 8.4 Results and Discussion

Table 8 displays Auger decay branching ratios obtained from present measurements along with a selection of theoretical predictions for triply excited $F^{6+}$ ions [?] and Li atoms [**?**]. The determination of branching ratios in the present experimental technique is independent of the electron spectrometer constant and target pressure. That significantly reduces the experimental uncertainty, providing accurate infor-

mation on the decay dynamics from populated states.

An overall reasonable agreement between theoretical predictions and present experimental results was observed for all investigated Auger decay channels. In the analysis of peak 5, which represents a mixture of three decay channels from $2s2p^2\,{}^2P$, ${}^2D$ and $2p^3\,{}^2D$ triply excited states, we relied on the knowledge of the branching ratios for the $2s2p^2\,{}^2D$ state that was produced by RTE in metastable ion–atom collisions, as explained in chapter 6. Since in this work the $2s2p^2\,{}^2D$ to ${}^1S + {}^3P$ decay channel is measured separately (peak 1), the contribution of the other decay branch from this state (${}^2D$ to ${}^3S$) into peak 5 has been evaluated. In order to extract the individual contributions of the remaining two Auger decay channels in peak 5, namely, $2s2p^2\,{}^2P$ to $1s2p\,{}^3P$ and $2p^3\,{}^2D$ to $1s2p\,{}^3P$, calculations within an independent electron approximation were performed and the results were normalized to the other decay branches (peaks 2, 3) from $2s2p^2\,{}^2P$ and $2p^3\,{}^2D$ states observed in the spectra.

The good agreement between experimental and theoretical branching ratios indicates a correct representation of the investigated triply excited states through a chosen configuration complex, as was stressed in recent work of K.T. Chung [?]. Also, the agreement of the branching ratios calculated for Li atom with the experimentally measured ones for $F^{6+}$ signifies that Auger decay branching ratios are insensitive to the nuclear charge along the isoelectronic sequence.

Table 8: Summary of present experimental results and theoretical calculations for the observed triply excited states of $F^{6+}$. Single differential cross sections (SDCS) are given in units of $10^{-21} cm^2/sr$. Auger energies are calculated relative to the ground state of Li-like fluorine (E = 2242.2 eV [?]).

| Peak | State | | Auger Energy (eV) | | SDCS | SDCS |
|---|---|---|---|---|---|---|
| No | Initial | Final | Exp. | HSCC calc. | exp. | calc. |
| $1a$ | $2s2p^2\,{}^2D$ | $1s2s\,{}^1S$ | 609.4±0.5 | 609.35 | 3.3±0.6 | 6.05 |
| $1b$ | $2s2p^2\,{}^2D$ | $1s2p\,{}^3P$ | | 609.74 | | |
| 2 | $2s2p^2\,{}^2P$ | $1s2p\,{}^1P$ | 611.9±0.6 | 611.73 | 2.9±0.7 | 3.19 |
| 3 | $2p^3\,{}^2D$ | $1s2p\,{}^1P$ | 613.6±0.6 | 613.60 | 2.9±0.8 | 1.02 |
| $4a$ | $2s2p^2\,{}^2S$ | $1s2s\,{}^1S$ | 616.7±0.5 | 617.08 | 0.5±0.2 | 0.99 |
| $4b$ | $2s2p^2\,{}^2S$ | $1s2p\,{}^3P$ | | 617.47 | | |
| $5a$ | $2s2p^2\,{}^2P$ | $1s2p\,{}^3P$ | 619.1±0.8 | 618.11 | 12.7±2.9 | 15.90 |
| $5b$ | $2s2p^2\,{}^2D$ | $1s2s\,{}^3S$ | | 618.39 | | |
| $5c$ | $2p^3\,{}^2D$ | $1s2p\,{}^3P$ | | 619.04 | | |
| 6 | $2s2p^2\,{}^2S$ | $1s2p\,{}^3S$ | 625.4±0.5 | 625.73 | 0.5±0.2 | 1.35 |
| 7 | $2p^3\,{}^2P$ | $1s2p\,{}^3P$ | 627.1±0.5 | 627.12 | 1.8±0.4 | 1.86 |
| 8 | $2s2p^2\,{}^4P$ | $1s2p\,{}^3P$ | 599.0±0.7 | 599.29 | 9.5±1.9 | 13.10 |
| | | | SDCS (sum) | 34.37±7.7 | 43.84 | |

Table 9: Summary of experimental and theoretical branching ratios for main Auger decay channels from triply excited states of $F^{6+}$.

| Auger Peak | Peak Assignment | | Branching Ratios | | |
|---|---|---|---|---|---|
| No | Initial state | Final state | Exp. | Theory [?] | Theory [?] |
| $1a$ | $2s2p^2\,{}^2D$ | $1s2s\,{}^1S$ | 0.41 | 0.44 | 0.52 |
| $1b$ | $2s2p^2\,{}^2D$ | $1s2p\,{}^3P$ | | | |
| 2 | $2s2p^2\,{}^2P$ | $1s2p\,{}^1P$ | 0.45 | 0.39 | 0.44 |
| 3 | $2p^3\,{}^2D$ | $1s2p\,{}^1P$ | 0.32 | 0.25 | 0.24 |
| $4a$ | $2s2p^2\,{}^2S$ | $1s2s\,{}^1S$ | 0.50 | 0.50 | 0.52 |
| $4b$ | $2s2p^2\,{}^2S$ | $1s2p\,{}^3P$ | | | |
| $5a$ | $2s2p^2\,{}^2P$ | $1s2p\,{}^3P$ | 0.55 | 0.60 | 0.56 |
| $5b$ | $2s2p^2\,{}^2D$ | $1s2s\,{}^3S$ | 0.59 | 0.56 | 0.48 |
| $5c$ | $2p^3\,{}^2D$ | $1s2p\,{}^3P$ | 0.68 | 0.74 | 0.75 |
| 6 | $2s2p^2\,{}^2S$ | $1s2p\,{}^3S$ | 0.50 | 0.37 | 0.47 |
| 7 | $2p^3\,{}^2P$ | $1s2p\,{}^3P$ | - | 0.78 | 0.60 |
| 8 | $2s2p^2\,{}^4P$ | $1s2p\,{}^3P$ | 1 | 1 | 1 |

## 8.5 Conclusions

In summary, we demonstrate a novel experimental method where triply excited states of atoms and ions can be efficiently populated via triple electron capture. Unlike photoabsorption or electron impact excitation from the ground state of an atom, which rely on the weak electron-electron correlation to populate triply excited states, the present method benefits from the stronger electron-projectile Coulomb interaction, resulting in the copious production of hollow states in ions and atoms. The technique was demonstrated by investigating autoionizing $2s2p^2\,{}^2S$, ${}^2P$, ${}^2D$, ${}^4P$ and $2p^3\,{}^2P$, ${}^2D$ states of fluorine produced in energetic collisions of 16 MeV $F^{9+}$ ions with Ar atoms. The energies of these triply excited states are compared to new calculations based on the hyperspherical close coupling method. Differential cross sections for triple electron capture are calculated in the independent electron approximation and are shown to be in good overall agreement with the experimental data. In addition, the Auger decay branching ratios have been extracted from the electron spectra and compared to the limited calculations available in the literature. By proper selection of collision partners, we expect that triple electron capture can offer an efficient method for the study of triply excited states in many different ions.

# 9 Conclusions

Multielectron interactions in fast ion–atom collisions were investigated using high–resolution projectile Auger electron spectroscopy. Several different projects have been accomplished by measuring state-resolved projectile Auger cross sections utilizing a novel high–efficiency hemispherical analyzer with a position sensitive electron detector. The measurements were performed at zero degrees with respect to the beam direction, where the kinematic broadening is minimized.

A universal technique for the determination of the metastable $1s2s\,^3S$ ion fraction, based on measurements of the Auger electron emission from doubly excited states of Li-like ions formed in collisions of investigated beams with light targets has been developed. It was subsequently used to measure the fraction of metastable $1s2s\,^3S$ ions in fast He-like B, C, N, O, F beams produced in collisions with thin carbon foils as a function of both the incident energy in the range of 0.5 to 2 MeV/u and the foil thickness in the range of 1-5 $\mu g/cm^2$. Some differences were observed both in the energy dependence and the absolute value of metastable fractions for different ion beams. In particular, the metastable content in $C^{4+}$ ions produced in carbon foils was found to be significantly lower than that of other investigated

beams. The observed deviation has been explained as due to K-vacancy sharing, which is known to have the highest probability for symmetric collisions.

The dominant process contributing to the formation of metastable $1s2s\,^3S$ ions in collisions with atomic targets has been identified. It was demonstrated that the K-shell vacancy production in He-like beams, that leaves ions in the $I^{(Z-1)+}$ charge state, followed by subsequent electron capture into the 2s electron state is the only significant contribution to the formation of the metastable $1s2s\,^3S$ ions in both solid and gas targets. The first theoretical model for the predictions of metastable $1s2s\,^3S$ ion fraction has been developed and successfully applied for predictions of absolute values and energy dependence of the metastable fraction.

The present method for the determination of the metastable fraction relies on theoretical cross sections for both RTE and electron capture processes. A number of independent measurements using a different technique [**?**] have been performed. Although, this technique is only applied when two beams with the same energy can be produced with different metastable fractions, a few measurements were made for systems, studied in this thesis. The new results agree with the ones obtained in the present work, substantiating the accuracy of the method developed in this thesis.

The knowledge of the metastable fraction has been used to study the triply excited $2s2p^2\,^2D$ resonance that was produced by resonant transfer excitation of metastable $B^{3+}$ ions in collisions with $H_2$ targets. Measurements of the Auger electron emission in the direction of the ion beam was used to determine the absolute

cross sections for the formation of the triply excited $2s2p^2\,{}^2D$ state and the branching ratios of the corresponding elastic and inelastic electron scattering channels. The results were compared to existing theoretical calculations for the Auger decay rates. It was demonstrated that the experimentally measured autoionization rate for the elastic decay channel from the $2s2p^2\,{}^2D$ state is significantly lower than the one calculated within the $1/Z$ expansion method, although the experimental branching ratio for this channel was in full agreement with the theory.

The unique capacity of the present experimental setup to analyze projectile Auger electrons in the energy bandwidth of 20% was employed for studying multi-electron capture processes. In particular, doubly excited KLL states were populated by triple electron capture in collisions of fast (v = 4.5–6.6 a.u.) $C^{6+}$ ions with Ar atoms. Measurements of the Auger electron emission in the direction of the ion beam were used to determine the absolute single differential cross sections for the triple electron capture to all autoionizing KLL states. The results were compared with cross sections calculated within the independent particle model. Single electron capture probabilities, employed by the model, were obtained using the two-center semiclassical close-coupling method, based on an atomic orbital expansion. In order to allow comparison of the measured zero-degree differential cross sections with calculated total cross sections, the Auger electron emission from the doubly excited KLL states was assumed isotropic.

The agreement of model calculations with experimental data is quite acceptable

in view of the complexity of the process. This confirms that electron-electron correlation effects do not play a significant role in the formation of doubly excited states by triple electron capture. The observed agreement also signifies that the projectile's energy levels do not fully readjust in the course of the collision due to the insufficient interaction time, and the projectile charge remains essentially unscreened by captured electrons.

The study of triple electron capture described immediately above gave rise to a new experimental technique that relies on a strong projectile-Coulomb interaction to populate triply excited states in Li-like ions. The production of these states is realized in energetic ion-atom collisions by triple electron capture.

The method is demonstrated by studying triply excited $2s2p^2\ {}^2S^e$, ${}^{24}P^e$, ${}^2D^e$, and $2p^3\ {}^2P^o$, ${}^2D^o$ states of fluorine formed in fast collisions of bare $F^{9+}$ ions with Ar atoms both experimentally, using zero-degree Auger projectile electron spectroscopy and theoretically, using the hyperspherical close coupling method (HSCC).

The Auger decay branching ratios have been extracted from the electron spectra and compared to the limited calculations available in the literature. Differential cross sections for triple electron capture are calculated in the independent electron approximation and are shown to be in good overall agreement with the experimental data. Finally, the energies for the observed triply excited states were calculated using the HSCC method and compared to both the present experimental data and other available calculations. Present results demonstrate that triple electron capture can

offer an efficient method for the study of triply excited states in different ions.

In the author's opinion, the results, presented in this thesis, establish a number of possible directions for future investigations. The experimental technique for measurements of triply excited states in Li–like ions has only been used for fluorine, whereas the need for experimental data for other Li–like ions has been emphasized in many recent theoretical publications. Moreover, the presented experimental technique can be used to study the quadruply excited states, highly correlated resonances that have not yet been observed. The present work demonstrates that the investigation of theses states will be possible if the experimental energy resolution is slightly improved.

# References


[1] U. I. Safronova, A. S. Shlyaptseva, and R. Bruch, Physica Scripta **57**, 519 (1998).

[2] N. Stolterfoht, J. Electr. Spectr. and Rel. Phenom. **67**, 309 (1994).

[3] T. J. M. Zouros and D. H. Lee, in *Accelerator-based atomic physics techniques and applications*, edited by S. M. Shafroth and J. C. Austin (American Institute of Physics Conference Series, New York, 1997), pp. 426–79.

[4] J. Ullrich *et al.*, J. Phys. B **30**, 2917 (1997).

[5] E. P. Benis *et al.*, Nucl. Instrum. Methods in Phys. Res. B **146**, 120 (1998).

[6] P. Závodszky *et al.*, Phys. Rev. Lett. to be published (2001).

[7] A. Barany and *et al.*, Nucl. Instrum. Methods in Phys. Res. B **9**, 397 (1985).

[8] H. Niehaus, J. Phys. B **19**, 2925 (1986).

[9] S. Diehl *et al.*, Phys. Rev. Lett. **76**, 3915 (1996).

[10] S. Diehl *et al.*, J. Phys. B **30**, L595 (1997).

[11] S. Diehl *et al.*, Phys. Rev. A **56**, R1071 (1997).

[12] S. Diehl *et al.*, Phys. Rev. Lett. **79**, 1241 (1997).

[13] S. Diehl *et al.*, Phys. Rev. Lett. **84**, 1677 (2000).

[14] D. Cubaynes *et al.*, Phys. Rev. Lett. **77**, 2194 (1996).

[15] R. Morgenstern, A. Niehaus, and U. Thielmann, Phys. Rev. Lett. **37**, 199 (1976).

[16] R. Morgenstern, A. Niehaus, and U. Thielmann, J. Phys. B **10**, 1039 (1977).

[17] R. Morgenstern, A. Niehaus, and G. Zimmermann, J. Phys. B **13**, 4811 (1980).

[18] A. Itoh *et al.*, J. Phys. B **16**, 3965 (1983).

[19] A. Itoh *et al.*, Phys. Rev. A **31**, 684 (1985).

[20] A. Itoh *et al.*, J. Phys. B **18**, 4581 (1985).

[21] M. L. A. Raphaelian, H. G. Berry, and N. B. Mansour, Phys. Rev. A **43**, 4071 (1991).

[22] J. K. Swenson *et al.*, Phys. Rev. Lett. **57**, 3042 (1986).

[23] T. J. M. Zouros, D. Schneider, and N. Stolterfoht, J. Phys. B **21**, L671 (1988).

[24] T. J. M. Zouros *et al.*, Phys. Rev. A **40**, 6246 (1989).

[25] B. D. DePaola, R. Parameswaran, and W. J. Axmann, Phys. Rev. A **41**, 6533 (1990).

[26] T. J. M. Zouros, C. P. Bhalla, D. H. Lee, and P. Richard, Phys. Rev. A **42**, 678 (1990).

[27] D. H. Lee *et al.*, Phys. Rev. A **44**, 1636 (1991).

[28] R. C. Parameswaran, C. P. Bhalla, B. P. Walch, and B. D. DePaola, Phys. Rev. A **43**, 5929 (1991).

[29] T. J. M. Zouros, D. H. Lee, and P. Richard, Phys. Rev. Lett. **62**, 2261 (1989).

[30] B. Sulik *et al.*, Phys. Rev. A **52**, 387 (1995).

[31] H. P. Hülskötter, W. E. Meyerhof, E. Dillard, and N. Guardala, Phys. Rev. Lett. **63**, 1938 (1990).

[32] T. J. M. Zouros, D. H. Lee, P. Richard, and J. M. Sanders, Nucl. Instrum. Methods in Phys. Res. B **56/57**, 107 (1991).

[33] D. H. Lee *et al.*, Phys. Rev. A **46**, 1374 (1992).

[34] T. J. M. Zouros, D. Schneider, A. Itoh, and N. Stolterfoht, Phys. Rev. A **35**, 1963 (1987).

[35] N. Stolterfoht *et al.*, Phys. Rev. Lett. **57**, 74 (1987).

[36] R. Mann, Phys. Rev. A **35**, 4988 (1987).

[37] H. A. Sakaue *et al.*, J. Phys. B **23**, L401 (1990).

[38] H. A. Sakaue *et al.*, J. Phys. B **24**, 3787 (1991).

[39] M. Breinig *et al.*, Phys. Rev. A **25**, 3015 (1982).

[40] H. I. Hidmi, P. Richard, and I. Ben-Itzhak, Nucl. Instrum. Methods in Phys. Res. B **88**, 313 (1994).

[41] T. J. M. Zouros *et al.*, Phys. Rev. A **53**, 2272 (1996).

[42] M. Zamkov *et al.*, Phys. Rev. A **66**, 042714 (2002).

[43] R. Mann, S. Hagmann, and L. Weitzel, Nucl. Instrum. Methods in Phys. Res. B **34**, 403 (1988).

[44] D. H. Lee *et al.*, Phys. Rev. A **41**, 4816 (1990).

[45] N. Stolterfoht, Phys. Rep. **146**, 315 (1987).

[46] E. P. Benis and T. J. M. Zouros, Nucl. Instrum. Methods in Phys. Res. A **440**, 462 (2000).

[47] P. Závodszky *et al.*, J. Phys. B **32**, 4425 (1999).

[48] E. P. Benis, Ph.D. thesis, University of Crete, Heraklion, 2001.

[49] E. Bonderup and P. Hvelplund, Phys. Rev. A **4**, 562 (1971).

[50] P. Sigmund, Phys. Rev. A **14**, 996 (1976).

[51] D. Brandt, Phys. Rev. A **27**, 1314 (1983).

[52] P. Richard, C. Bhalla, S. Hagmann, and P. Zavodsky, Physica Scripta **T80**, 87 (1999).

[53] T. J. M. Zouros, Comments At. & Mol. Phys. **32**, 291 (1996).

[54] F. Biggs, L. B. Mendelsohn, and J. B. Mann, At. Data & Nucl. Data Tables **16**, 201 (1975).

[55] J. S. Lee, J. Chem. Phys. **66**, 4906 (1977).

[56] B. H. Bransden, *Atomic Collision Theory* (W. A. Benjamin, New York, 1970).

[57] C. P. Bhalla and R. Shingal, J. Phys. B **24**, 3187 (1991).

[58] R. Shingal *et al.*, J. Phys. B **23**, L637 (1990).

[59] S. R. Grabbe, Ph.D. dissertation, Kansas State University, 1997 (unpublished).

[60] E. P. Benis, T. J. M. Zouros, H. Aliabadi, and P. Richard, Physica Scripta **T80**, 529 (1999).

[61] J. B. Marrion and F. C. Young, *Nuclear Reaction Analysis* (North-Holland Publishing Co., Amsterdam, 1968).

[62] N. L. S. Martin and A. von Engel, J. Phys. D **10**, 863 (1977).

[63] M. Terasawa *et al.*, Phys. Rev. A **27**, 2868 (1983).

[64] E. H. Pedersen, Phys. Rev. Lett. **42**, 440 (1979).

[65] H. S. W. Massey and H. B. Gilbody, *Electronic and Ionic Impact Phenomena* (Cambridge Univ. Press, Clarendon, Oxford, 1974).

[66] C. P. Bhalla, Phys. Rev. Lett. **64**, 1103 (1990).

[67] M. H. Chen, B. Crasemann, and H. Mark, Phys. Rev. A **27**, 544 (1983).

[68] D. H. Lee *et al.*, Nucl. Instrum. Methods in Phys. Res. B **56/57**, 99 (1991).

[69] A. S. Schlachter *et al.*, Phys. Rev. A **27**, 3372 (1983).

[70] K. Shima, N. Kuno, M. Yamanouchi, and H. Tawara, NIFS-DATA **10**, 28 (1991).

[71] M. Zamkov *et al.*, Phys. Rev. A **64**, 052702 (2001).

[72] W. E. Meyerhof, Phys. Rev. Lett. **31**, 1341 (1973).

[73] R. Bruch, G. Paul, J. Andrä, and L. Lipsky, Phys. Rev. A **12**, 1808 (1975).

[74] M. Rødbro, R. Bruch, and P. Bisgaard, J. Phys. B **12**, 2413 (1979).

[75] M. Agentof, T. Andersen, and K. T. Chung, J. Phys. B **17**, L433 (1984).

[76] S. Mannervik *et al.*, Phys. Rev. A **39**, 3964 (1989).

[77] E. P. Benis *et al.*, Production of triply excited states in Li-like boron XXI ICPEAC, Sendai, Japan (1999).

[78] Y. Azuma *et al.*, Phys. Rev. Lett. **79**, 2419 (1997).

[79] B. Cleff and W. Mehlhorn, J. Phys. B **7**, 593 (1974).

[80] K. Abrahamsson *et al.*, Nucl. Instrum. Methods in Phys. Res. B **79**, 269 (1993).

[81] J. F. J. Vancura, J. J. Perotti and V. O. Kostroun, Phys. Rev. A **49**, 2515 (1994).

[82] R. Ali, C. L. Cocke, M. L. A. Raphaelian, and M. Stöckli, Phys. Rev. A **49**, 3586 (1994).

[83] N. Nakamura *et al.*, J. Phys. B **28**, 4743 (1995).

[84] N. Selberg, C. Biedermann, and H. Cederquist, Phys. Rev. A **56**, 4623 (1997).

[85] J. H. Posthumus and R. Morgenstern, Phys. Rev. Lett. **68**, 1315 (1992).

[86] J. H. Posthumus and R. Morgenstern, J. Phys. B **25**, 4533 (1992).

[87] H. Merabet and *et al.*, Phys. Rev. A **59**, R3158 (1999).

[88] E. D. Emmons, A. A. Hasan, and R. Ali, Phys. Rev. A **60**, 4616 (1999).

[89] S. Martin and *et al.*, Phys. Rev. Lett. **77**, 4306 (1996).

[90] H. Ryufuku, K. Sasaki, and T. Watanabe, Phys. Rev. A **21**, 745 (1980).

[91] H. Zhang and *et al.*, Phys. Rev. A **64**, 012715 (2001).

[92] T. C. Theisen and J. H. McGuire, Phys. Rev. A **20**, 1406 (1979).

[93] J. Kuang and C. D. Lin, J. Phys. B **29**, 1207 (1996).

[94] M. Rødbro, E. H. Pedersen, C. L. Cocke, and J. R. Macdonald, Phys. Rev. A **19**, 1936 (1979).

[95] V. S. Nikolaev, Sov. Phys. JETP **24**, 847 (1967).

[96] B. F. Davis and K. T. Chung, Phys. Rev. A **39**, 3942 (1989).

[97] B. F. Davis and K. T. Chung, Phys. Rev. A **36**, 1948 (1987).

[98] K. Berrington and S. Nakazaki, J. Phys. B **31**, 313 (1998).

[99] L. VoKy and *et al.*, Phys. Rev. A **58**, 3688 (1998).

[100] K. T. Chung and B. C. Gou, Phys. Rev. A **53**, 2189 (1996).

[101] M. J. Conneely and L. Lipsky, Atomic Data and Nuclear Data Tables **82**, 115 (2002).

[102] J. P. Briand and *et al.*, Phys. Rev. Lett. **65**, 159 (1990).

[103] M. Zamkov *et al.*, Phys. Rev. A **65**, 052702 (2002).

[104] J. A. Tanis, in *Recombination of Atomic Ions*, NATO Advanced Study Institute Series B: Physics, edited by W. G. Graham, W. Fritsch, Y. Hahn, and J. Tanis (Plenum Publishing Corp, New York, 1992), Vol. 296, pp. 241–257.

[105] I. Y. Tolstikhina *et al.*, Physica Scripta **54**, 188 (1996).

[106] K. T. Chung, Phys. Rev. A **59**, 2065 (1999).

[107] E. P. Benis, M. Zamkov, T. J. M. Zouros, and P. Richard, Phys. Rev. A **65**, 064701 (2002).